CONDENSÉ EN FRANÇAIS

1 Introduction

Le champ magnétique terrestre est généré par des sources électriques internes (principalement par le noyau externe de la terre et l'aimantation des roches dans la croûte) de l'ionosphère et de la magnétosphère. Nous pouvons approximativement simuler le champ magnétique de la terre par un aimant dipolaire (William Gilbert, 1600) qui est défini par ces angles de déclinaison (par rapport au nord) et d'inclinaison (par rapport à l'horizon). Nous l'appelons le champ géomagnétique qui est un champ potentiel.

L'un des défis dans l'interprétation des données du champ potentiel (magnétique et gravité) est de déterminer la profondeur des sources superposées verticalement. Bo Holm Jacobsen (1987) a appliqué un filtre pour séparer des formations géologiques en fonction de la profondeur. Beaucoup d'auteurs ont utilisé le prolongement du champ potentiel vers le haut et vers le bas pour mettre en évidence différentes caractéristiques des sources peu profondes et profondes (Jacobsen, 1987; Trompat, et al., 2003; Gordon Cooper, 2004; Chen Long-wei, et al., 2007). Jusqu'à présent, il n'y a pas de méthode efficace pour les distinguer.

L'objectif de notre étude est de développer un nouvel outil d'interprétation afin de séparer les sources superposées verticalement, et aussi pour essayer de distinguer les anomalies avec des volumes différents (taille du corps géologique) et des niveaux de magnétisations différents (nature du corps de l'anomalie causal).

Ce mémoire comporte quatre parties :

1. L'introduction présente la problématique, les objectifs de l'étude et une revue des travaux antérieurs.
2. La deuxième partie est le noyau de ce mémoire. Après un résumé de la théorie fondamentale sur la méthode magnétique et l'analyse du spectre, nous avons décrit, étape par étape, la dérivation d'une nouvelle méthode de l'imagerie profonde (Depth imaging). Par une série de tests sur les données synthétiques, nous avons validé cette méthode. Nous avons aussi discuté en détail de l'impact des bruits sur la qualité d'interprétation et de « l'ambiguïté » dans le résultat d'interprétation.

3. Dans la troisième partie du mémoire, nous avons appliqué la méthode de l'imagerie profonde à l'étude de la structure du dépôt de la mine Gallen. En nous basant sur les résultats d'interprétation des 19 profils, nous avons proposé un modèle complexe tridimensionnel pour le dépôt de la mine Gallen et des zones adjacentes.
4. La conclusion permet de faire le point sur les résultats les plus significatifs des travaux réalisés dans le cadre de ce mémoire et des pistes de recherche possibles pour le futur.

2 DÉVELOPPEMENT DE LA MÉTHODE DE L'IMAGERIE PROFONDE SUR LA BASE DE L'ANALYSE DU SPECTRE

Nous partons de plusieurs modèles physiques simples et de leurs expressions analytiques du champ magnétique, puis nous les transformons en domaine de fréquences afin d'étudier la relation entre le spectre de puissance et la profondeur de différents modèles. Trois modèles physiques simples (sphère, plaque épaisse, cylindre, et une superposition de ces modèles) sont impliqués dans la procédure de calcul. De l'anomalie magnétique au spectre de puissance, la variation de la profondeur d'enfouissement affecte visiblement l'amplitude et la largeur d'anomalie qui est caractérisée par une variation de longueur d'onde dans le domaine de fréquence. Nous avons constaté que la plus grande profondeur d'enfouissement correspond à la plus petite valeur de la longueur d'onde de spectre. Peu importe la géométrie du corps magnétique, la plus grande profondeur d'enfouissement correspond toujours à la plus petite longueur d'onde de la bande principale du spectre associé à la valeur maximale de la puissance. Nous nous demandions si nous pouvions quantifier cette fonction par l'attribut de l'anomalie liée à la profondeur d'enfouissement.

2.1 Relation entre le nombre d'ondes et la profondeur d'enfouissement

Pour une source ponctuelle comme une sphère ou une plaque épaisse en 3D, ou une source allongée horizontale comme le cylindre dans la section 2D, ils ont les mêmes propriétés de la transformée de Fourier, selon la transformée de Fourier de l'anomalie magnétique (Zhining Guan, 2005; Richard J. Blakely, 1995; Changli Yao, 2009) dans une dimension (nous considérons seulement un profil le long de l'axe x) :

$$\Delta\tilde{T} = A \cdot H(k_x, h) \cdot M(k_x, l, m, n, l_0, m_0, n_0) \cdot S(k_x, a, b) \cdot D(k_x, \xi, \eta) \tag{1}$$

$$\tilde{Z}_a = \frac{|k_x|}{il_0 k_x + n_0 |k_x|} \Delta\tilde{T} \tag{2}$$

Où :

Facteur de profondeur : $H(k_x, h) = e^{-2\pi(z-h)|k_x|}$

Facteur de magnétisation : $M(k_x, l, m, n, l_0, m_0, n_0) = [ilk_x + n|k_x|][il_0k_x + n_0|k_x|]$

Orientations de magnétisation : $\vec{n}_1 = (l, m, n)$ and $\vec{n}_2 = (l_0, m_0, n_0)$ sont la direction de magnétisation et la direction du champ magnétique terrestre normale sur le profil de mesure, respectivement :

Facteur de scalaire horizontal : $S(k_x, k_y, a, b) = \frac{\sin(2\pi k_x a)}{2\pi k_x a} \frac{\sin(2\pi k_y b)}{2\pi k_y b}$

Facteur de transfert : $D(k_x, \xi, \eta) = e^{ik_x\xi + ik_y\eta}$

La constante A se rapporte à π et à la susceptibilité de l'espace libre. Si nous notons que k_x pour la longueur d'onde le long de la ligne d'observation, k_y est nul, $S(k_x, a, b)$ est 1 pour le cylindre horizontal et la plaque épaisse. En général, l'intervalle entre les stations de mesure le long de la ligne d'observation est n*10 ou plus, de sorte que pour le facteur scalaire horizontal, nous pouvons le remplacer par une valeur approximative ($S(k_x, k_y, a, b) = 1$).

Nous calculons le déterminant de la composante verticale :

$$\left|\tilde{Z}_a\right| = ck_x{}^2 e^{-2\pi h|k_x|} \tag{3}$$

Où h est la profondeur du centre du corps équivalent, c une constante. Au point d'extrémité du spectre de puissance, la première dérivée $\left|\tilde{Z}_a\right|$ doit être zéro :

$$\left.\frac{\partial |Z_a(k_x)|}{\partial k_x}\right|_{k_x = k_{x\max}} = 0 \tag{4}$$

Alors, nous obtenons une relation entre la profondeur d'enfouissement et le nombre d'ondes en suivant :

$$h_{center} = \frac{1}{\pi k_{x\max}} \tag{5}$$

Où k_{xmax} est le nombre d'ondes correspondant à la valeur maximale du spectre, nous ne considérons que le nombre d'ondes positives, h_{centre} est la profondeur du centre du corps équivalent.

Ensuite, nous généralisons l'eq.5 en divisant le modèle de la sphère en un nombre infini de petites sphères. Leur centre de profondeur d'enfouissement et leurs rayons sont h_0, h_1, h_2, … h_i, …, h_n et r_0, r_1, r_2, … r_i, … r_n, respectivement (figures 2.6b et 2.6c). Basées sur le principe de superposition, les anomalies magnétiques de différents corps aux différentes profondeurs peuvent être considérées comme différents signaux de fréquence; et la réponse du nombre infini de petites sphères est :

$$z_a(x) = \sum_{i=0}^{n} z_i(x) \tag{6}$$

Son spectre de transformée de Fourier est également la somme des spectres de la transformée de Fourier de $z_i(x)$:

$$\tilde{Z}_a(k_x) = \sum_{i=0}^{n} \tilde{Z}_i(k_x) \tag{7}$$

Où $\tilde{Z}_i(k_x)$ est le spectre de transformée Fourier de $z_i(x)$.

Selon l'éq.1 et l'éq.7, nous pouvons obtenir une formule liant le centre de la profondeur d'enfouissement et le nombre d'onde maximale pour une petite sphère arbitraire ou un cylindre horizontal arbitraire. Et si nous considérons r_i comme infiniment petit, lorsque $r_i \rightarrow 0$, les petites sphères deviennent des points, nous pouvons donc simplifier l'éq.6 comme suit :

$$h_i = \frac{1}{\pi k_{xi}} \tag{8}$$

Dans la nature, une véritable source d'anomalie comme une sphère n'existe pas. Les anomalies magnétiques sont principalement générées par des corps irréguliers comme le montre la figure 2.6c dans le Chapitre II de ce mémoire. Nous supposons qu'il existe une anomalie magnétique en un point arbitraire dans l'espace, et que c'est un certain nombre de petites sphères qui génère cette anomalie. Vu que le spectre de puissance $Z_i(k_{xi})$ obtenu à partir de la réponse magnétique de chaque sphère a une valeur maximale de puissance, et que sa profondeur d'enfouissement h et le nombre d'ondes maximales k_{xmax} sont liées par l'éq.5, par conséquent, nous pouvons déterminer la profondeur d'enfouissement de chaque sphère par l'analyse de leur spectre de puissance à des positions arbitraires spatiales. Ultimement, nous pouvons déterminer

une distribution de la source des anomalies magnétiques. Nous appelons cette dernière Imagerie de profondeur.

Nous avons généré les anomalies de 14 petites sphères et ensuite utilisé l'eq.8 pour estimer leur profondeur d'enfouissement. Les résultats sont présentés au tableau 2.2 dans le Chapitre II de ce mémoire. L'erreur relative moyenne de l'estimation des sources profondes et peu profondes est de 21 %. Cependant l'erreur relative est de seulement 5 % pour les sources qui se trouvent à une profondeur supérieure à 150 mètres. Il semble que plus la profondeur d'enfouissement de la source augmente, plus l'erreur d'estimation diminue (figure 2.7). La méthode d'imagerie de profondeur sera donc utile pour localiser des corps enfouis profondément.

2.2 Analyse du spectre de puissance pour les modèles complexes

Les amplitudes du spectre de puissance représentent les intensités de susceptibilité ou de magnétisation à des fréquences différentes pour chaque station. Le long d'une ligne d'observation du champ magnétique, nous avons une série de données $f_i(x)$ qui se trouvent dans la i^e fenêtre comme le montre la figure 2.8 dans le Chapitre II. En utilisant la méthode de transformée de Fourier rapide (FFT), nous obtenons un ensemble de données $F_i(k_x)$ qui est considéré comme la distribution des amplitudes correspondant à des fréquences différentes à une station (P). Cette même procédure est répète N fois pour chaque station. Nous avons résumé cette procédure de calcul de façon schématique à la section 2.5 dans le Chapitre II. La série de données $\{F_i(k_x)\}$ est dans le domaine espace-nombre d'ondes. Les méthodes STFT (Short-time Fourier Transform; Jont B. Allen, 1977), WT (Wavelet Transform; Morlet, 1982; Chui, Charles K., 1992) et ST (S Transform; Stockwell R.G., Mansinha L., Lowe R.P., 1996； Stockwell, 1999) peuvent être utilisées pour transformer les données spatiales dans le domaine de fréquence :

$$f(x) \xrightarrow{Transform\ \ tools} F(x,k_x) \tag{9}$$

En intégrant l'eq.8 dans l'eq.9, nous obtenons les données d'imagerie dans le domaine spatial :

$$F(x,k_x) \xrightarrow{h=g(k_x)} F(x,h) \tag{10}$$

Où :

x est la ligne d'observation;

h représente la profondeur d'enfouissement du corps causatif de l'anomalie;

k_x représente la longueur d'onde ;

$f(x)$ représente la réponse du champ magnétique (courbe noire);

$fi(x)$ représente les données interceptées par la i^e fenêtre (segment de la courbe rouge).

Nous considérons que l'amplitude (spectre de puissance) est un attribut pertinent de l'anomalie magnétique pour chaque longueur d'onde (ou chaque profondeur) à une station. Donc, cet attribut inclut des informations de l'intensité de la magnétisation et de la profondeur du corps magnétique.

Nous avons appliqué la nouvelle méthode aux six modèles de sphère. Pour chaque modèle, l'azimut de la ligne d'observation est $\pi/2$. Les sphères sont dans un champ magnétique aimanté verticalement. Elles ont le même niveau de magnétisation et la susceptibilité est de 0.2 SI pour chaque sphère. La force du champ magnétique incité est de 50 000 nT. Différents paramètres géométriques sont présentés par les figures 2.32-2.37 dans le Chapitre II du mémoire.

Modèle 1 : Telles que présentées à la figure 2.32, deux sources d'anomalies sont très bien définies par leur spectre de puissance, et leur position dans l'espace estimé par l'imagerie de profondeur est identique à celle du modèle. La profondeur du centre de la sphère correspond à la profondeur de la partie supérieure du spectre de puissance (partie inférieure de la figure 2.32).

Modèle 2 : Nous ajoutons une sphère plus profonde en dessous d'une des deux sphères du modèle 1 (panneau supérieur de la figure 2.33), à la position x=0. Ces deux sphères empilées verticalement génèrent une zone rubanée du spectre de puissance élevée (partie inférieure de la figure 2.33). Nous ne pouvons pas distinguer les deux corps facilement, mais nous pouvons deviner qu'il y a deux sources parce que la largeur du spectre de puissance change avec la profondeur et parce que la zone de puissance élevée ne se ferme pas à la profondeur. L'estimation de la position latérale de source peu profonde à l'emplacement de x=250 m correspond exactement à la position du modèle; c'est aussi le cas pour la position latérale des deux modèles à

x=0 m. Pour la précision sur la profondeur des sphères, celle qui est enfouie à 100 mètres de profondeur est marquée par le début de l'amincissement de spectre.

Modèles 3 et 4 : Ces modèles sont composés d'un cylindre horizontal au-dessus d'une plaque épaisse (modèle 3), ou sous la plaque épaisse (modèle 4); ils s'étendent à l'infini le long de l'axe *y*. L'inclinaison du champ magnétique est de 300 et l'azimut du profil d'observation est zéro. Les positions du modèle et leurs paramètres géométriques sont présentés à la figure 2.34 dans le Chapitre II. Pour le modèle 3, les emplacements du centre du cylindre sont (0, 0, -50) et (0, 0, -150) respectivement, l'emplacement du centre de la plaque épaisse est (0, 0, -100) pour les deux modèles.

Selon la forme du spectre habituel des sphères (centré et fermé), le spectre de puissance du modèle 3 implique qu'il existe une autre source profonde qui a une géométrie différente de sphère ou de cylindre. Nous pouvons voir que le haut du spectre de puissance (figure 2.34) définit très bien la profondeur de la sphère. En plus, il y a une discontinuité de spectre qui correspond à la profondeur du centre de la plaque épaisse, ce qui est cohérent avec les modèles 1 et 2. Nous avons distingué ces deux corps superposés verticalement avec succès puisque la plaque épaisse a un grand volume par rapport à la sphère. Si cette plaque épaisse se positionne au-dessus d'un cylindre ou d'une sphère qui est caché plus profond (figure 2.35), elle pourrait engendrer une fausse interprétation et laisser croire que la zone d'anomalie du spectre de puissance représente un seul corps allongé verticalement (figure 2.35). Toutefois, la zone d'anomalie du spectre est estimée entre 100 et 200 mètres de profondeur. Celle-ci récupère les deux corps et représente toujours une interprétation raisonnable.

Modèle 5 : Comme nous ne sommes pas en mesure de distinguer le cylindre profond à partir du prisme dans le modèle 4, nous mettons le cylindre en lieu profond (200 mètres), et nous augmentons son rayon à 50 mètres afin d'obtenir sa réponse (figure 2.36a). L'inclinaison du champ magnétique est de 30 degrés.

À la figure 2.36b-c, nous pouvons clairement distinguer deux zones irrégulières du spectre de puissance. C'est définitivement prouvé que la méthode d'imagerie de profondeur peut séparer les sources superposées verticales si elles sont à part à une certaine distance.

Mais la position du centre de la source dévie de l'emplacement (x=0); nous nous demandons si elle peut être causée par l'inclinaison magnétique. Ainsi, nous avons modifié l'inclinaison à 90 degrés (aimantation verticale) comme dans le modèle 6 suivant.

Modèle 6 : Pour le modèle 6, tous les paramètres géométriques et physiques sont les mêmes que pour le modèle 5, à l'exception de l'inclinaison du champ magnétique est de 90 degrés.

Nous avons toujours les mêmes conclusions avec le modèle 5. Le modèle 6 a montré que la déviation de position n'est pas provoquée par l'inclinaison.

2.3 Analyse du bruit

Nous avons analysé l'impact du bruit sur la méthode d'imagerie de profondeur en utilisant le bruit aléatoire et le bruit blanc Gaussien. Le bruit peut provoquer une déformation grossière au résultat de la transformée de Fourier. Comme le NSR augmente, les composants de DC deviennent ainsi plus évidents.

Une discontinuité se produit lors de l'utilisation de la transformation de Fourier, il s'appelle le phénomène de Gibbs (effet du bord). Souvent, nous devons choisir une fenêtre pour lisser les points discontinus. Afin d'obtenir des fonctions appropriées de la fenêtre, nous avons étudié une série de fonctions et leur impact sur le signal, y compris la fenêtre gaussienne, la fenêtre de Blackman, la fenêtre Hamming, la fenêtre de Hanning et la fenêtre de Bartlett. Pour un même nombre d'échantillonnages, le spectre de signal lissé par la fenêtre gaussienne, la fenêtre de Hamming et la fenêtre de Bartlett est meilleur que par la fenêtre de Hanning et de Blackman. Pour une même fenêtre, un grand nombre d'échantillonnages correspond à un spectre plus lisse ; cependant le nombre d'échantillonnage n'est pas assez grand pour affecter la vitesse de calcul.

2.4 Problème de source équivalente

Afin d'analyser le problème d'équivalence de la source (plusieurs sources peuvent produire une anomalie similaire), nous avons fait une série de modélisations utilisant des modèles de prismes, de sphères, de corps polygonaux 2D.

Le principe d'équivalence de sources a été utilisé pour des transformations du champ potentiel, par exemple, pour les dérivations directionnelles, continuation vers le haut ou vers le

bas. Nous avons discuté de ce problème en citant deux types de sources d'équivalence : source des points confinés à une surface et des corps ayant une géométrie différente ou se situant à différente profondeur. Selon les résultats de modélisations, nous concluons que : 1) le premier type d'équivalence de source ne contient aucune information de la géologie; 2) plusieurs corps ayant une géométrie différente peuvent générer une anomalie magnétique vraisemblable, mais ils doivent se situer à la même profondeur. Cette équivalence ne pose pas de problème dans l'interprétation des données magnétiques ou gravimétriques, car la résolution spatiale de l'interprétation consiste à la localisation réelle de sources. En tentant de simuler certains corps équivalents qui sont plus profonds que le corps causal, nous avons démontré que ce type de source équivalente n'existe pas en réalité.

3 ÉTUDE DE CAS

Nous avons appliqué la méthode d'imagerie de profondeur aux données réelles recueillies à la mine Gallen, dans la ceinture de roches vertes de l'Abitibi, au Québec.

3.1 Contexte géologique

Le dépôt de la mine Gallen des sulfures massifs volcanogènes et des roches volcaniques forme une inclusion dans la granodiorite du lac Dufault (figures 3.1 et 3.2). Les contacts de la granodiorite du Lac Dufault avec les roches encaissantes sont partiellement connus. Le contact nord s'incline vers le sud et il recoupe gisement Gallen. La lentille principale de la minéralisation recouvre une séquence volcanique falisque nommée Formation rhyolitique Sud du lac Dufault, dont la composition varie de tacite à andésite.

Du stockwerk à pyrite est présent dans les roches du plancher du dépôt; ici, l'altération est caractérisée par la séricitisation et la silicification. La déformation progressive est plus intense dans cette zone, celle-ci est marquée par une schistosité pénétration parallèle au contact inférieur de la lentille minéralisée. Les sulfures massifs sont hébergés dans ce qu'on appelle un « horizon de tuf contenant des phénocristaux de quartz » (Riopel, 2001).

La lentille principale de la mine Gallen a environ 250 mètres de longueur et 80 mètres de largeur, avec une petite lentille profonde située au sud-ouest à plus de 200 mètres de profondeur (figure 3.2). La lentille principale se compose principalement de pyrite, mais contient jusqu'à 20 % de sphalérite (Guimont et Riopel, 1998). Les deux lentilles sont associées à une vaste minéralisation disséminée dans la Formation rhyolitique sud du lac Dufault.

3.2 Description des données magnétiques

Les données magnétiques utilisées dans cette étude proviennent principalement d'un levé aéroporté de MEGATEM en 2003 (Fugro airborne surveys). Le Scintrex CS-2 monté sur un avion Tash-12 mesure l'intensité totale du champ magnétique de la terre à une altitude de 70 mètres au-dessus du sol. Les données magnétiques sont ensuite traitées à l'aide du logiciel Geosoft. Un champ linéaire est également supprimé en utilisant Geosoft pour éliminer l'effet régional; les anomalies résiduelles sont réduites au pôle.

La réponse magnétique du dépôt de la mine Gallen sur la carte des anomalies résiduelles est relativement petite, environ de 300 à 700 nT. Mais au sud du dépôt de la mine Gallen, les valeurs de la réponse magnétique sont élevées ce qui attiennent un maximum de 2800 nT dans le sud-ouest de la zone d'étude (figure 3.4 dans le Chapitre III).

3.3 Résultats et interprétations

À la figure 3.1, nous pouvons observer que le dépôt de la mine Gallen est dans un contexte géologique complexe. Nous avons appliqué la méthode d'imagerie de profondeur pour recouvrir une distribution de la susceptibilité magnétique en profondeur à l'intérieur d'une petite zone autour du dépôt de la mine Gallen. Un modèle géologique 3D a été construit par l'interprétation des données de trous de forage pour cette zone (figure 3.5). Nous voyons à la figure 3.2 que les intrusions felsiques porphyriques ont perturbé la séquence de rhyolite, ce qui implique que la géologie réelle du dépôt de la mine Gallen serait beaucoup plus complexe que le modèle géologique 3D montré.

Nous avons procédé au calcul d'imagerie de profondeur le long de dix profils orientés O-E et de neuf profils orientés S-N (la localisation de ces lignes est indiquée à la figure 3.4). En comparant les résultats d'imagerie de profondeur avec la géologie connue de la surface (figure 3.7), il semble que l'amplitude du spectre de puissance de la Formation rhyolitique est inférieure à celui des intrusions felsiques porphyriques (à la gauche de la figure 3.7). Selon l'image du spectre de puissance, les intrusions felsiques porphyriques s'étendent vers l'est.

Le contact nord entre la rhyolite et la granodiorite est clairement démontré par la discontinuité du spectre de puissance (figures 3.7 et 3.8). Il est possible que le contact nord soit incliné vers le sud au niveau peu profond, mais on ne peut pas ignorer l'existence d'une source profonde qui se situe dans le sud-ouest de la zone d'étude. Cette source s'étendait vers le nord-est en profondeur (figure 3.7). Son spectre de puissance a une amplitude élevée de 80000 à 100000 nT. Il pourrait être la source des intrusions felsiques porphyriques. La figure 3.7 nous montre une fois de plus la discontinuité du spectre de puissance dans le nord (à gauche) et la direction du pendage de contact nord vers le SW à faible profondeur (à droite).

Nos résultats d'interprétation par la méthode d'imagerie de profondeur ont montré que la structure souterraine dans la zone de la mine Gallen est très hétérogène, ce qui est conforme à la

carte géologique détaillée (figure 3.2). Notre étude a proposé une nouvelle approche pour l'interprétation des données magnétiques.

4 CONCLUSIONS

Nous avons étudié les caractéristiques du spectre de puissance du champ magnétique dans le domaine de fréquence, ce qui nous a permis de constater qu'il y a une corrélation entre la puissance de spectre et la profondeur d'enfouissement de la source de l'anomalie. Nous avons développé une nouvelle formule mathématique pour exprimer la relation entre la profondeur d'enfouissement et le nombre d'ondes du spectre de puissance. Nous avons ensuite généralisé cette formule à une situation générale et développé une nouvelle méthode d'imagerie en profondeur pour l'interprétation des données magnétiques.

En utilisant des modèles synthétiques, nous avons testé cette nouvelle méthode. Pour les sources horizontales, nous pouvons estimer leur profondeur et leur localisation latérale à haute précision. Lorsque la profondeur d'enfouissement des sources augmente, nous obtenons une plus grande précision de l'estimation par l'analyse de leur spectre de puissance. Pour les corps superposés verticalement, nous pouvons estimer précisément la profondeur de la source peu profonde. Si un petit corps recouvre un corps plus grand, nous pouvons facilement les séparer par une discontinuité du spectre. Toutefois, lorsque le corps plus grand cache un petit en dessous, nous ne pouvons les distinguer que s'ils sont suffisamment espacés.

Pour les anomalies magnétiques, le bruit peut provoquer une déformation grossière au résultat de la transformée de Fourier comme le NSR augmente; ainsi les composants de DC deviennent plus évidents. L'effet du bruit sur les composants avec un petit nombre d'ondes est plus petit que ceux avec un grand nombre d'ondes pour le même rapport de signal-bruit.

À propos du problème d'équivalence de la source, selon nos études, il est possible que plusieurs corps magnétiques à la même profondeur puissent produire une seule anomalie. Cependant, il n'affecte que la forme du corps causal sans affecter le positionnement précis de la source, ce qui est le plus important facteur dans l'exploration minière. Pour un empilage vertical de plusieurs corps magnétiques, l'effet d'augmentation de la profondeur d'enfouissement sur la forme d'anomalie est non compensable par la variation de la susceptibilité. Par conséquent, il est donc possible de distinguer les corps à différentes profondeurs par notre nouvelle méthode.

L'effet du bord dans la transformation de Fourier (le phénomène de Gibbs) est considéré dans notre calcul. En utilisant des fenêtres pour lisser le signal, les résultats de la transformée de

Fourier sont bien meilleurs que ceux du signal d'origine. Le principe de choisir une fenêtre est qu'un nombre suffisant de points d'échantillonnage, en ajustant les paramètres de la fonction de fenêtre, fait le signal original lisse de zéros.

À travers l'étude de cas de la mine Gallen, nous démontrons également que la méthode d'imagerie de profondeur peut produire un modèle complexe sans aucune contrainte de discrétisation du modèle. Nous allons continuer à travailler vers des situations géologiques plus complexes. L'ajout d'informations connues, comme la contrainte dans la procédure de calcul, permettra d'améliorer la résolution spatiale. Nous continuerons également à trouver le lien intrinsèque entre le spectre de puissance et les propriétés physiques, comme la susceptibilité magnétique.

TABLE OF CONTENTS

LIST OF TABLES

LIST OF FIGURES

LIST OF SYMBOLS AND ABBREVIATIONS

Abbreviation or Symbol	Definition
$A,\ B,\ C,\ D$	Apices of prism
A'	Magnetic azimuth of profile
$a,\ b$	Geometric parameters of body
c	Constant
$f(x)$	Data in spatial domain
$F(x,k_x)$	Data in space-wavenumber domain
$F(x,h)$	Data in 2-dimensional spatial domain
FFT	Fast Fourier transform
GWN	White Gaussian Noise
h	Burial depth of geological body
h_{center}	Depth to the center of body
I	Magnetic inclination
i_s	Effective magnetization inclination
k_x	Wave number of x-axis
k_y	Wave number of y-axis
$k_{x\max}$	Wave number corresponding to the maximum value of Power spectrum
M	Total intensity of magnetization
M_s	Effective magnetization
M_x	X-axis' component of M
M_y	Y-axis' component of M
M_z	Z-axis' component of M
$MAX(abs(S))$	Maximum of the absolute values of signal S,

$\vec{n}_1 = (l, m, n)$	Magnetizing direction
$\vec{n}_2 = (l_0, m_0, n_0)$	Direction of the normal geomagnetic field on the Measurement profile
NSR	Percent ratio of noise to signal
n	Numeral
N_{random}	Random noise distributed uniformly
$N0$	White Gaussian noise with the variance of 1
N_G	White Gaussian noise with specific variances
P	Power spectrum
r_A, r_B, r_C, r_D	Distance between two points
$random(0,1)$	Random sequence distributed in the interval [0, 1]
S, S_1 ,S_2	Signal of magnetic response
x	Survey line or x-axis
Z_a	Vertical magnetic anomaly component in spatial domain
$\tilde{Z}_a$	Vertical magnetic anomaly component in wave number domain
2b	Thickness of prism
2-D, 3-D	Two dimensional, three dimensional
π	Circumference ratio (PI)
μ_0	Magnetic permeability of free space
α	The dip angle of the prism
κ	Magnetic susceptibility of rocks and minerals
r	Radius of sphere or cylinder
φ_A, φ_B, φ_C, φ_D	Angles between r_A, r_B, r_C, r_D and the vertical line
ΔT	The total magnetic anomaly field in spatial domain
$\Delta\tilde{T}$	The total magnetic field anomaly in wave number domain

CHAPTER 1 INTRODUCTION

1.1 Magnetic field

The Earth magnetic field is generated by internal electric currents (mainly by the Earth's outer core, and the magnetization of rocks in the crust) but also from ionosphere and magnetosphere. The Earth magnetic field can be very roughly approximated by a dipole magnet (William Gilbert, 1600), which is defined by its angles relative to the north (declination) and relative to the horizontal (inclination), called geomagnetic field.

In the middle of 17th century, Swedes (1640) used magnetic compasses to prospect for magnetite in Zhalkovsky (2008). Thaln made a simple magnetometer in 1879 and the magnetic method was then formally used for mineral exploration. In 1915, Schmidt invented the knife edge-type magnetometer (balance), the magnetic method started to be used extensively in iron prospecting, also for studying the geological structure. In 1936, Rogachev succeeded in inventing the airborne magnetometer, and improved the measurement range and the efficiency of the instrument. After the Second World War, the airborne magnetic method was widely used in prospecting metallic deposits over extensive area. In the 20th century, in the 50's and early 60's, the proton-precession magnetometer was used for marine prospecting. At the same time, the magnetic method began to be used for the study of tectonic structures and geological mapping.

Since the strength of the magnetic field from rocks (high iron content) is small compared to the strength of the main magnetic field of the Earth, the Spherical harmonic analysis method (Gauss, 1838) was used to simulate Earth's main magnetic field in order to extract structural geology information of the crust. In 1968, the International Association of Geomagnetism and Aeronomy (IAGA) first proposed the 1965.0 Gaussian spherical harmonic analysis models. This model was approved in 1970 by IAGA and called the international geomagnetic reference field model (IGRF). This model, which is regarded as the mathematical model of the main geomagnetic field and its secular variations, consists of a set of Gaussian spherical harmonic coefficients and annual gradient coefficients. Alldredge recreated the rectangular harmonic analysis (RHA) in 1981, and applied RHA to surface data (1981, 1982, and 1983). Nakagawa and Yukutake (1985) and Nakagawa et al. (1985) extended its application to the analysis of satellite data. The RHA used a plan to approximate spherical surface; therefore the area of the model is

limited. In order to overcome this problem, and to use the rectangular coordinate system to replace the spherical coordinate system, Haines (1985) designed the spherical cap harmonic analysis (SCHA) to simulate the IGRF. Since then, the SCHA is used to provide a magnetic reference field of Canada. Because of the secular variation of the geomagnetic field, spherical harmonic coefficients are republished every five years, and the geomagnetic map is redrawn. Recently, the National Geophysical Data Center (NGDC) and the British Geological Survey developed the 2010.0 - 2015.0 World Magnetic Model (WMM). By using those models, after subtracting the main magnetic field and correcting external sources, geophysicists use the residual magnetic field for mineral exploration and for studying underground structures.

Magnetic exploration has many merits: the magnetometer is light and easy to handle, has high work efficiency and low cost. The most important is that the airborne magnetic method can measure extensive areas in a short period of time; and the measurement is not restricted by the terrain relief, providing global magnetic field anomaly information. This method is therefore extensively used in mineral and oil prospecting, hydrogeology, environmental sounding and for monitoring of the movement of tectonic plates.

1.2 Methodological development and research hypotheses

The availability of magnetic data increases with time, mainly due to those collected from airborne surveys. However, we still have limited access to efficient interpretation tools for magnetic data. There is no clear relationship between the magnetic signal (anomaly) and the rock types as well as the depth of the magnetic anomaly's source, due to large variability of geology in nature. Barton (1929), Nabighian (1962), Bhattacharya (1964), Nagy (1966), and Hjelt (1972, 1974) simulated magnetic anomalies with simple geometries such as a sphere, a cylinder and a plate. Talwani and Ewing (1960), and Talwani (1965) proposed the numerical integration method to simulate arbitrarily shaped bodies. These numerical methods may be cumbersome to use, yet the body to be modeled has to be divided into a large number of thin horizontal laminas (Barnett, 1976). Parker (1973), Dorman and Lewis (1974) presented other numerical methods which are well used in potential fields; these methods involve a series expansion in terms of the Fourier transforms of powers being considered (Barnett). Paul (1974) developed a solution for potential fields based on a homogenous polyhedron composed of triangular facets. Plouff (1976) used polygonal prisms to model the potential field. Barnett (1976) developed an analytical method for

modeling the potential field of a homogenous, arbitrary shaped, three-dimensional body. Okabe (1979) first proposed the 3-D vertex point method to compute the response of a potential field; the main idea is to use polyhedral bodies composed of a set of triangles, which yields high accuracy model. Mareschal (1985), Myoung An, et al. (1990) proposed the solution of potential fields in the frequency domain in order to reduce the computation time. Other methods used in simulating complex models in the spatial domain are developed, as finite element methods (Zeng Hua Lin, 1985; Guan, Zhining, 2005; Wenxiao Zhu, Wansheng Tu, Tian you Liu, 1989) and boundary element methods (Sigh B., 2001; Zheshi Xu, Yunju Lou, 1986). Within the finite element method, there are three approaches: the point element method, the linear element method and the panel method. The point element method can be used in modeling the anomalies whose physical properties are inhomogeneous in horizontal and vertical directions. The linear element method requires that the physical properties are change regularly along straight line. The panel method requires that the physical properties change regularly on a surface.

The magnetic inversion methods have also made a significant progress by recovering an underground susceptibility distribution from magnetic observations. In the 70s, the Hilbert transformation inversion method was used in magnetic interpretation for the estimation of 2-dimensional bodies (Moon, Ushah, 1988; Norden E. Huang, Zhaohua Wu. 2008). In the 80s, a three-dimensional derivative computation was developed (Nabighian, 1984). Werner (1955) proposed a deconvolution method, in which model is composed of a vertical or a dipping plate infinitely extending downward. By solving a set of linear equations, we can estimate the horizontal position, the depth to top, magnetic susceptibility and the magnetized direction of the model. Hartman (1971) used this method in aeromagnetic interpretation, and Hansen (1993) extended it to an interpretation of multiple 2-dimensional anomalies. The Compudepth inversion method, which is based on the Fourier transform, the linear phase filtering and frequency shifting, is used to interpret the position and depth of 2-dimensional bodies (O'Brien, 1972). Wang and Hansen (1990) used it in the interpretation of 3-dimensional polyhedrons. Thompson (1982) proposed the Euler deconvolution which can automatically evaluate the position of the source and rapidly make depth estimates from large amounts of magnetic data. The theory is based upon Euler's homogeneity relationship. Reid et *al.* (1990) and Mushayandebvu et *al.* (2000, 2001) developed this method and resolved the stability problem. Ugalde and Morris (2010) used the cluster analysis technique and resolved the problem of strike and dip angle for 2-

and 3-dimensional bodies. The source parameter imaging (SPI^{TM}) has been presented and developed by Thurston and Smith (1997) and by Thurston, Smith and Guillon (2002); this method assumes either a 2-D sloping contact or a 2-D dipping thin-sheet model and is based on the complex analytic signals.

Stochastic methods have been also widely used in the inverse calculation. In the 60s, Backus and Gilbert proposed the Backus-Gilbert inversion method based on finding the smoothest solution. Tarantola A. (1987) developed a set of theories and methods of probability tomography based on optimization theories, such as the Gauss-Newton method (Chen, Kemna, Hubbard, 2008), the non-linear conjugate gradient method (Kelbert, Egbert, Schultz, 2008) and the Monte Carlo method (Bosch, Meza, Jimenez, Honing, 2006), resolving the divergence problem and the stability problem. After the 90s, the simulated annealing (Rothman, 1986), neural network (Zhining Guan, Junsheng Hou, Linping Huang et *al.* 1998; Ziqiang Zhu, Guoxiang Huang, 1994) and the genetic algorithm (Berg, 1990; Smith, Scales, Fischer, 1992; Curtis, Snieder, 1997) were presented with improved stability of the solution and speed of convergence. Peter G. Lelièvre and Oldenburg (2006) studied the magnetic forward modeling and the inversion of self-demagnetization effects, then designed a methodology for inverting magnetic data for subsurface magnetization and proposed a 3D magnetic inversion with a complicated remanence. Now, Cokriging, a stochastic inversion, which is applied to provide quantitative descriptions of natural variables distributed in space or in time and space and minimizes the theoretical estimation error variance by using auto- and cross-correlations of several variables (Pejman Shamsipour, et *al.* 2011 and 2012).

Due to the complexity of the magnetic field caused by one or more geological bodies with inhomogeneous magnetic susceptibilities and of irregular shapes, therefore several assumptions have been made in the above developments, such as a) the shape of the model is regular or simple; b) magnetization is homogeneous within the body and susceptibility is isotropic in the causative body; and c) the remanent magnetization was not considered for most of calculations.

Although simple geological bodies are easy to simulate, complex geological conditions in actual surveys broaden huge the gap between theoretical models and actual geology. Furthermore, by using conventional interpretation tools, different bodies can be easily distinguished from magnetic anomalies if they are horizontally well apart, but hardly

distinguishable if they are superimposed vertically. In our study, we proposed a new method in spectrum domain, which identifies not only horizontally distributed sources, but also those superimposed vertically.

1.3 Objectives

One of the challenges in potential field (magnetic and gravity) data interpretation is to determine the depth of different vertical superimposed sources. Bo Holm Jacobsen (1987) applied a filter for mapping the geology at different depth levels; many authors used the upward and downward continuation of potential fields to enhance the signal of shallow or deep sources (Jacobsen, 1987; Trompat, Boschetti, and Hornby, 2003; Cooper, 2004; Chen Long-wei, Zhang Hui, and Zheng Zhi-qiang, 2007). However, until now there is no effective method to distinguish them.

The objective of our study is to develop a new interpretation tool in order to separate deep and shallow sources and also try to discriminate magnetic anomalies with different volumes (size of geological body) and magnetic susceptibilities (nature of the anomaly causative body).

CHAPTER 2 THE DEVELOPMENT OF DEPTH IMAGING METHOD BASED ON SPECTRUM ANALYSIS

We start from several simple physical models and their magnetic field analytic expressions, and then transform them into frequency domain in order to study the relation between the Power spectrum & the wave-number of spectrum and the depth of various models.

2.1 Magnetic anomaly of a sphere model

On Figure 2.1, M indicates the geomagnetic field vector or induced geomagnetic vector, its units is in nT (nanotesla); M_H represents its horizontal component which can be projected onto the X-axis (M_x) and the Y-axis (M_y) and M_z is its vertical component.

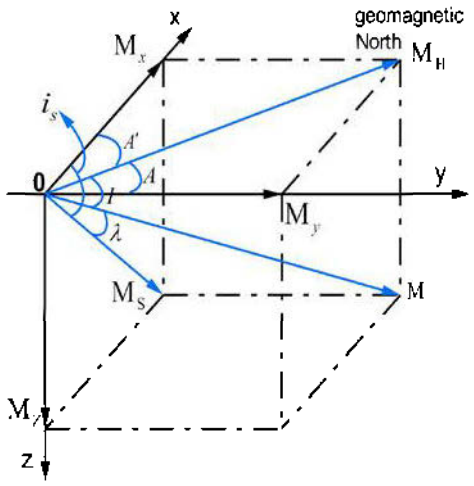

Figure 2.1: Geomagnetic field elements

If there is a ferromagnetic sphere inside of this geomagnetic field, assuming that its remanent magnetization is negligible, it will be strongly magnetized along the geomagnetic field direction, thus, a magnetic anomaly is produced. From a magnetic survey on land, the main parameters measured are total magnetic field anomaly (ΔT), vertical magnetic anomaly (Za) component can be got by calculating from the total magnetic field anomaly or measurement; by an airborne survey we measure the total magnetic field anomaly (ΔT). Their units are in nT.

Outside of the magnetic sphere, the vertical magnetic component Z_a and the total field anomaly ΔT at an arbitrary point in space can be expressed by the following equations (Zhining Gnan, 2005):

$$z_a = \frac{\mu_0 m}{4\pi(x^2+y^2+h^2)^{5/2}}[(2x^2-y^2-h^2)\sin I - 3hx\cos I\cos A' + 3hy\cos I\sin A'] \quad (1)$$

$$\Delta T = \frac{\mu_0 m}{4\pi(x^2+y^2+h^2)^{5/2}}[(2h^2-x^2-y^2)\sin^2 I + (2x^2-y^2-h^2)\cos^2 I\cos^2 A' + (2y^2-x^2-h^2)\cos^2 I\sin^2 A' - 3xh\sin 2I\cos A' + 3xy\cos^2 I\sin 2A' - 3yh\sin 2I\sin A'] \quad (2)$$

$$m = \frac{\kappa}{\mu_0} M \frac{4\pi}{3} r^3$$

Where μ_0 is the magnetic permeability of free space; κ is the magnetic susceptibility of the sphere; m is the magnetic moment of the sphere; r is the radius of the sphere; h is its depth; I is the magnetic inclination; A' is the magnetic azimuth of the profile (observations); (x, y, z) are the coordinates of the survey station, z is zero on the surface and the sphere is located at (0, 0, h).

2.2 Power spectrum analysis of single or multiple spheres

The Fourier transform of a vertical magnetic anomaly is written as following:

$$Z_a(k_x) = \int_{-\infty}^{\infty} z_a(x) e^{-2\pi i x k_x} dx \quad (3)$$

Where $Z_a(k_x)$ is the Fourier transform of $z_a(x)$, k_x and x are the wave-number and distance respectively; and the wave-number has unit of inverse distance.

In order to easily study and compare results, all of Fourier transform results are normalized. The way to normalize Fourier transform results is that: (1) First we find out the maximum of the magnetic response in frequency domain, (2) then we divide the magnetic response in frequency domain by the maximum, (3) the anomalies in frequency domain are normalized in this chapter (only in this chapter, but except the section 2.7 of Chapter II).

We show two spheres on Figure 2.2a. Assuming that they have the same magnetic inclination ($\pi/2$), magnetic azimuth of the profile ($\pi/2$), and the magnetic susceptibility (κ) is 0.2SI, the magnetization (T) is 50000nT. The radius of the sphere 1 is 20m and its center is situated at a depth of 30m. The sphere 2 is buried at a depth of 100m; radius of sphere is 35m.

In Figure 2.2b, from left to right, they are the response of total magnetic anomaly field of the sphere 1 (ΔT) and its vertical magnetic anomaly component (Z_a) along the x-axis crossed the projection of the center of sphere (y=0, x=0), its total magnetic anomaly field and its vertical magnetic anomaly component on the surface of x-y. In Figure 2.2c, they are magnetic response of sphere 2, which are same with that of sphere 1.

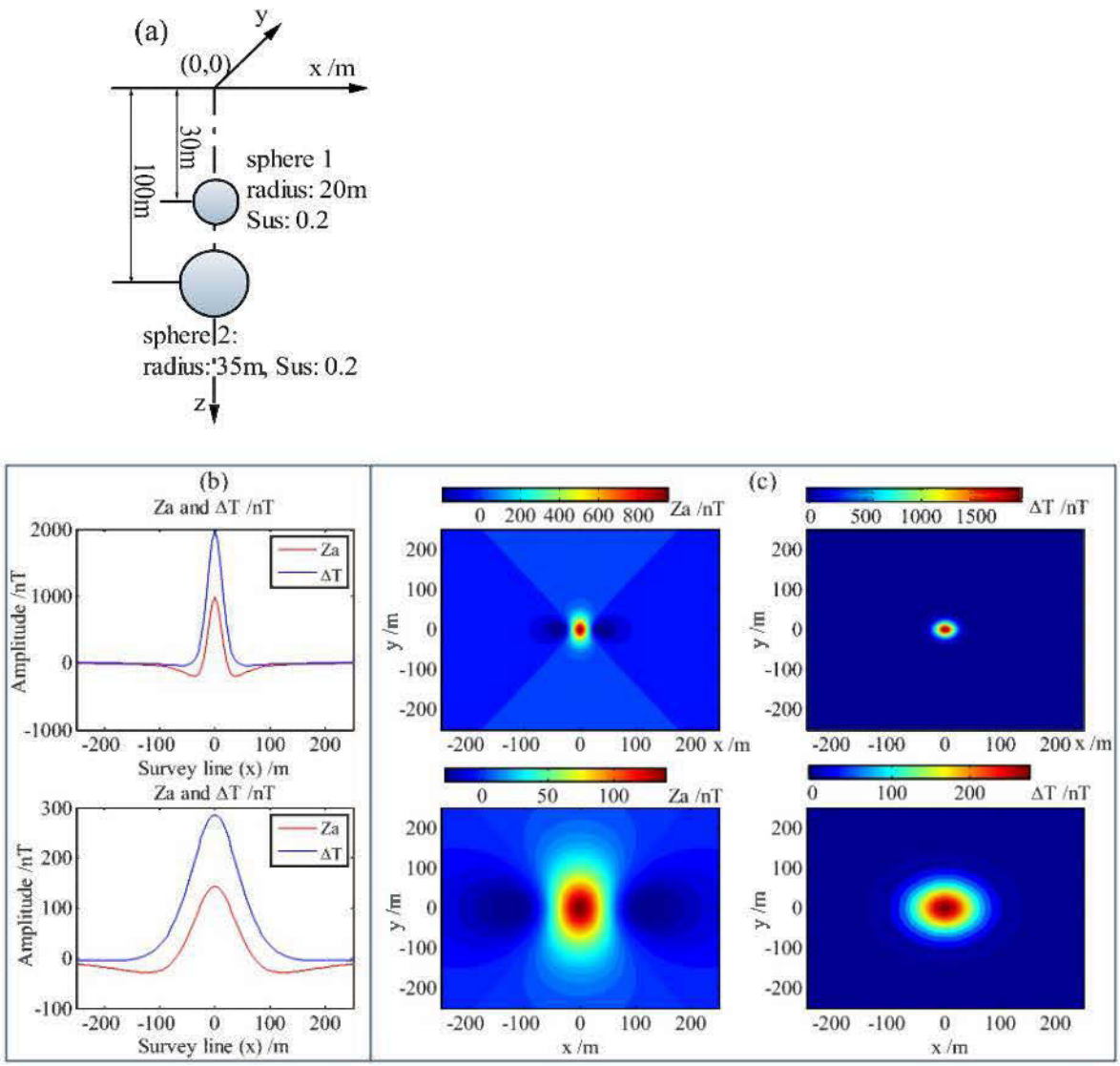

Figure 2.2: a) two sphere models; b) upper panel, magnetic anomalies of the model 1 calculated from eq. 1 and eq. 2 on the upper panel c) and those of the model 2 on the lower panel

From Figure 2.2b and 2.2c, we see that as the depth increases, the magnetic anomaly becomes flatter and weaker.

We designed then three sets of models (Table 2.1). The Set 1 consists of two spheres at same location but having different size. The Set 2 is composed of two spheres of same size, but they have different depths. The Set 3 has two spheres of different size, and the small sphere is over the big one. We calculated the magnetic anomaly of three sets of models, and then we did the Fourier transform of the vertical magnetic anomaly. Figure 2.3 (a) to (c) show clearly that the magnetic anomaly changes only the amplitude in the space (left figure), however the different depths correspond to different wavenumber in the frequency domain. As the depth of the sphere increases, the wave number becomes smaller. We wonder if we could quantify this feature by the anomaly's attribute related to the depth. Please note that the results of Power spectrum are normalized by their own maxima.

Table 2.1: Parameters of three sets of sphere models

Models / parameters	**Set 1 (figure 2.3a)**		**Set 2 (figure 2.3b)**		**Set 3 (figure 2.3c)**	
	Model 1	**Model 2**	**Model 1**	**Model 2**	**Model 1**	**Model 2**
Radius (r)	5m	25m	20m	20m	20m	35m
Center depth (h)	30m	30m	30m	100m	30m	100m
Magnetization (M)	50000nT					
Susceptibility (κ)	0.2SI					
Inclination (I)	$\pi/2$					
Azimuth (A')	$\pi/2$					

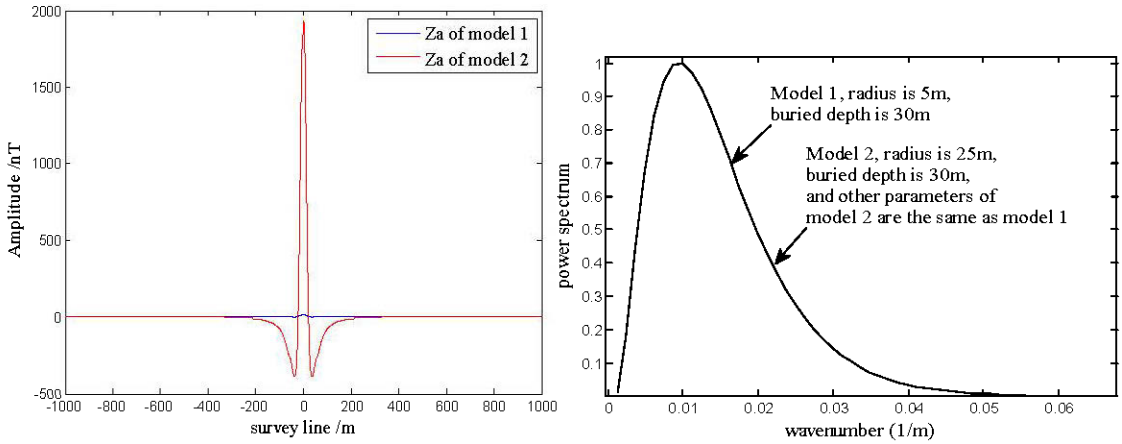

Figure 2.3a: vertical magnetic anomalies (left) and their Power spectrum (right) of the first set of models

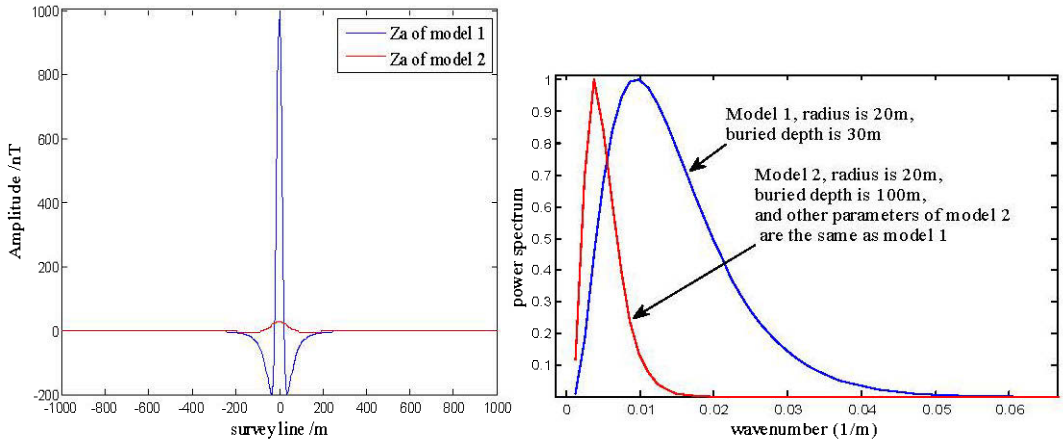

Figure 2.3b vertical magnetic anomalies (left) and their Power spectrum (right) of the second set of models

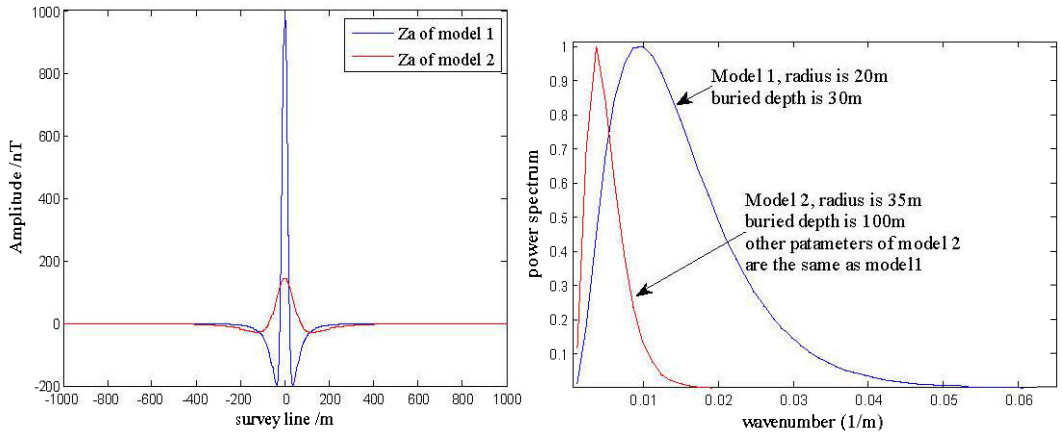

Figure 2.3c: vertical magnetic anomalies (left) and their Power spectrum (right) of the third set of models

Figure 2.3: Vertical magnetic anomalies (left) and their Power spectrum (right) of three sets of models. The results of Power spectrum are normalized by their own maxima

2.3 Magnetic anomaly of a thick prism model

The sphere model represents symmetric 3-D body. Many geological bodies can be simplified as an elongated body such as thick prisms, dykes, veins and lenticular etc. One often regards finite extension (or finite depth) geological bodies as an infinite extension (or infinite depth) models, because when length of the thick prism is ten times larger than its depth, the difference in vertical component between the infinite model ($Z_{a\infty}$) and the finite model (Z_{a2L}) is negligible (Zhining Guan, 2005). Therefore, we consider a thick prism as follows (Figure 2.4): its length in the strike direction (y) is infinite. We assume that P is an arbitrary point in space. The equation for the vertical magnetic component Za is expressed as following (Zhining Guan, 2005):

$$Z_a = \frac{\mu_0 M_S \sin\alpha}{2\pi}\{\sin\gamma \ln\frac{r_B r_C}{r_A r_D} - \cos\gamma[(\varphi_A - \varphi_B) - (\varphi_C - \varphi_D)]\} \tag{4}$$

$$M_S = M\cos\lambda = (M_x^2 + M_z^2)^{1/2} = M(\cos^2 I \cos^2 A' + \sin^2 I)$$

$$\tan i_s = \frac{M_z}{M_x} = \frac{\sin I}{\cos I \cos A'},\ \gamma = \alpha - i_s$$

Where α is the dip angle of the thick prism, and it is not equal to zero; r_A, r_B, r_C, r_D are the distances between A, B, C, D and P, respectively; φ_A, φ_B, φ_C, φ_D are the angles between r_A, r_B, r_C, r_D and the vertical line, respectively; h is the depth of the center of the thick prism; 2b is the thickness, H is the vertical extension of the thick prism; Magnetic azimuth of the profile (A') is the angle between the survey line and the horizontal projection of M_s; i_s is the effective magnetization inclination; Ms is the effective magnetization as shown in Figure 2.1.

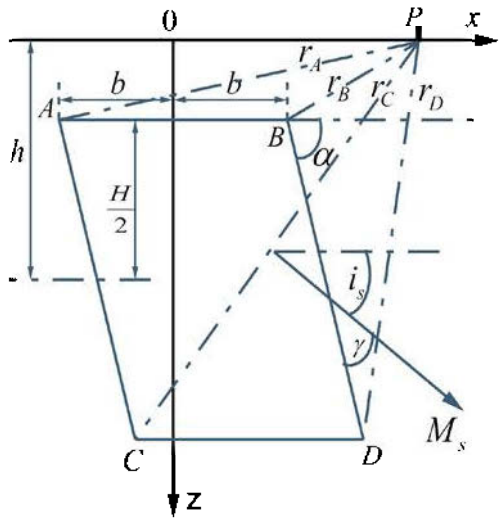

Figure 2.4: Elements of thick prism

The expression of Fourier transform for the thick prism (Zhining Guan, 2005) is given by:

$$\begin{aligned} Z(u) &= \mu_0 b M_s \sin\alpha (e^{-2\pi k h_1} - e^{-2\pi k h_2} e^{-i2\pi k x_2}) e^{i\gamma} \\ &= \mu_0 b M_s \sin\alpha e^{-2\pi k h_1} (1 - e^{-2\pi k H \sin\alpha} e^{-i2\pi k H \cos\alpha}) e^{i\gamma} \end{aligned} \tag{5}$$

Where, k is the wavenumber, h_1 is the depth of the top of the thick prism, h_2 is the depth of the bottom of the thick prism, and x_2 is x-coordinate of the center location of the CD-side of the prism.

In order to evaluate the depth's effect, we modeled this thick prism at two different depths, which are at 50m and 100m respectively, here the effective magnetization inclination is vertically upward, in other words, the Earth's magnetic field direction is vertically upward. As shown in Figure 2.5, we definitively show once again the difference of two anomalies from the vertical magnetic anomaly amplitude (left) and also from the Power spectrum (right). These results confirmed that the bigger the depth is, the smaller the maximal wave-number value is, regardless

of the geometry of the magnetic body. It is the depth of the magnetic body that dominates the distribution of the main wave-number band.

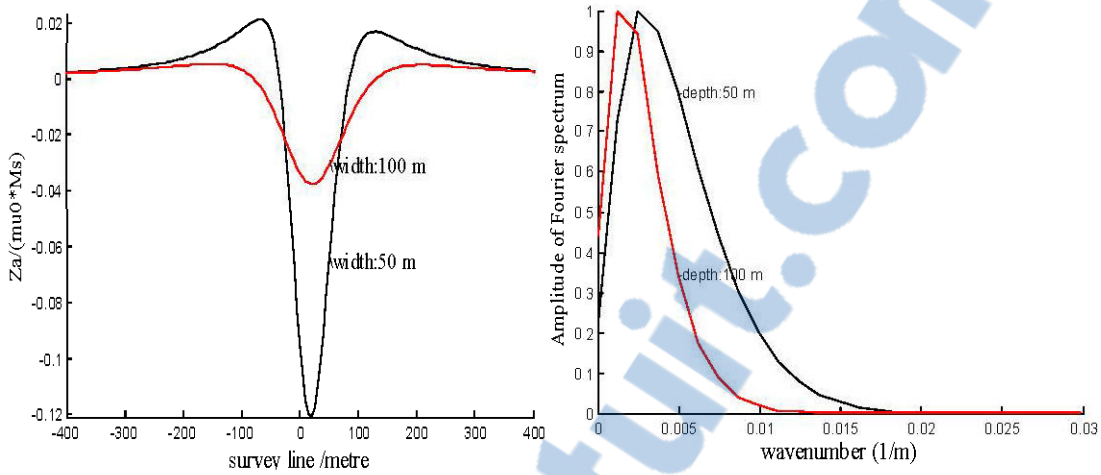

Figure 2.5: Vertical magnetic anomalies (upward) of thick prisms and their Power spectrum at different depths

2.4 The relationship between wave-number and depth

As shown above, the depth of the magnetic anomaly causative body affects significantly the wave-number band, associated to the maximal spectrum value, thus the depth correlates strongly with wave-number.

For a point source or a sphere in 3D, or for a horizontal line source as a cylinder in 2D section, they have the same Fourier Transform properties. According to the Fourier transform of the magnetic anomaly (Zhining Guan, 2005; Blakely, 1995; Changli Yao, 2009), in one dimension (we only consider one profile along the x axis), the mathematic model of the total magnetic anomaly is, that

$$\Delta\tilde{T} = A \cdot H(k_x, h) \cdot M(k_x, l, m, n, l_0, m_0, n_0) \cdot S(k_x, a, b) \cdot D(k_x, \xi, \eta) \tag{6}$$

Once we know the total magnetic anomaly field, we can define the vertical component ($\tilde{Z}_a$) or vice versa.

$$\tilde{Z}_a = \frac{|k_x|}{il_0 k_x + n_0 |k_x|} \Delta\tilde{T} \tag{7}$$

Where:

Depth factor: $H(k_x, h) = e^{-2\pi(z-h)|k_x|}$

Magnetizing factor: $M(k_x, l, m, n, l_0, m_0, n_0) = [ilk_x + n|k_x|][il_0k_x + n_0|k_x|]$

Magnetizing orientation: $\vec{n}_1 = (l, m, n)$ and $\vec{n}_2 = (l_0, m_0, n_0)$ are the magnetizing direction and the direction of the normal geomagnetic field on the measurement profile, respectively.

Horizontal scale factor: $S(k_x, k_y, a, b) = \frac{\sin(2\pi k_x a)}{2\pi k_x a}\frac{\sin(2\pi k_y b)}{2\pi k_y b}$, a and b are approximately geometric parameters of an anomaly.

Shifting factor: $D(k_x, \xi, \eta) = e^{ik_x\xi + ik_y\eta}$, (ξ, η) are the displacement in horizontal direction.

The constant A relates to π and the susceptibility of free space. If we consider wave-number k_x along the survey line (x-axis), k_y is zero, thus, $S(k_x, a, b)$ is 1 for a horizontal cylinder and a thin prism. Also for a specific anomaly parameters a and b are constant. Therefore,

$$\lim_{\substack{k_x\to 0\\ k_y\to 0}} S(k_x, k_y, a, b) = \lim_{\substack{k_x\to 0\\ k_y\to 0}} \frac{\sin(2\pi k_x a)}{2\pi k_x a}\frac{\sin(2\pi k_y b)}{2\pi k_y b} = 1 \tag{8}$$

We only need to calculate the items of domination for the vertical component as following.

$$\left|\tilde{Z}_a\right| = ck_x{}^2 e^{-2\pi h|k_x|} \tag{9}$$

Where h is the center depth of the equivalent body and c is a constant. At the extremum of the Power spectrum, the first derivative of $\left|\tilde{Z}_a\right|$ must be zero, that is,

$$\left.\frac{\partial\left|\tilde{Z}_a(k_x)\right|}{\partial k_x}\right|_{k_x = k_{x\max}} = 0 \tag{10}$$

Then we get a relation between the depth and the wave-number as follows:

$$h_{center} = \frac{1}{\pi k_{x\max}} \tag{11}$$

Where, $k_{x\max}$ is the wavenumber corresponding to the maximum spectrum value, where only the positive wave-numbers are considered, and h_{center} is the center depth of equivalent body.

The equation 11 represents the maximum wavenumber ($k_{x\max}$) corresponding to the maximum spectrum value is used. Indeed, each observed data contains near/shallow and far/deep sources responses, which is a combination of different wavelength anomalies having different wavenumbers. In any case, the vertical magnetic anomaly at a given point should be dominated by sources that locate along the vertical line directly under the point of observation. We generalize eq.11 by dividing a sphere model into an infinite number of small spheres. Their depths and radius are h_0, r_0, h_1, r_1, h_2, r_2, h_i, r_i … h_n and r_n respectively (Figure 2.6b and 2.6c). Based on the principle of superimposition, different magnetic anomalies of different sources can be regarded as different frequency signals; and the response from an infinite number of small spheres is given by, if we neglect demagnetization effects, then

$$\begin{cases} Z_a(x) = \sum_{i=0}^{n} Z_i(x) \\ \tilde{Z}_a(k_x) = \int_{-\infty}^{\infty} Z_a(x) e^{-ixk_x}\,dx = \int_{-\infty}^{\infty} \sum_{i=0}^{n} Z_i(x) e^{-ixk_x}\,dx = \sum_{i=0}^{n} \int_{-\infty}^{\infty} Z_i(x) e^{-ixk_x}\,dx \end{cases} \tag{12}$$

Its Power spectrum is also the sum of the Power spectrums of $z_i(x)$.

$$\tilde{Z}_a(k_x) = \sum_{i=0}^{n} \tilde{Z}_i(k_x) \tag{13}$$

Where, $Z_i(k_x)$ is the Power spectrum of $Z_i(x)$.

According to eq.11 and eq.13, we can obtain a formula related to the center depth and the maximum wave-number for an arbitrary small sphere or a horizontal cylinder, that is

$$h_{icenter} = \frac{1}{\pi k_{xi\max}} \tag{14}$$

Our aim is to obtain a formula about the depth and the wave-number at an arbitrary point. If we consider r_i as infinitely small, that is to say $r_i \to 0$, infinite small spheres become points, and then we can get the formula about the depth and the wave-number at an arbitrary point.

$$h_i = \frac{1}{\pi k_{xi}} \tag{15}$$

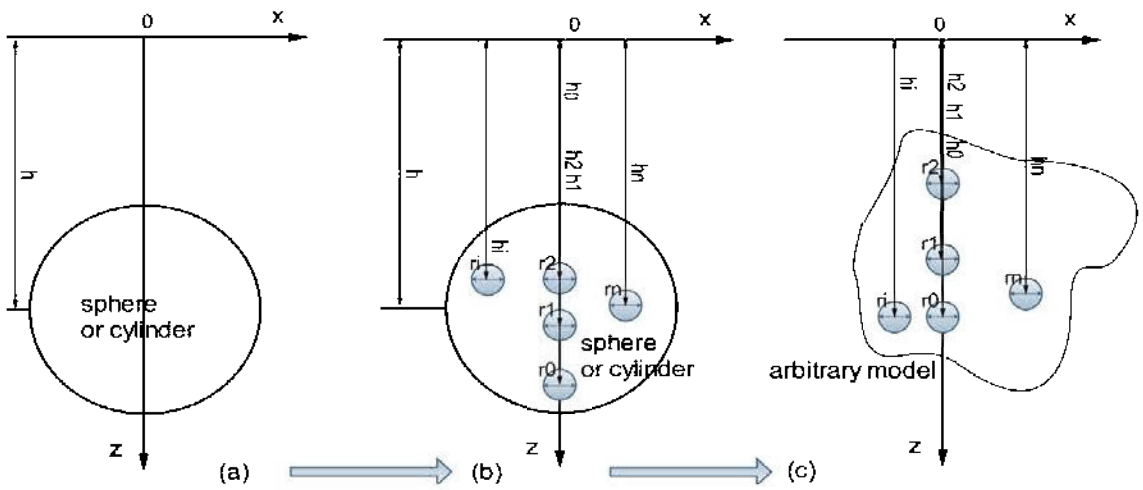

Figure 2.6: Discretization from sphere model to an arbitrary model

In nature, a true sphere anomaly source almost does not exist; magnetic anomalies are mostly generated by arbitrary irregular bodies as shown in Figure 2.6c. Since the Power spectrum $Z_a(k_{xi})$ is obtained from the magnetic response of each sphere has a maximum spectrum value, its depth h and maximum wave-number k_{xmax} are related as defined by eq.15. Therefore, we can determine the depth of a number of spheres through the analysis of their Power spectrum at an arbitrary position; ultimately we can determine a distribution of the source under each observation point and then for whole survey line (please see the next section).

In order to examine the estimated depth of this new method, using eq.15, we simulated 14 small spheres at arbitrary positions. The results are shown in Table 2.2. The average relative error of the estimation for shallow and deep sources is 21%. It seems increasing the depth of source decreases the error (Figure 2.7). The relative error is about 5% if we ouly consider deep sources buried at depth of more than 150 m.

Table 2.2: Estimation of the depth of 14 spheres

Wave-number (1/m)	**True depth (m)**	**Estimated depth (m)**	**Error (m)**	**Error percentage**
9.77E-04	300	326	26	8.67%
1.30e-03	250	244.5	5.5	2.20%
1.56E-03	200	203.7	3.7	1.85%
1.95E-03	150	163	13	8.67%
2.44E-03	100	130.3	30.3	30.30%
2.60E-03	90	122.2	32.2	35.78%
2.93E-03	80	108.6	28.6	35.75%
3.91E-03	70	81.4	11.4	16.28%
4.39E-03	60	72.4	12.4	20.67%
4.88E-03	50	65.2	15.2	30.40%
6.35E-03	40	50.1	10.1	25.25%
8.30E-03	30	38.3	8.3	27.67%
1.27E-02	20	25.1	5.1	25.5%
2.49E-02	10	12.7	2.7	27.00%

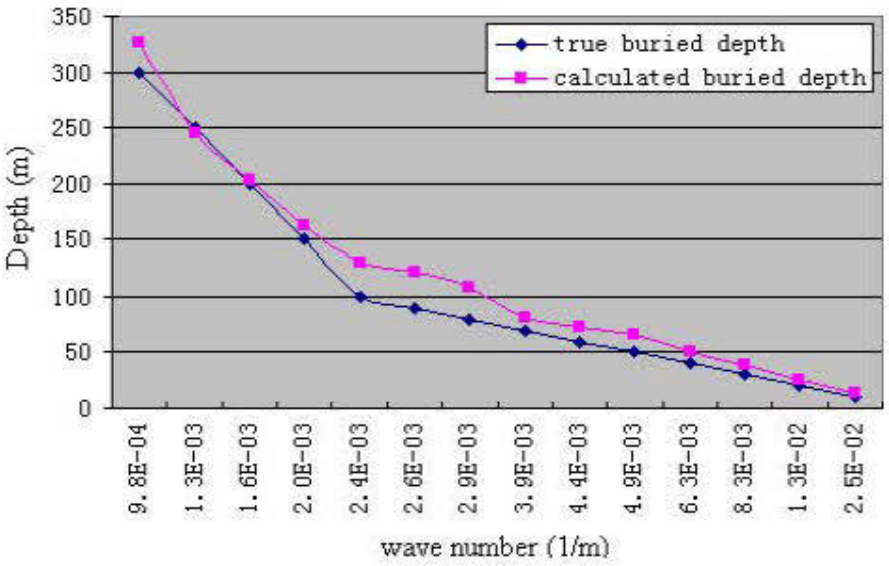

Figure 2.7: Correlation between depth and wave-number

2.5 Power spectrum analysis for complex models

Magnetic field is continuous in time and space. Through the Fourier transform, we approximate magnetic field by a periodic function, and then discrete it into Fourier series. The coefficients of Fourier series represent the intensities of susceptibilities or magnetizations at different frequencies at each station. Since they are complex amplitudes in the frequency domain, we call them as frequency spectrum. Complex calculation reduces the difficulty of integration operation in space.

Even a survey station only refers to one data (a value measured for one survey station), it contains also the contribution from sources under other survey stations around the observed point along a survey line. Therefore, we use a window moving from one station to another to scan magnetic anomalies, by assuming that major magnetic anomaly sources are located within the window width. Data $f_i(x)$ are observations in the i^{th} window. After the Fourier transform of data $f_i(x)$ we obtain $F_i(k_x)$ which is a set of complex amplitudes corresponding to different frequencies at one survey station (P). After processing N-times the same process is repeated at each survey station.

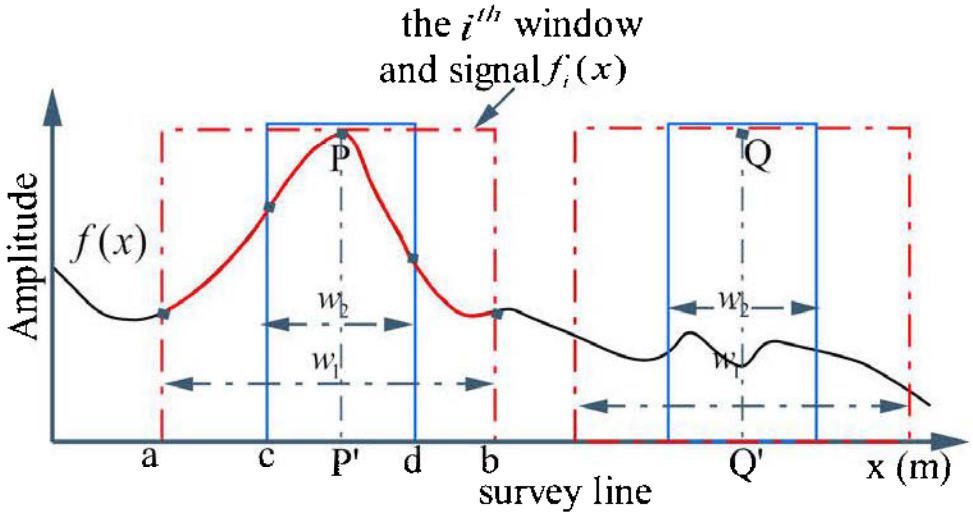

Figure 2.8: Sketch of space-wavenumber-domain analysis

Note: f(x) represents the magnetic field response (black curve); $f_i(x)$ represents the data within the i^{th} window (red curve segment).

The data $\{F_i(k_x)\}$ is in space-wavenumber domain. In our calculation, we used short-time Fourier transform (STFT, Jont B. Allen, 1977), and the results $\{|F_i(k_x)|^2\}$ are named power spectrum.

$$\begin{cases} f(x) \xrightarrow{STFT} F(x,k_x) \\ P(x,k_x) = |F(x,k_x)|^2 \end{cases} \tag{16}$$

Substituting eq.15 into eq.16 yields the imaging data in spatial domain and using symbol z to represent the depth h get the imaging results. Formula 17 is called the later **depth imaging**.

$$P(x,k_x) \xrightarrow{z=h(k_x)} P(x,z) \tag{17}$$

Where:

the survey line is along x direction;

h represents the depth of anomaly source;

k_x represents the wave-number.

One of the key questions is how to select the optimal width of window in STFT. In Figure 2.8, we hypothesize that main magnetic anomaly source is underneath the point P', and its response is mainly inside of the interval [a, b]. Therefore, the width of window must be enough big to include the entire main anomaly (red window). For example, the blue window, whose width is w_2, is not good because it cuts off part of data of the main response at survey station P'. At survey station Q', the blue window is better than the red window because the red window includes more than one anomaly, which makes the interpretation more complicate. The resolution of the STFT is thus windowing function dependent. A wide window corresponds to better frequency resolution but poor time resolution (or space resolution in spatial domain). A narrower window corresponds to good time resolution (space resolution in spatial domain) but poor frequency resolution. It determines whether there is good frequency resolution (frequency components close together can be separated) or good time resolution (the time at which frequencies change). WT (Wavelet Transform; Morlet, 1982; Chui, Charles K., 1992) and ST (S Transform; Stockwell R.G., Mansinha L., Lowe R.P., 1996; Stockwell, 1999), whose wavelet basis functions can adaptively reduce width of window as increasing frequency, are used for transforming the space-domain data into the space-wavenumber-domain data. Due to limited time, we only used STFT in our calculation.

In the following, we use two and three sphere models (Figure 2.9a_1 and 2.9a_2) to present a more complex situation as shown in Figure 2.9 (upper panel). The X-axis represents the survey line and units are in meter. The magnetic field inclination is $\pi/2$ and its azimuth is also $\pi/2$, the magnetic susceptibility of all five spheres is 0.2 SI, the magnetic field strength is 50000nT and other geometric parameters are indicated in Figure 2.9a_1 and 2.9a_2. The width of window function is 32 data points in STFT.

Through the power spectrum analysis (Figure 2.9b_1 and 2.9b_2), two different horizontal sources can be clearly distinguished at (0, 0) and (150, 0) respectively. Analyzing Figure 2.9b_2, it shows that the anomaly at location (0, 0) is deeper than the one at location (150, 0) because the anomaly is broader and also because it is associated with a small wave-number, which is consistent with the models. The power spectrum of Figure 2.9b_1 shows that there is a shallow source at location (0, 0) and that there is at least one deep source below due to the opening downward anomaly in small wave-number band. According to Figure 2.10b_1, we might also think

that it is a vertical elongated body or a vertical superposition of more than one magnetic body underneath location (0, 0), but in all cases, the possibility to indicate the existence of sources is taken into account.

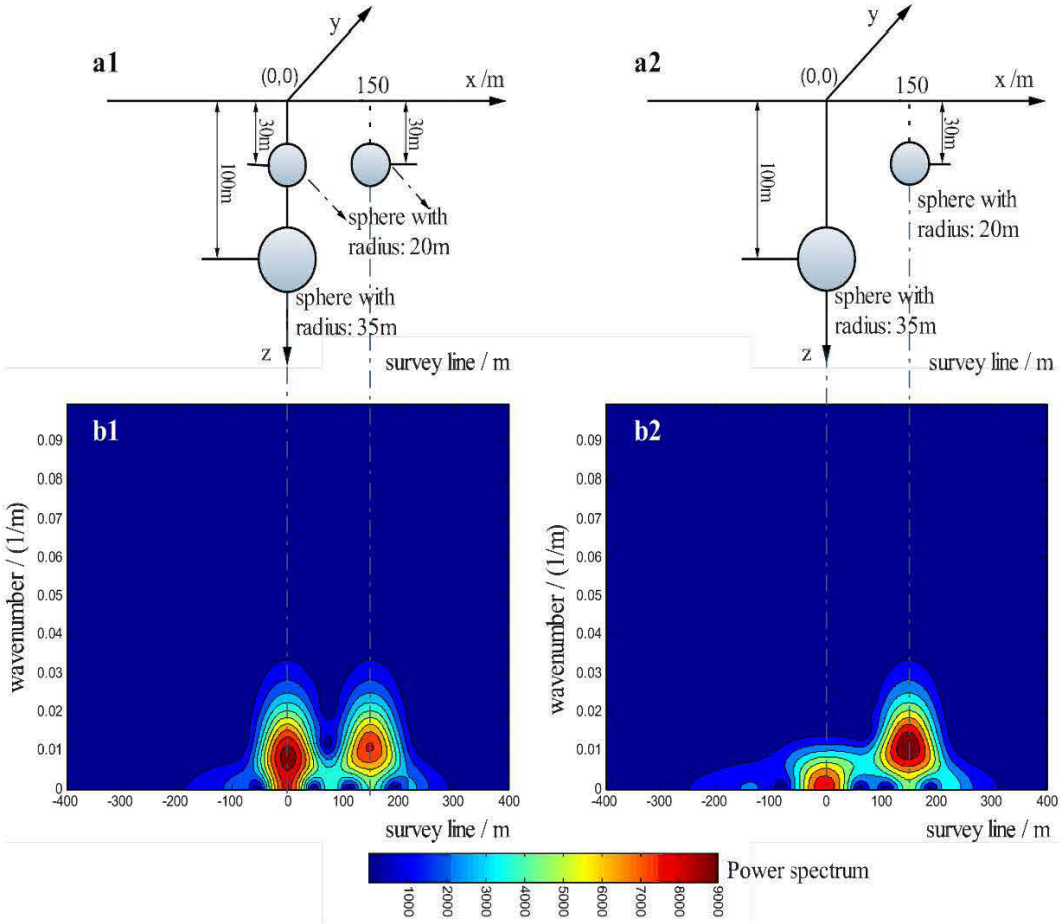

Figure 2.9: Complex models with three (a1) and two spheres (a2); STFT spectrum of their magnetic anomalies (b1 and b2)

2.6 Analysis of noise and the Gibbs phenomenon

2.6.1 Noise analysis

For the survey data in field, they are always affected by different types of noises, such as geological noise, random noise and human noise. We made two types of noises to analyze their impact on our method: random noises distributed uniformly and white Gaussian noises (WGN) (Kevin McClaning, et al. 2000) with different variances.

First, we calculate magnetic anomalies from two spheres shown in table 2.3. S_1 and S_2 represent the magnetic responses of shallow sphere 1 and deep sphere 2, respectively. Then, we add noises to the magnetic anomalies.

Table 2.3: List of parameters of two spheres

Parameters / Models	Radius (r)	Depth (h)	κ	M	I	A'
Shallow sphere 1	10m	30m	0.2SI	50000nT	$\pi/2$	$\pi/2$
Deep sphere 2	20m	100m	0.2SI			

2.6.1.1 Random noise distributed uniformly

This type of noise is distributed uniformly between the internal [0, 1]. The noise is constructed by the following formula.

$$N_{random} = random(0,1) * MAX(abs(S)) * NSR\% \tag{18}$$

Where,

N_{random} represents the random noise distributed uniformly,

$random(0,1)$ represents a random sequence distributed in the interval [0, 1],

S represents one of the signals (S_1, S_2),

$MAX(abs(S))$ represents the maximum of the absolute values of signal S,

NSR, is the noise-signal ratio of $random(0,1)$ to $MAX(abs(S))$

Analyzing Figures 2.10 to 2.17, the impact of random noise on the component with smaller wavenumber is smaller than that with bigger wavenumber. The figures show that the impact of random noise on the signal and spectrum of FFT become more and more serious as the NSR increases, and the DC components (direct current components) become more significant as

shown in Figures 2.12c to 2.14c and Figure 2.17c and 2.18c. This DC component may be caused by the bigger regional background field and other noise sequences whose average value are not equal to zero. When we deleted the DC component form the results, and got a serial of better results, they show that whole curves' shapes of spectrum of FFT do not be changed. Comparing the results of shallow sphere 1 and deep sphere 2, for the peer noise-signal ratio, the impact of random noise on shallow sphere 1 is much more serious than that of deep sphere 2.

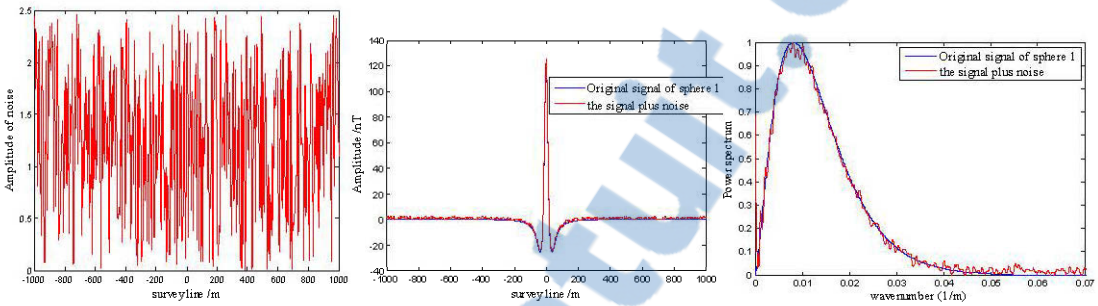

(a) (b) (c)

Figure 2.10: NSR=1%, (a) Random noise (NSR=1%), (b) original signal and the signal plus noise and (c) power spectrum of shallow sphere 1

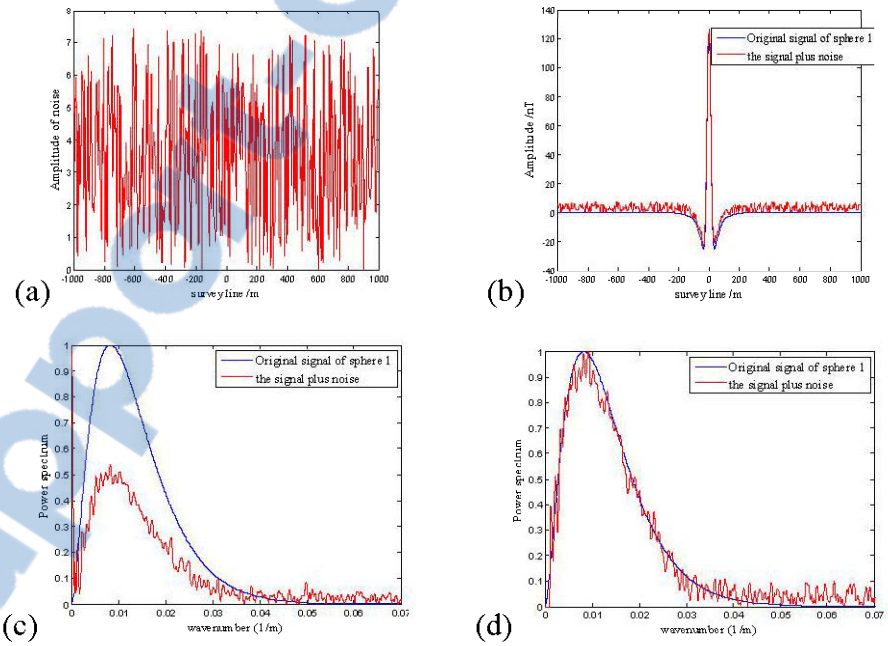

(a) (b) (c) (d)

Figure 2.11: NSR=3%, (a) Random noise (NSR=3%), (b) original signal and the signal plus noise, (c) power spectrum and (d) power spectrum with DC component removed of shallow sphere 1

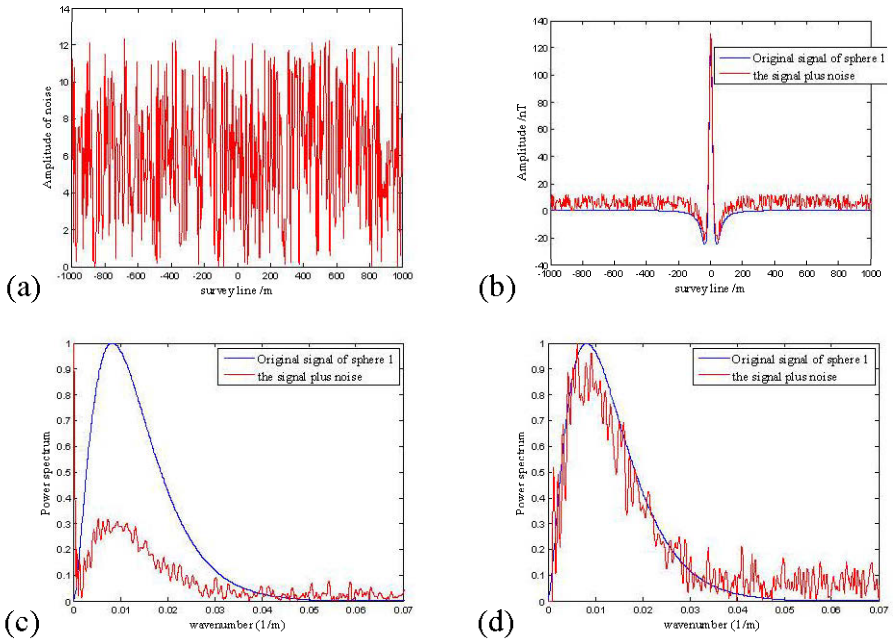

Figure 2.12: NSR=5%, (a) Random noise (NSR=5%), (b) original signal and the signal plus noise, (c) power spectrum and (d) power spectrum with DC component removed of shallow sphere 1

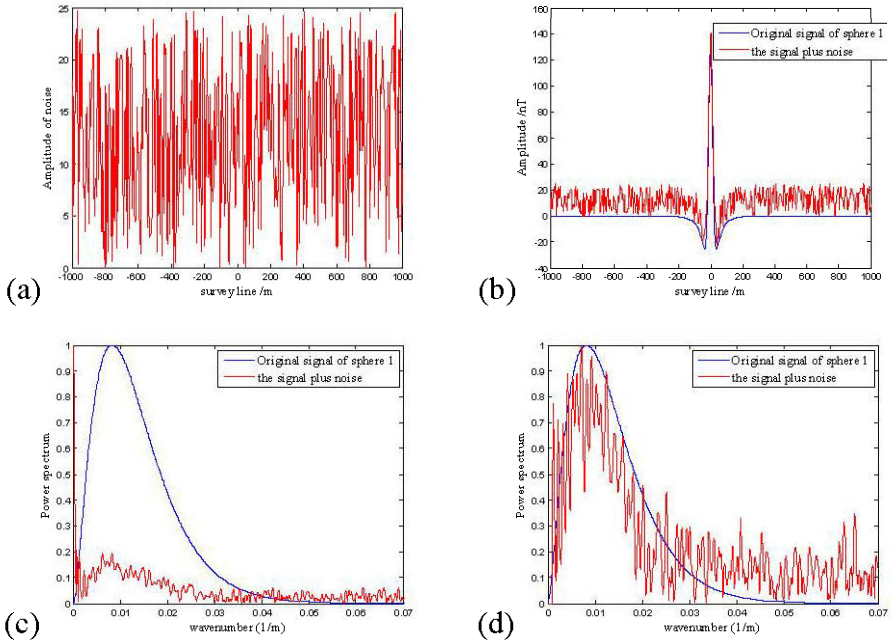

Figure 2.13: NSR=10%, (a) Random noise (NSR=10%), (b) original signal and the signal plus noise, (c) power spectrum and (d) power spectrum with DC component removed of shallow sphere 1

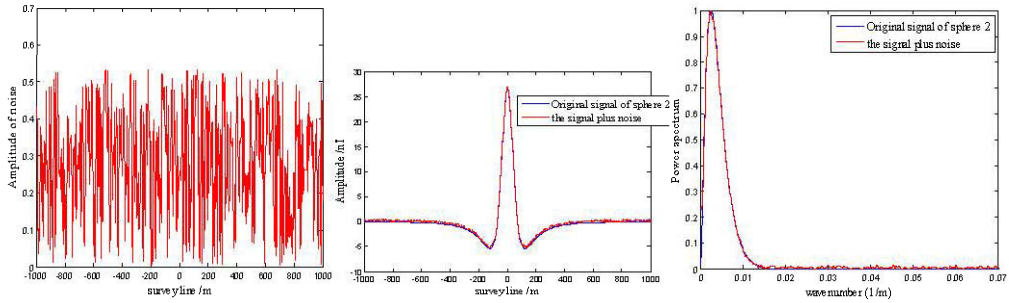

(a) (b) (c)

Figure 2.14: NSR=1%, (a) Random noise (NSR=1%), (b) original signal and the signal plus noise and (c) power spectrum of deep sphere 2

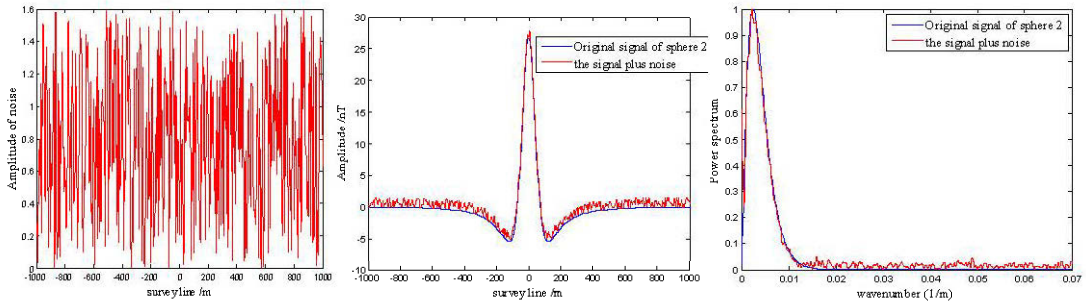

(a) (b) (c)

Figure 2.15: NSR=3%, (a) Random noise (NSR=3%), (b) original signal and the signal plus noise, (c) power spectrum of deep sphere 2

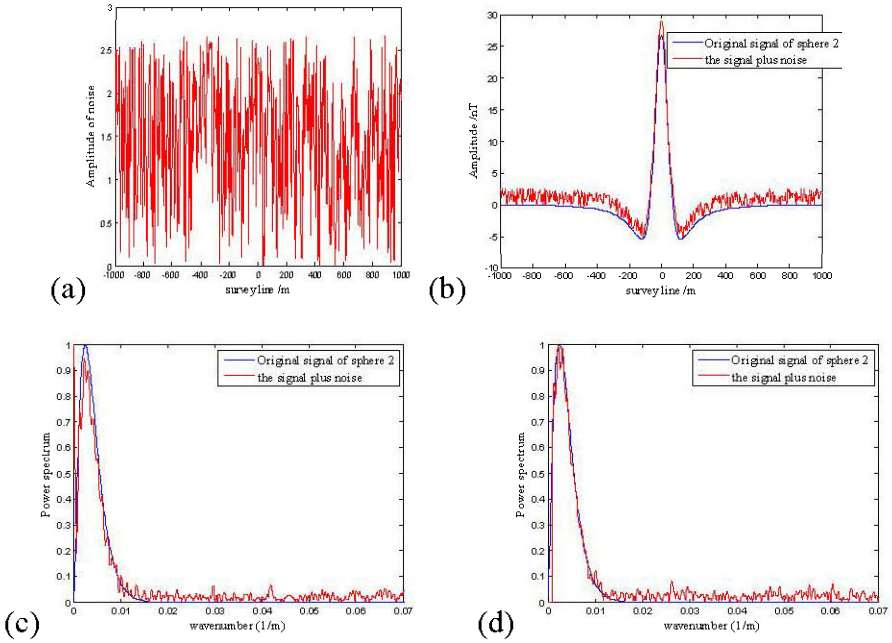

Figure 2.16: NSR=5%, (a) Random noise (NSR=5%), (b) original signal and the signal plus noise, (c) power spectrum and (d) power spectrum with DC component removed of deep sphere 2

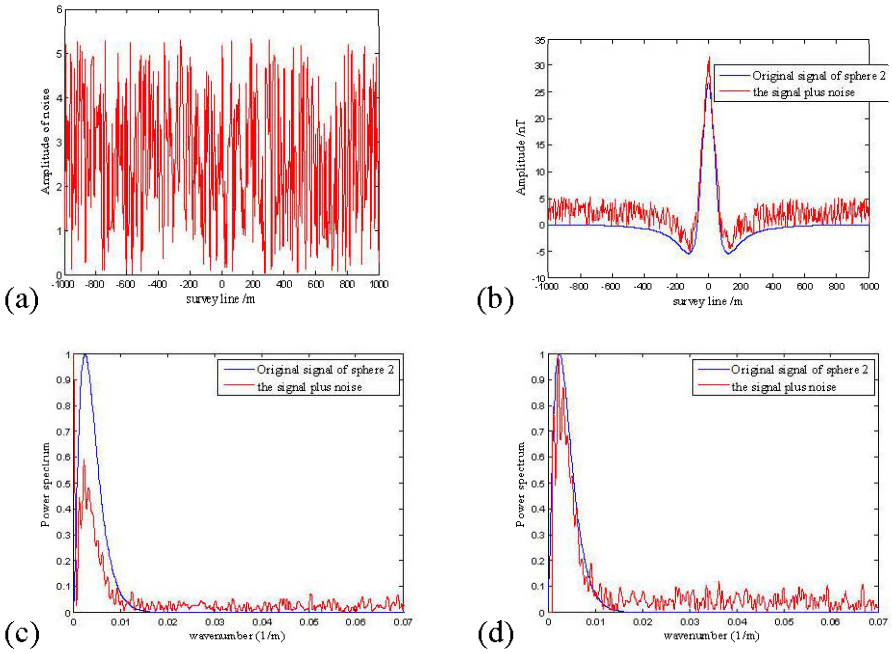

Figure 2.17: NSR=10%, (a) Random noise (NSR=10%), (b) original signal and the signal plus noise, (c) power spectrum and (d) power spectrum with DC component removed of deep sphere 2

2.6.1.2 White Gaussian noise (WGN)

A series of white Gaussian noises, which have the same average values of zero and different variances, are added to the magnetic anomalies to analyze their impact. The White Gaussian noises are constructed as following,

$$N_G = N0 * MAX(abs(S)) * NSR\% \tag{19}$$

Where,

S represents one of the signals (S_1, S_2),

$MAX(abs(S))$ represents the maximum of the absolute values of signal S,

NSR is the noise-signal ratio of $random(0,1)$ to $MAX(abs(S))$.

$N0$ represents the white Gaussian noise with the variance of 1,

N_G represents the white Gaussian noise with specific variances of $(MAX(abs(S)) * NSR\%)^2$

We also find the same principle with the impact of random noise on signal. The impact of WGN on the component with smaller wavenumber is less than that with bigger wavenumber, and this impact is more serious than that of random noise. Also for the peer noise-signal ratio, the impact of WGN on shallow sphere is much more than that on deep sphere. But for White Gaussian noise, there is no DC component due to than the average value of WGN equals to zero. When the noise-signal ratio is more than 8%, we even can't distinguish the spectrum of FFT for shallow sources.

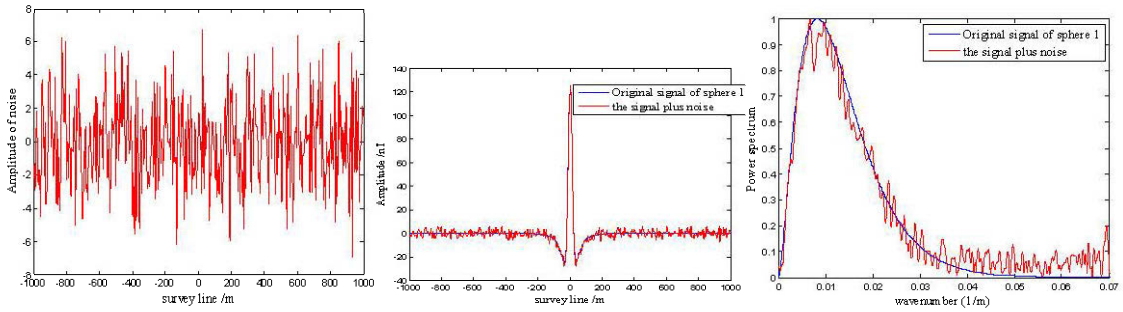

(a) (b) (c)

Figure 2.18: NSR=1%, (a) WGN (NSR=1%), (b) original signal and the signal plus noise, (c) power spectrum of shallow sphere 1

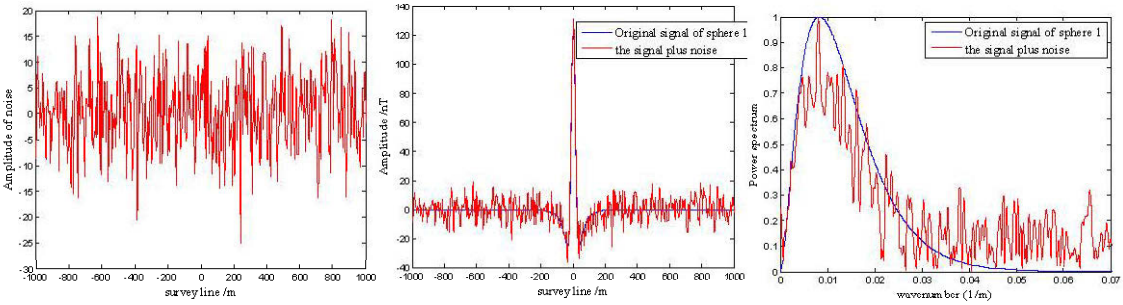

(a) (b) (c)

Figure 2.19: NSR=3%, (a) WGN (NSR=3%), (b) original signal and the signal plus noise, (c) power spectrum of shallow sphere 1

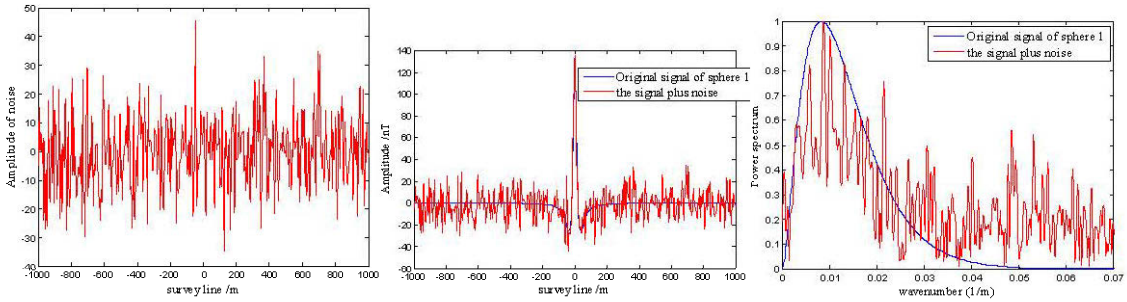

(a) (b) (c)

Figure 2.20: NSR=5%, (a) WGN (NSR=5%), (b) original signal and the signal plus noise, (c) power spectrum of shallow sphere 1

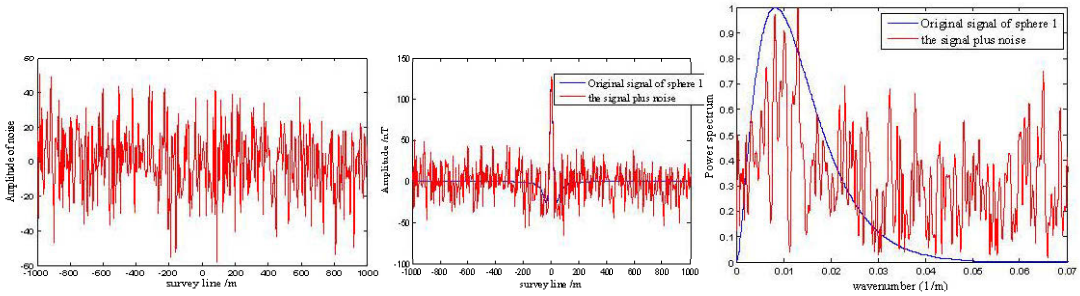

(a) (b) (c)

Figure 2.21: NSR=8%, (a) WGN (NSR=8%), (b) original signal and the signal plus noise, (c) power spectrum of shallow sphere 1

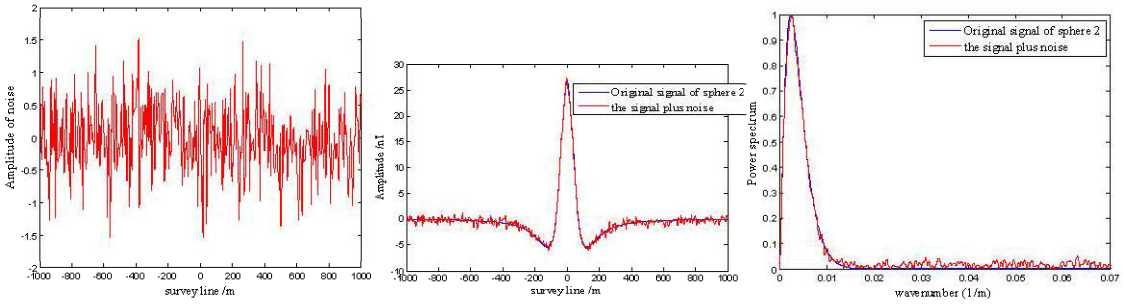

(a) (b) (c)

Figure 2.22: NSR=1%, (a) WGN (NSR=1%), (b) original signal and the signal plus noise, (c) power spectrum of deep sphere 2

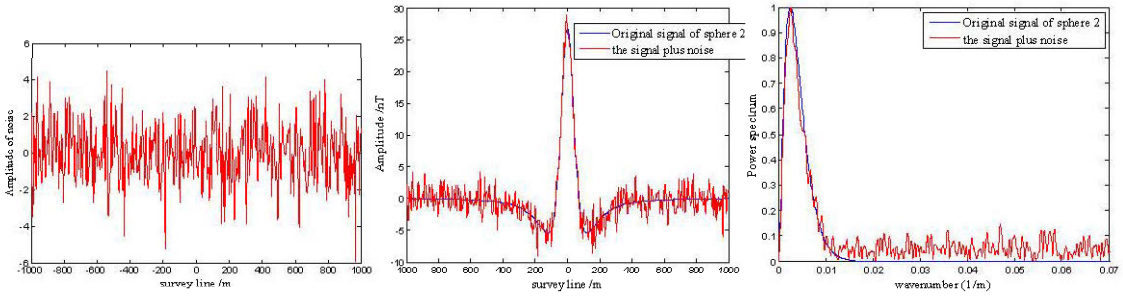

(a) (b) (c)

Figure 2.23: NSR=3%, (a) WGN (NSR=3%), (b) original signal and the signal plus noise, (c) power spectrum of deep sphere 2

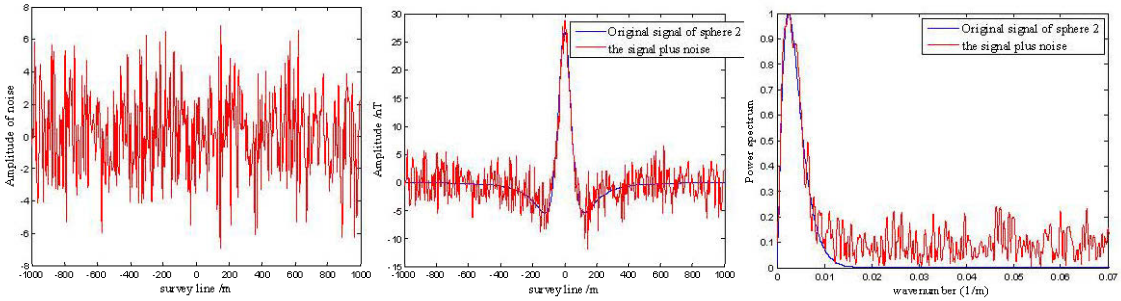

(a) (b) (c)

Figure 2.24: NSR=5%, (a) WGN (NSR=5%), (b) original signal and the signal plus noise, (c) power spectrum of deep sphere 2

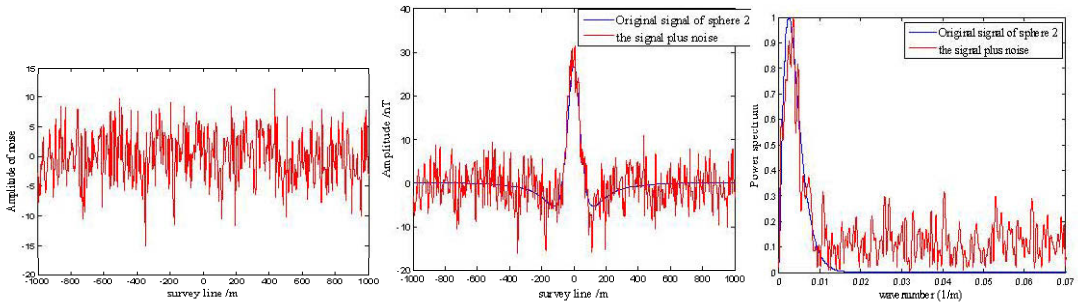

(a) (b) (c)

Figure 2.25: NSR=8%, (a) WGN (NSR=8%), (b) original signal and the signal plus noise, (c) power spectrum of deep sphere 2

2.6.2 Gibbs phenomenon and the choice of smooth window

An overshoot at the discontinuity occurs when using a Fourier series approximates a signal with a jump discontinuity, and this overshoot does not die out as the frequency increases. This phenomenon was noticed by A. Michelson (1898) and proposed by Gibbs (1899). Often we should consider a smooth window to smooth the discontinuous points. In order to get proper window functions, we studied a series of window functions to smooth the data to zeros and study their impact on signal, including Gaussian window, Blackman window, Hamming window, Hanning window and Bartlett window.

In our case, the signal used is the magnetic response of the deep sphere 2 in the section 2.6 of Chapter II, and add a constant signal with zero frequency to the signal in order to get the jump at the ends of the signal as shown in Figure 2.26. Using a series of window functions smooth the signal, we can get the spectrum of Fourier transform about original signals and the signal smoothed as shown in Figure 2.27 to 2.31.

Due to the jump discontinuity at the ends of signal, the Gibbs phenomenon is very serious as shown in the following figures. By using windows to smooth the signal (first applying windows on the survey data, and then computing the spectrum), the spectra (red curves) are much better than that of original signal (blue curves).

For the same sampling points, the power spectrum processed from the signal which is smoothed to zero by Gaussian window, Hamming window and Bartlett window are better than the Hanning and Blackman windows. For the same smooth window, a better spectrum can be obtained as the number of sampling points for smooth window increases. For the Gaussian window, as standard deviation of the Gaussian function increases, the spectrum become better as shown in Figure 2.27.

The principle to choose a smooth window is that enough number of sampling points and adjusting the parameters of window function make the window function smoother to zero. Also the sampling points of window function do not be countless so that it affects the computing speed.

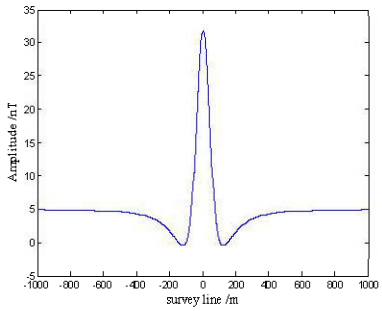

Figure 2.26: Signal with a constant signal with zero frequency

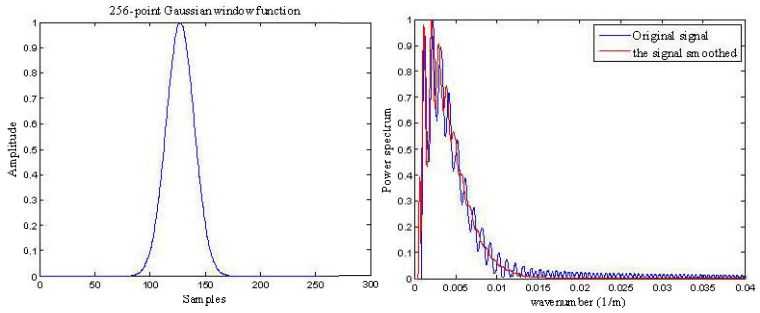

(a) 256-point Gaussian window, $\sigma = 0.1$

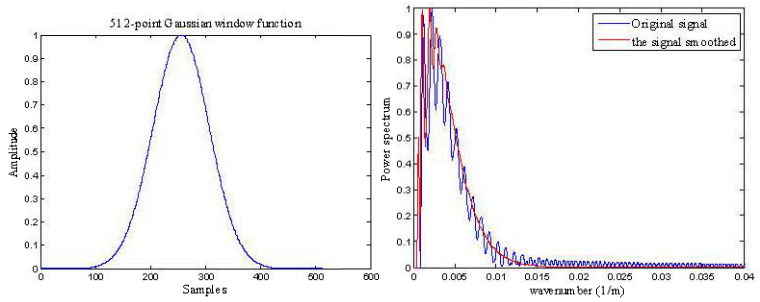

(b) 512-point Gaussian window, $\sigma = 0.1$

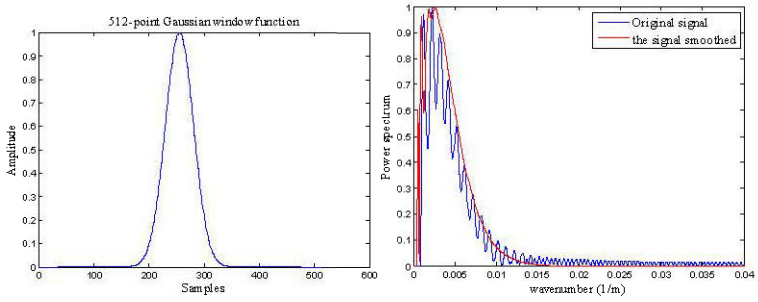

(c) 512-point Gaussian window, $\sigma = 0.2$

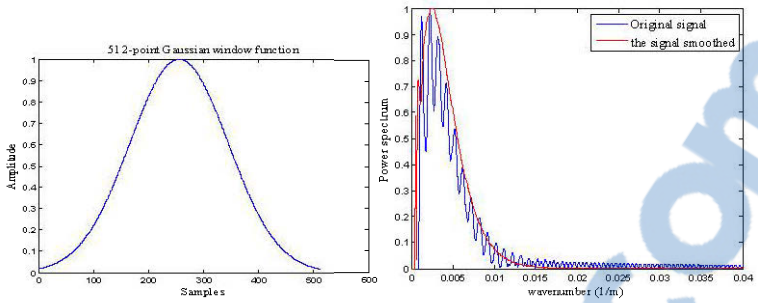

(d) 512-point Gaussian window, $\sigma = 0.35$

Figure 2.27: Analysis for the impact of Gaussian window on signal: window functions (left), spectrum of Fourier transform about original signals and signals smoothed (right)

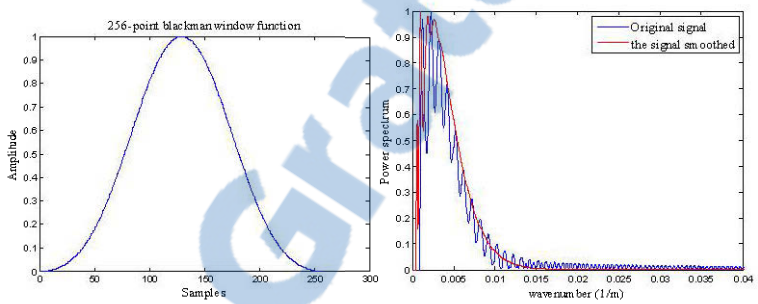

(a) 256-point Blackman window

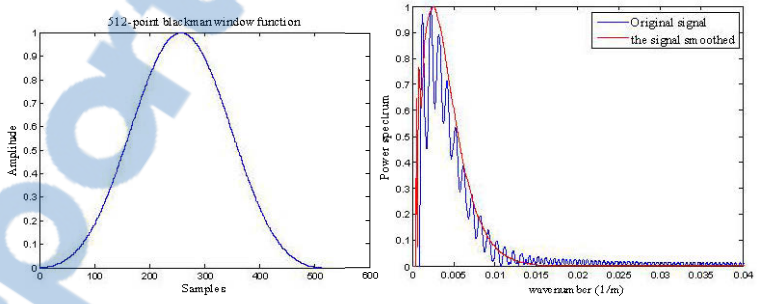

(b) 512-point Blackman window

Figure 2.28: Analysis for the impact of Blackman window on signal: window functions (left), spectrum of Fourier transform about original signals and signals smoothed (right)

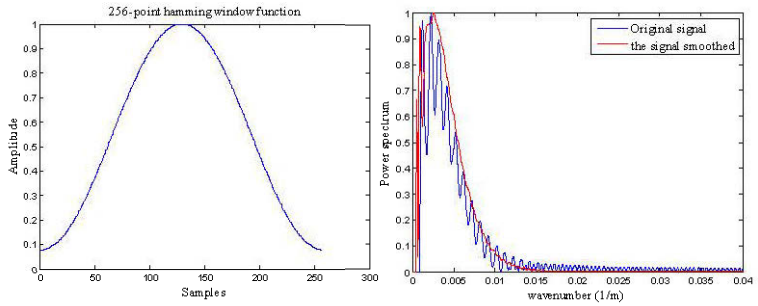

(a) 256-point hamming window

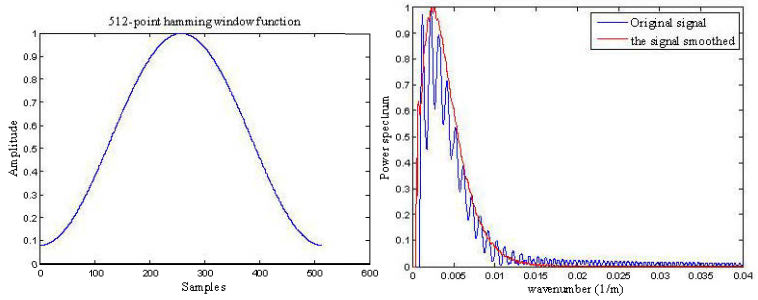

(b) 512-point hamming window

Figure 2.29: Analysis for the impact of hamming window on signal: window functions (left), spectrum of Fourier transform about original signals and signals smoothed (right)

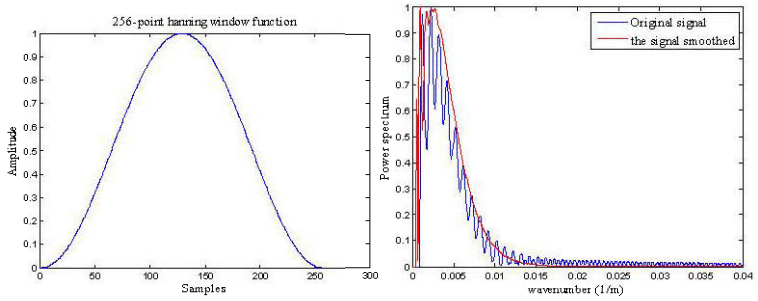

(a) 256-point hanning window

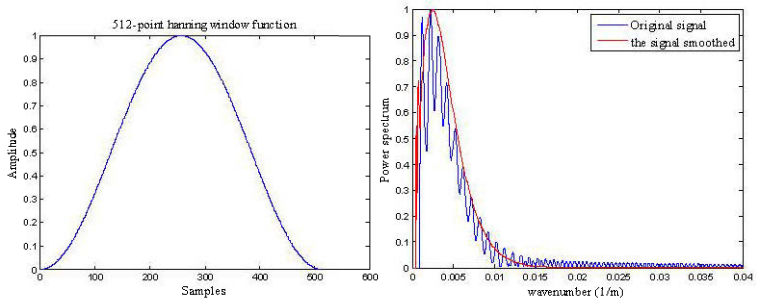

(b) 512-point hanning window

Figure 2.30: Analysis for the impact of hanning window on signal: window functions (left), spectrum of Fourier transform about original signals and signals smoothed (right)

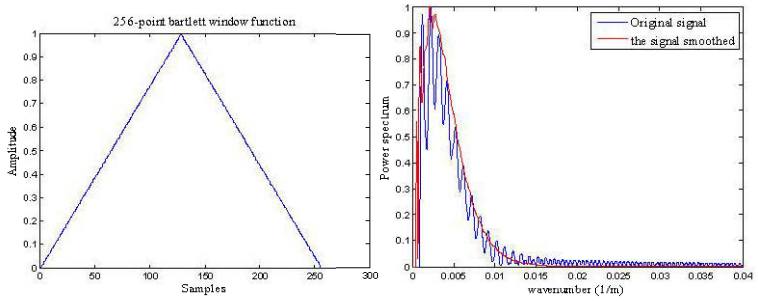

(a) 256-point Bartlett window

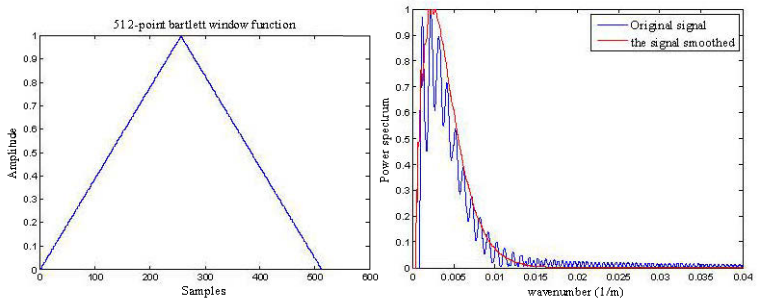

(b) 512-point Bartlett window

Figure 2.31: Analysis for the impact of Bartlett window on signal: window functions (left), spectrum of Fourier transform about original signals and signals smoothed (right)

2.7 Modeling test

We applied the new method to 5 synthetic models. The magnetic permeability of free space is $4\pi\times10^{-7}$ Hm^{-1} and the magnetic field strength is 50000nT. The different geometric parameters are shown in each model.

Model 1: As shown in Figure 2.32, all parameters of the two spheres are the same except the lateral position. For all of them, the azimuth of survey line is $\pi/2$, they are vertically magnetized (magnetic field inclination is $\pi/2$) and they have identical magnetic susceptibilities, which is 0.2 SI. Their depths are 30m, their radius are 20m. For smoothing the data, the width of window function is 32.

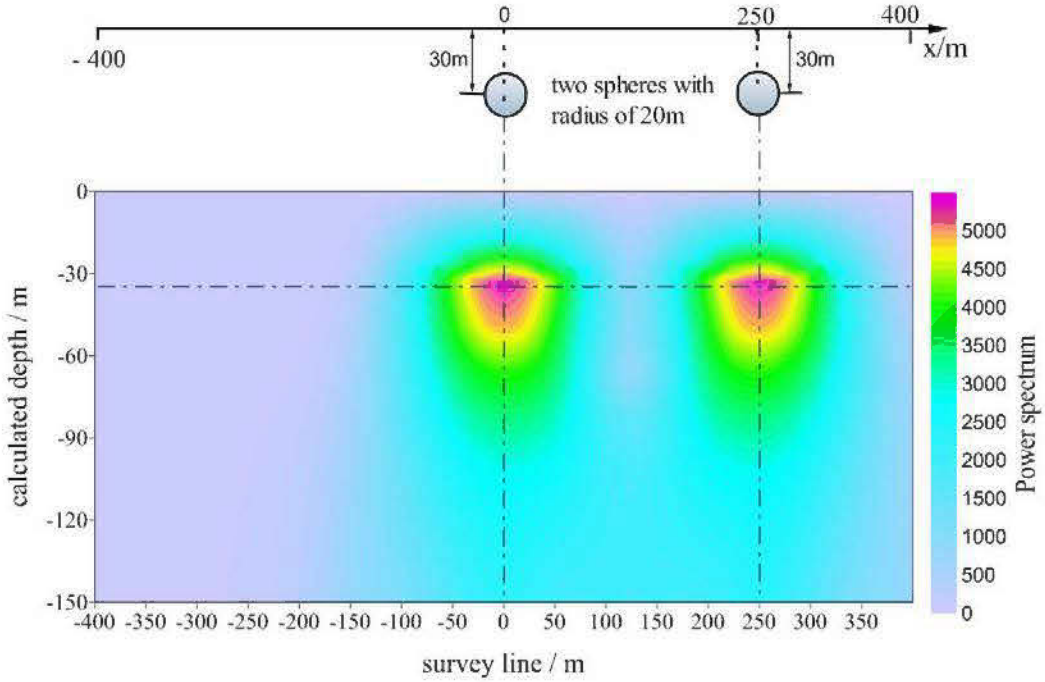

Figure 2.32: Model 1 (upper), the depth imaging result (lower)

Two anomaly sources are very well defined by their Power spectrum exactly at the same location shown by the model (Figure 2.32). The centre depths of the spectrum anomalies are about 35m; the error is about 5m (lower panel of Figure 2.32). We notice that the spectrum anomalies start at the depth of the model center.

Model 2: A deep sphere is added under one of the two spheres of the Model 1 (Figure 2.33) at location (x=0). Figures 2.33a to figure 2.33e are the depth imaging results with different window width. For all of them, the azimuth of survey line is $\pi/2$, they are vertically magnetized (magnetic field inclination is $\pi/2$) and they have identical magnetic susceptibilities, which is 0.2 SI.

From Figures 2.33a to 2.33e, the depth imaging results show that windows with smaller widths have a better horizontal resolution, and wider windows have better vertical resolution. In other words, smaller windows have a good expression to shallow anomalies, and bigger windows highlight the information of deep sources. In the results, some information what we don't interest in are magnified for specific window width, deep source and shallow source affect each other. Since we didn't consider the interaction between sources, we propose the optimal window width

is less than the half distance between two anomalies in order to avoid such false image (Figures 2.33d and 2.33e).

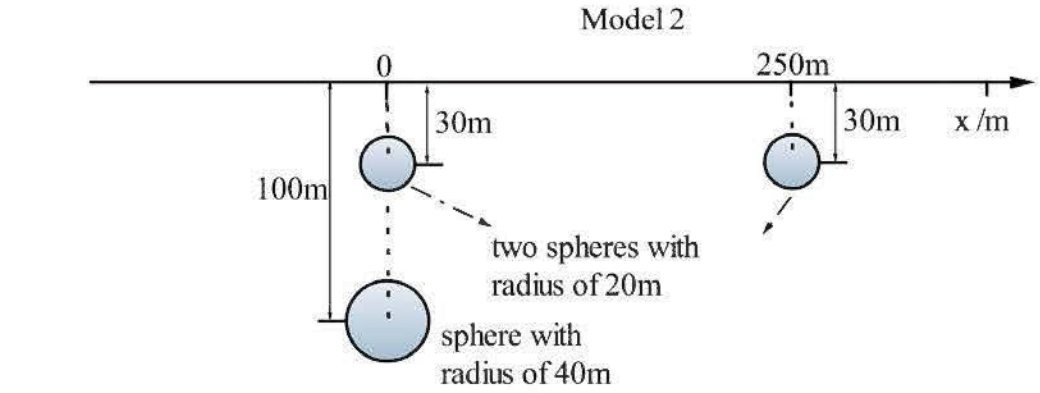

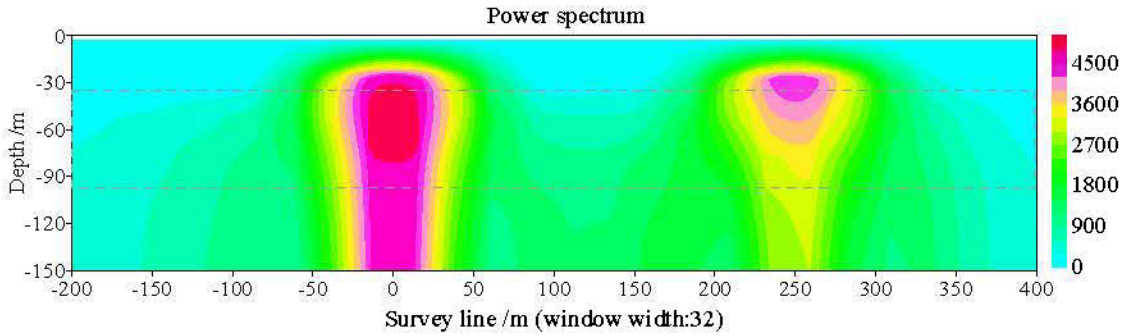

(a) Depth image with the window width of 32

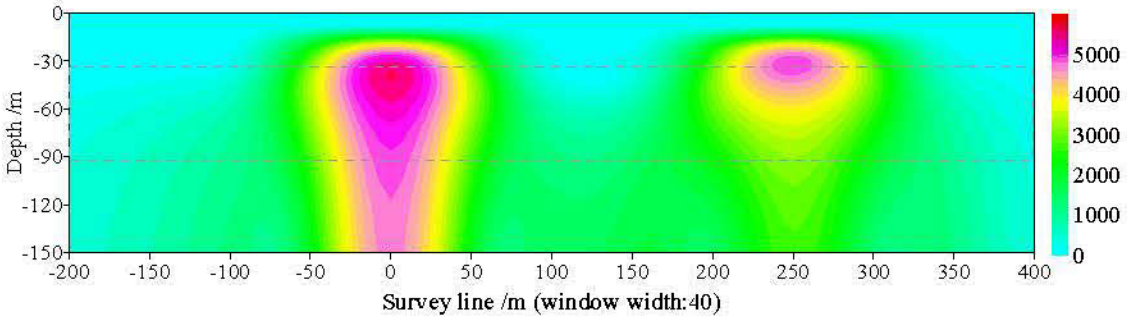

(b) Depth image with the window width of 40

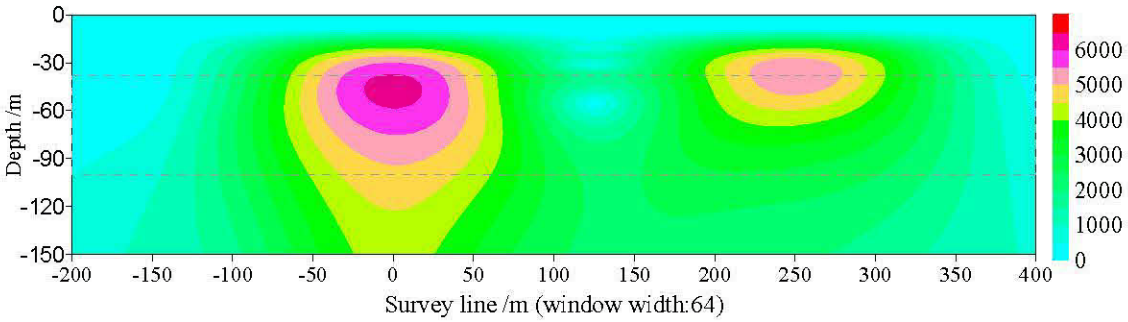

(c) Depth image with the window width of 64

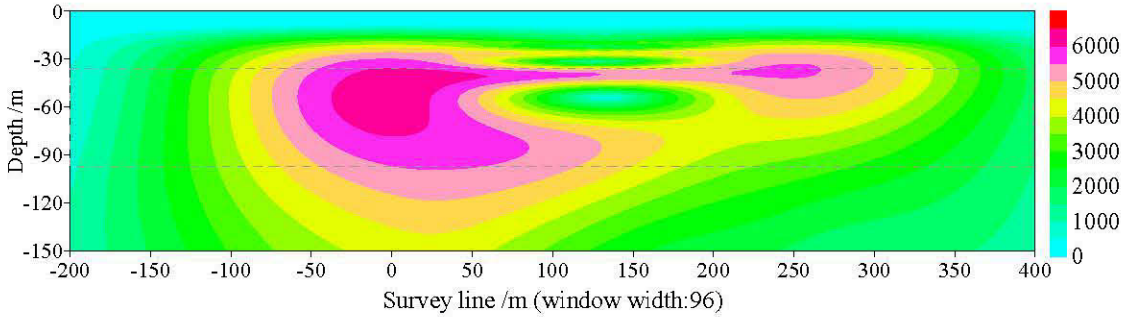

(d) Depth image with the window width of 96

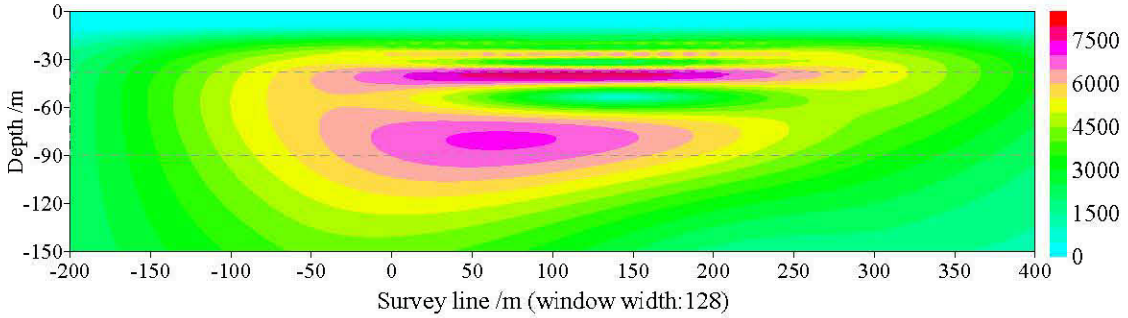

(e) Depth image with the window width of 128

Figure 2.33: Model 2 (upper) and their depth image (lowers)

Model 3: A small horizontal cylinder overlays a prism (model 3), they extend infinitely along the y axis. The magnetic field inclination is 30°, the azimuth of survey line is $\pi/2$, and they have identical magnetic susceptibilities, which is 0.2 SI. Model positions and their geometry parameters are shown in Figure 2.34 (upper map). For the model 3, the center of the cylinder is located at (0, 0, -50) and the center of the prism is located at (0, 0, -100). The depth imaging results with different window depths are shown in Figure 2.34 (lowers).

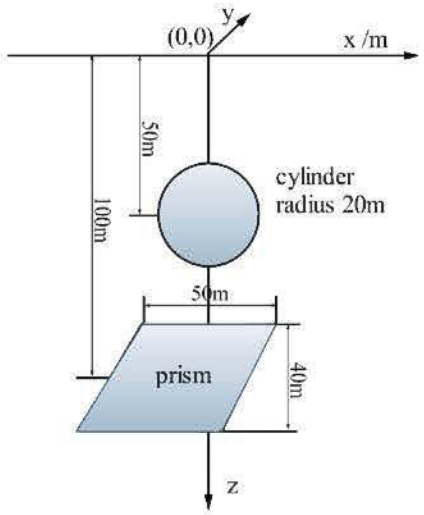

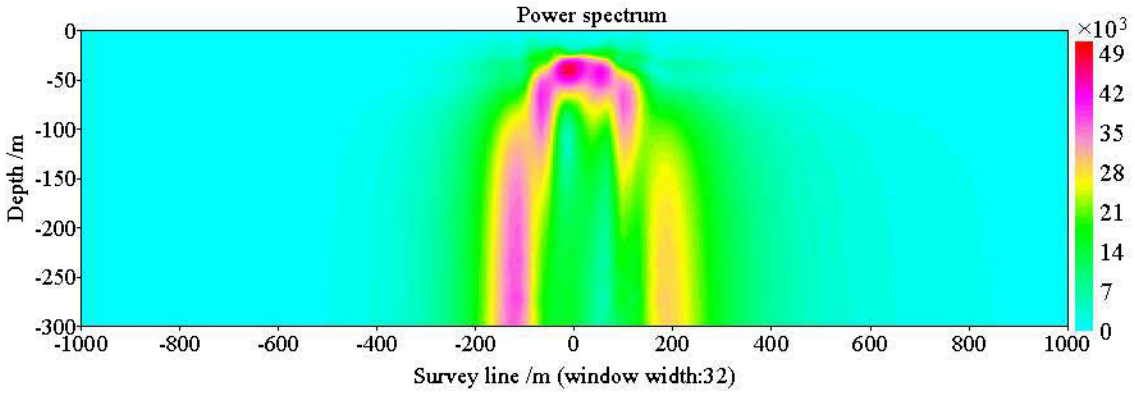

(a) Depth image with the window width of 32

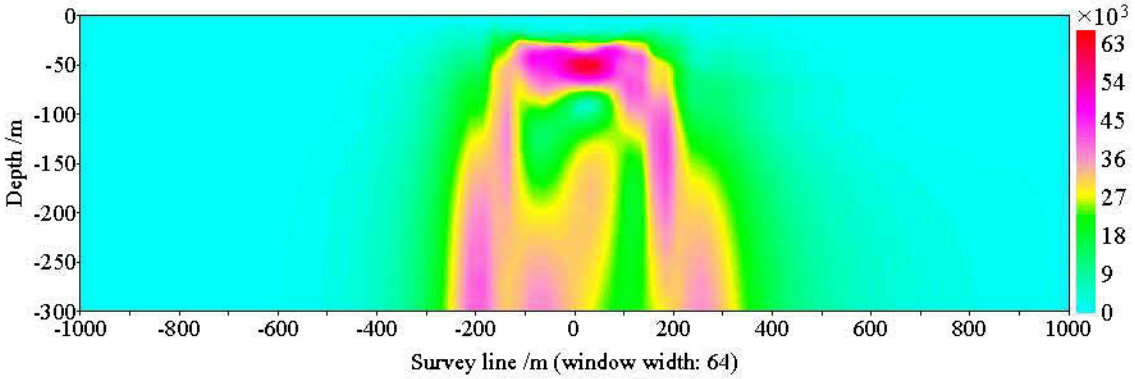

(b) Depth image with the window width of 64

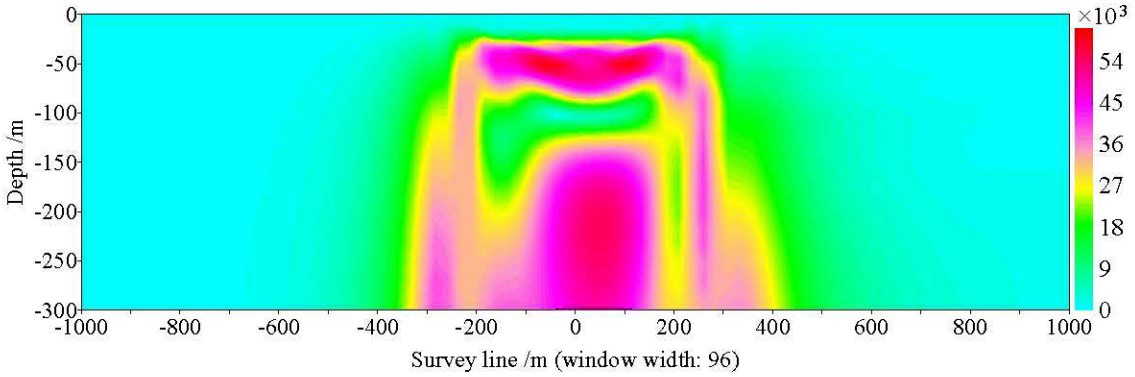

(c) Depth image with the window width of 96

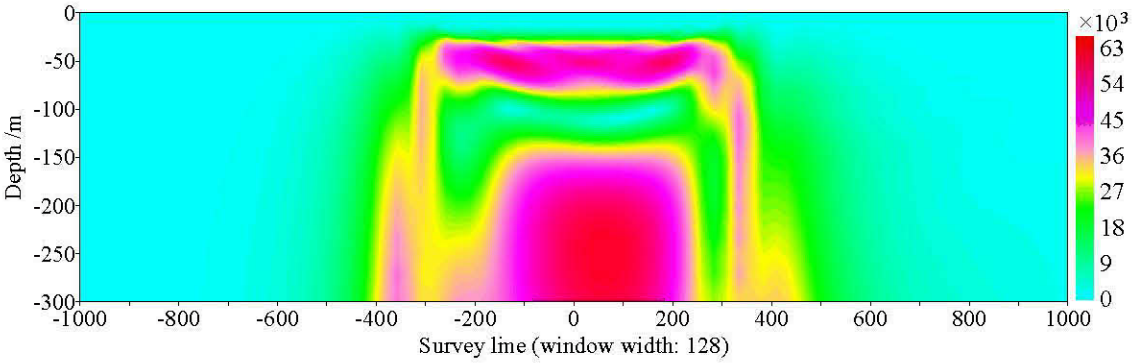

(d) Depth image with the window width of 128

Figure 2.34: Model 3 (upper) and Depth imaging (lower) for the superposition of the cylinder over (left) or under (right) the prism, window width is 256

From this model we show: since the amplitude of magnetic anomaly is inversely proportional to the cube of the distance between the source and the observation point, its power spectrum has low value. As shown in Figures 2.34a to 2.34d, we can define the horizontal position of the anomaly body exactly as the models designed. However, in the z-downward direction, we see a sphere-like spectrum anomaly on the top of another larger power spectrum. As width of window function increases, it becomes thicker, but dip extent almost do not changes. That's reasonable because increasing width of window function makes imaging data of many adjacent survey stations contain major same frequencies and power spectral. According to the usual shape of the spectrum of spheres (centered and closed), the top power spectrum of the model 3 indicates that there is another deep source, which has a different geometry from a sphere or a cylinder. We can see that the top power spectrum (Figures 34a to 2.34d) very well defines the depth of the cylinder (50m), and that the discontinuity depth of the Power spectrum (also the

top of the larger spectrum) corresponds to the center depth of the prism (100m), which is consistent with Model 3.

Model 4: A cylinder is located underneath the prism (model 4); they extend infinitely along the y axis. The magnetic field inclination is 30°, the azimuth of survey line is $\pi/2$, and they have identical magnetic susceptibilities, which is 0.2 SI. Model positions and their geometry parameters are shown in Figure 2.35 (upper map). For the model 4, the center of the cylinder is (0, 0, -150) and the center of the prism is located at (0, 0, -100).

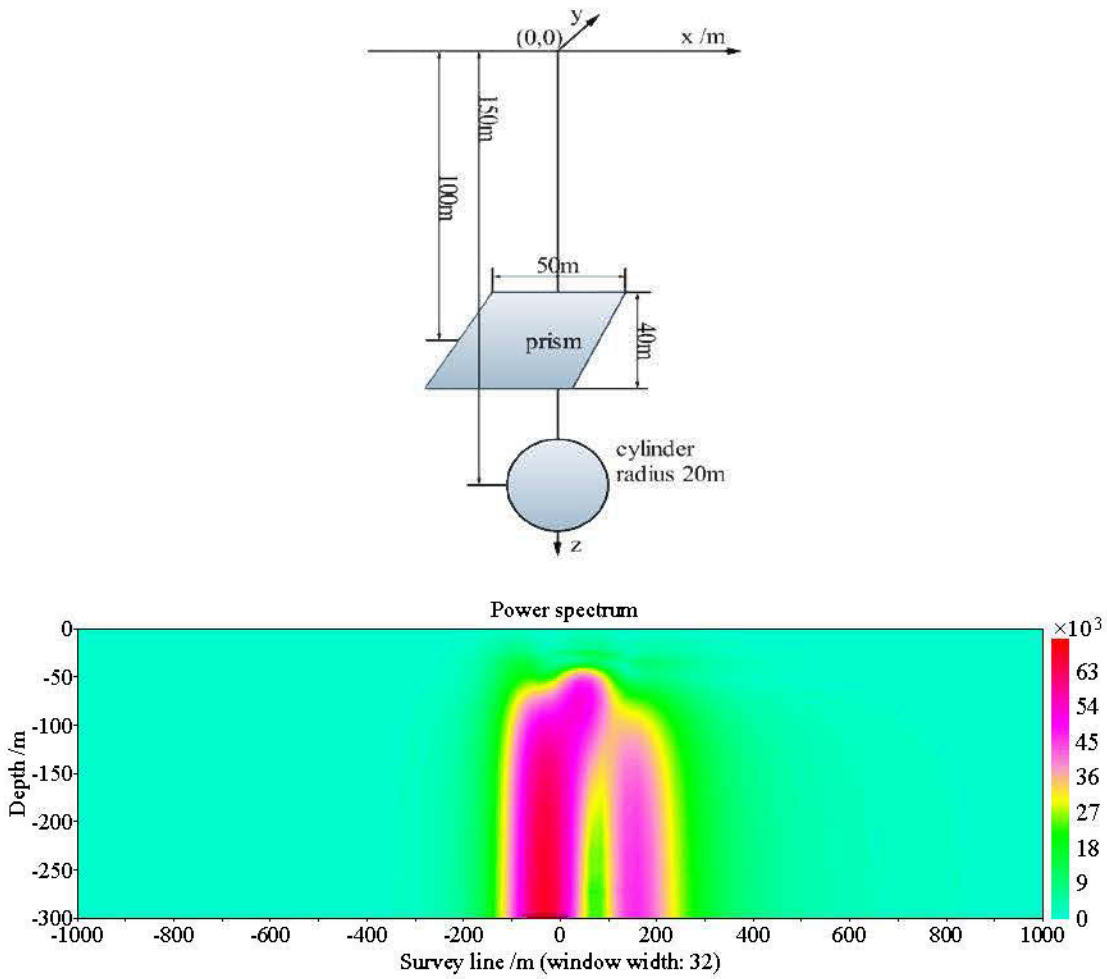

(a) Depth image with the window width of 32

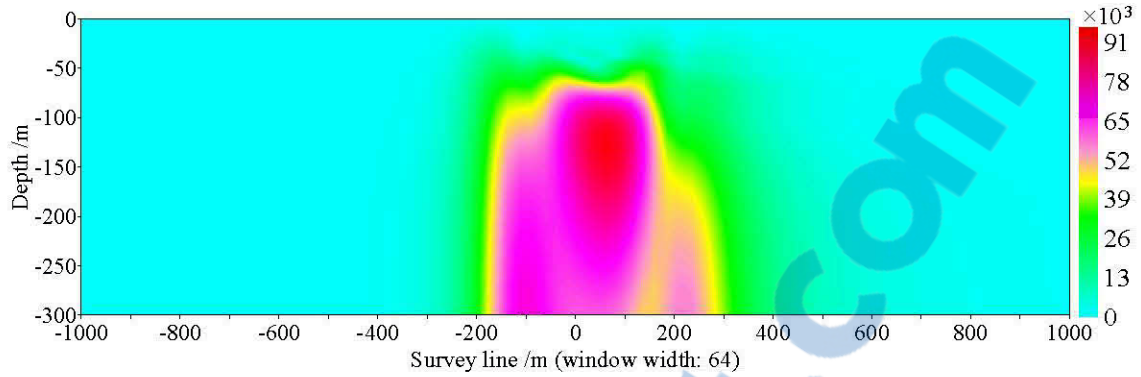

(b) Depth image with the window width of 64

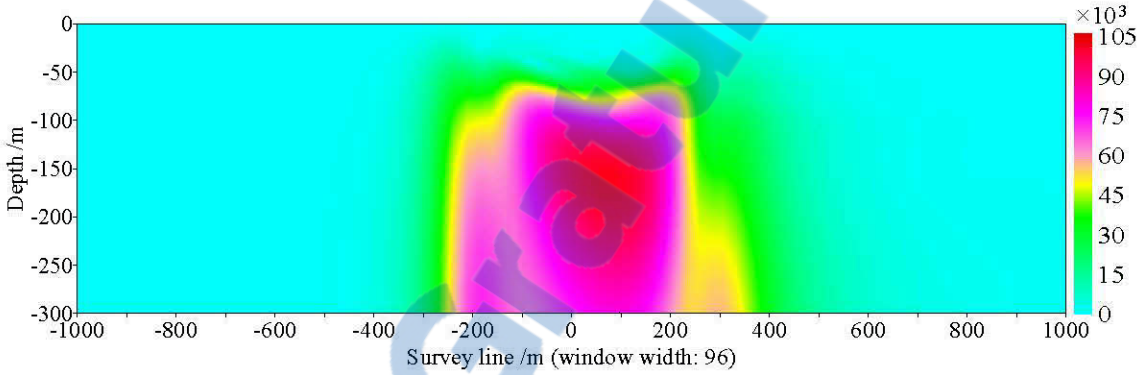

(c) Depth image with the window width of 96

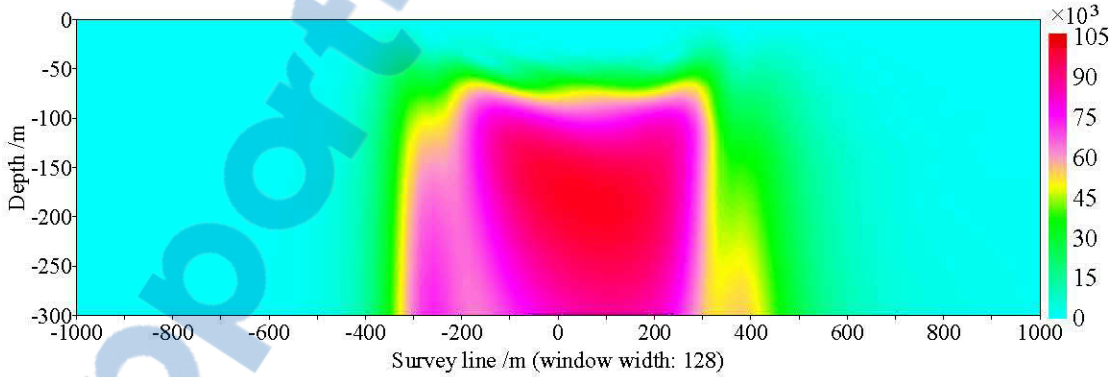

(d) Depth image with the window width of 128

Figure 2.35: Model 4 (upper) and Depth imaging (lower) for the superposition of the cylinder underneath the prism, window width is 256

On Figure 2.35, due to the fact that the prism has a larger volume than the cylinder, it dominates the Power spectrum distribution. The superimposition of a hidden deeper cylinder

could produce a false image of a single source leading to misinterpretation. However, the anomaly area recovers both sources between 100m and 200m of depth; it doesn't really affect the source depth estimation.

Model 5: As we were not able to distinguish the deep cylinder from the prism in the model 4, we put the cylinder at deeper place (200m), and increased its radius to 50m in order to get its response (Figure 2.36a, left). The magnetic field inclination is 30°, the azimuth of survey line is $\pi/2$, and they have identical magnetic susceptibilities, which is 0.2 SI.

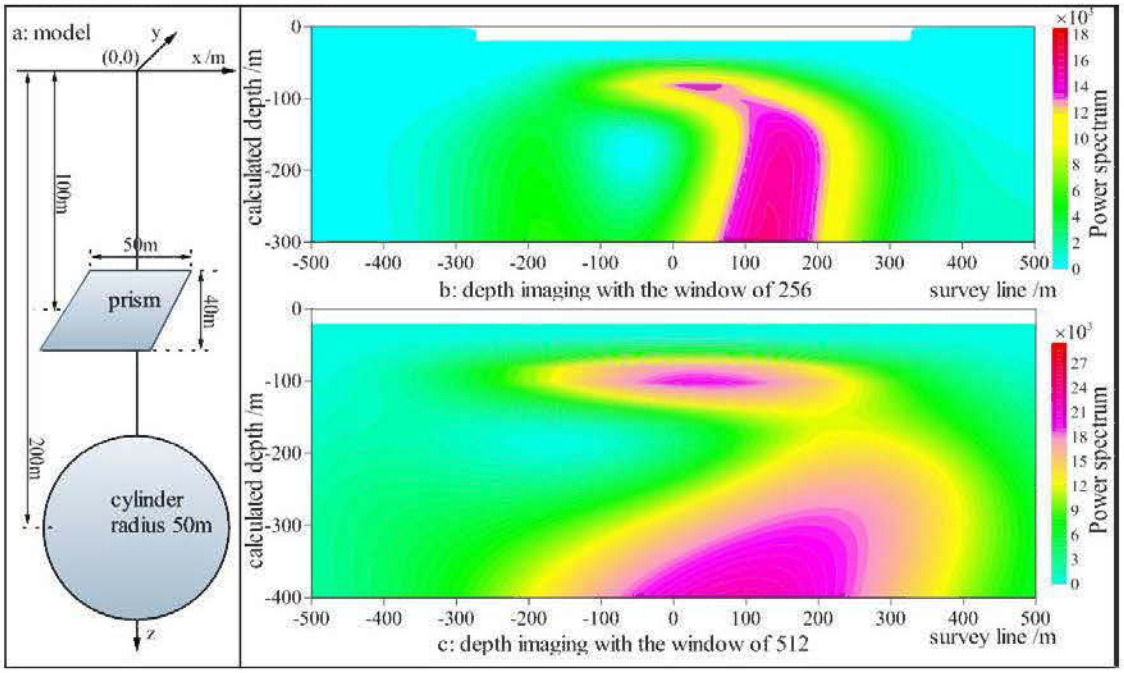

Figure 2.36: Model 5 (left) and Depth imaging (right) processed by window function with different width for the superposition of the cylinder and the prism

From Figures 2.36b and 2.36c, we can clearly distinguish two Power spectrum anomalous areas: a shallow one at the depth of 100m and a deeper one at the depth of about 200m. That's definitely proved that the depth imaging method can separate the vertical superimposed sources if they were apart in a certain depth.

But the source center position deviates from the location (x=0), we wonder that may be caused by the magnetic inclination which is 30° in this case. We modified the inclination as 90° (vertical magnetization) in the following model 6.

Model 6: The model is shown in Figure 2.36a, all the geometric and physical parameters are the same as the model 5 except the magnetic field inclination is 90°. The azimuth of survey line is $\pi/2$, and they have identical magnetic susceptibilities, which is 0.2 SI. The depth imaging results processed by window functions with different width are shown in Figure 2.37a to 2.37d.

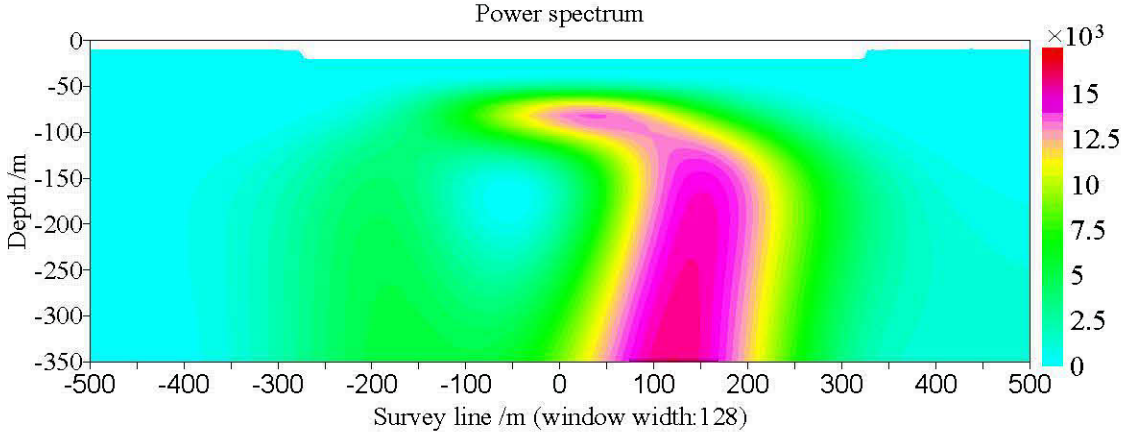

(a) Depth image with window width: 128

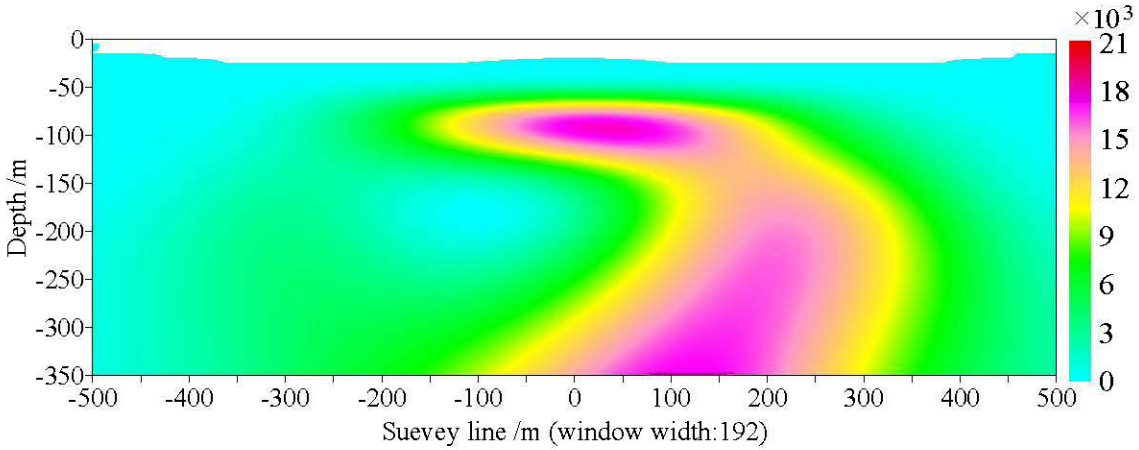

(b) Depth image with window width: 192

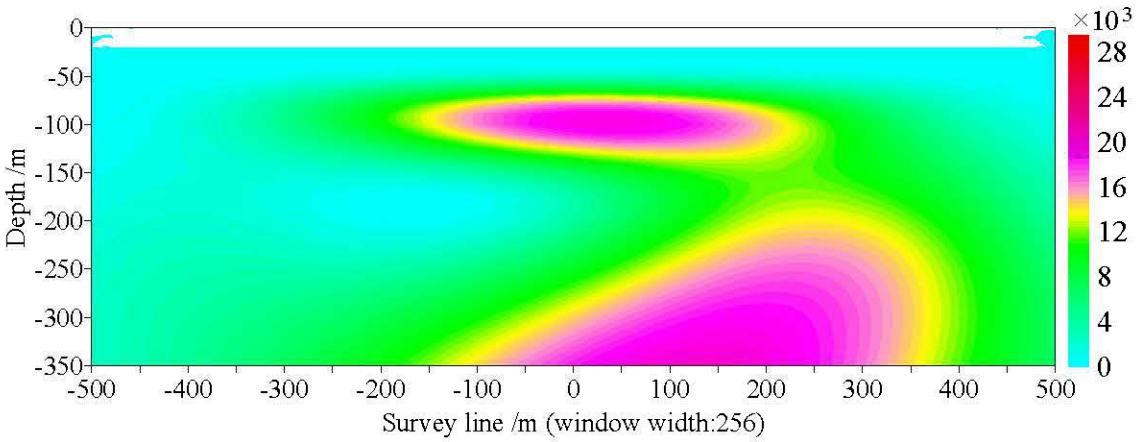

(c) Depth image with window width: 256

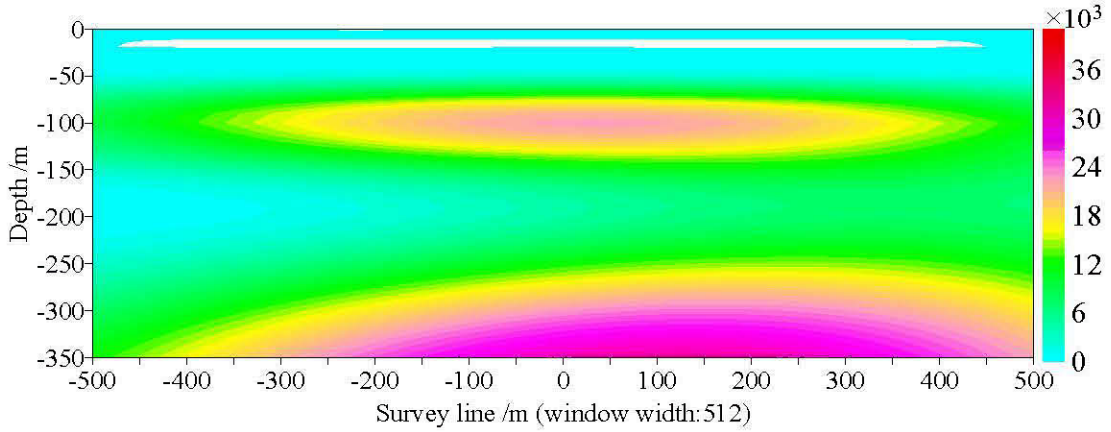

(d) Depth image with window width: 512

Figure 2.37: Model 6 (as shown in figure 2.37a) and Depth imaging results processed by window functions with different width for the superposition of the cylinder and the prism

We still got the same conclusions with the model 5: depth imaging method can separate the vertical superimposed sources if they were apart in a certain depth. For vertical magnetization anomaly, using small window can get the same resolution as the imaging results of oblique magnetization anomaly. Comparing Figures 2.36b and 2.37a, 2.36c and 2.37c, same resolution, but Figure 2.37a and 2.37c have smaller width of window. So for vertical magnetization case, the width of window must be narrower, or we will get a misinterpretation, such as shown in Figure 2.37d. Also, the model 6 proved that the position deviation is not caused by the inclination.

We would mention also that the depth imaging method has several weaknesses: 1) it over-estimated the volume of source and we need quantify more precisely the significant Power spectrum area; 2) users have to find out the suitable window length in order to have the best resolution, 3) for two dimensional inclined source, the estimated center position is offset.

2.8 Problem of equivalent source

The problem of equivalent source is well known in potential field data interpretation. However, we need to distinguish between two types of equivalent source: equivalent surfaces and equivalent bodies.

2.8.1 Equivalent surface or layer

Applying the equivalent source principle to potential field data processing was firstly discussed by Dampney (1969). As he mentioned in his paper: 'Bouguer anomaly measurements on an irregular grid and at a variety of elevations can be synthesized by an equivalent source of discrete point masses on a plane of arbitrary depth below the surface'. Subsequently, several techniques had been developed for first and second vertical derivation, upward- and downward-continuation, and directional derivation of the potential field (Needham, 1970; Emilia, 1973; Codell, 1992; Cooper, 2004; Li and Oldenburg, 2010; Kara et al., 2014, references therein). We reproduced such equivalent source through several examples (Figures 2.38a, 2.38b, 2.38c, 2.38d), which demonstrate that those equivalent sources are meaningless about the structural geology. The true model in Figure 2.38 is a magnetic cylinder. The center depth of the cylinder is 250m with magnetic susceptibility of 0.2SI, and its radius is 100m. Four groups of point sources located on a magnetic layer and they produced perfectly the cylinder's anomaly, but the susceptibility is different for each point source.

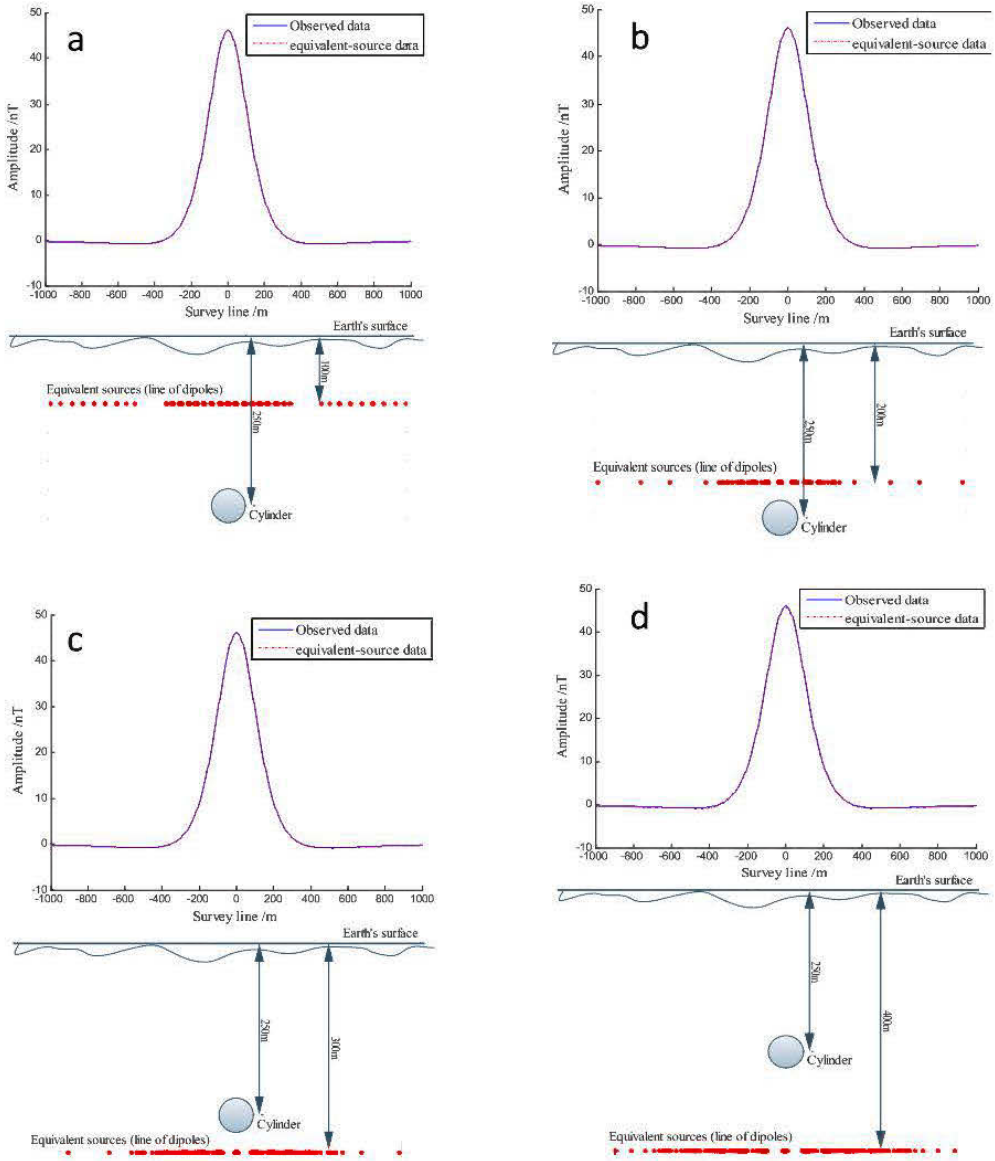

(a) Equivalent-source at the depth of 100m; (b) Equivalent-source at the depth of 200m

(c) Equivalent-source at the depth of 300m; (d) Equivalent-source at the depth of 400m

Figure 2.38: A cylinder at the depth of 250m and its equivalent-sources at different depth

2.8.2 Equivalent bodies

Equivalent bodies have specific geometric configuration, in this case, they are more close to real geology. For example, we search for abnormal bodies in mineral exploration, which have a specific location, limited size and different magnetic susceptibility or density (for potential

field) compared to surrounding rocks. The anomaly that is used in the interpretation represents mostly the local geological feature. If there were several abnormal bodies who might produce a same observed anomaly individually, this kind of equivalent source problem is totally different from the equivalent surface. The latter is to find an arbitrary mass distribution which generates a fixed potential, but the former is the problem to find the equal ratio of the magnetization or density and the distance between the observation point and the abnormal body. In order to study this type of equivalent sources, we did a series of modeling works and chosen several best fit models that are shown in the Table 2.4.

We design a shallow prism model (prism 1) and use its magnetic anomaly as our reference (red line on Figure 2.39). The survey line is E-W oriented and the strike direction of prism 1 is in the N-S direction. If there is an equivalent source which is deeper than the prism 1, in order to produce the same anomaly it should have higher susceptibility. At the depth of 200m, prism 2 and 3 (brown and green line respectively) show that the susceptibility has to be 10 times higher than that of the prism 1 to reach the same amplitude of the anomaly. Due to the effect of depth, they have larger width of the anomaly. Even we reduced the thickness of the prism 3 and compensated the amplitude of anomaly by extending its vertical length from 300m to 500m; its magnetic anomaly is still broader than the prism 1. We conclude that there is no such equivalent body from the point of view of petrophysics and geology, because the maximum of the magnetic susceptibility of Magnetite is 5.6 SI; of the Iron is 3.9 SI; of the pyrrhotite are 1.4 SI; of Maghemite is 2.5 SI and of Ilmentite is 3.8 SI (PP Handbook, Peter Blum, 1997). We inclined the prism 4 and 5 to see if the dip direction of prism makes impact on the anomaly. Indeed, it mostly affects the shape of the anomaly not the amplitude.

Table 2.4: Parameters of prism 1 - 3

Models / **parameters**	**Prism 1**	**Prism 2**	**Prism 3**	**Prism 4** Dipping to the east 75°	**Prism 5** Dipping to the west 75°
Strike length (m)	500	300	300	300	300
Dip extent (m)	500	300	500	500	500
Thickness (m)	100	40	30	30	30
Top location (m)	-100	-200	-200	-200	-200
Center depth (m)	-350	-350	-450	-450	-450
Susceptibility (κ)	1 SI	8 SI	10 SI	10 SI	10 SI
Magnetization (M)	52500nT				
Inclination (I)	75°				
Declination east of north	20°				
Altitude of survey line	0 (Earth's surface)				

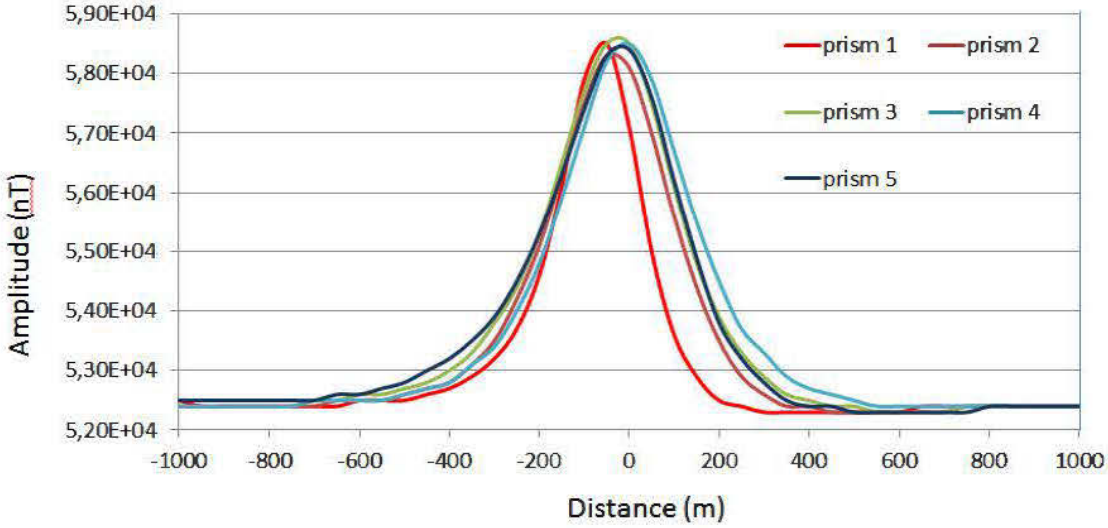

Figure 2.39: Equivalent source of prisms which have the same (or different) center depth with the causative anomaly (Prism 1)

Through following models (Table 2.5) we would like to show the different 2-D modeling and 3-D modeling. The prism model (prism 6) is our reference. By modifying the parameters of 2D polygonal body, we can easily find a 2D polygonal body which has approximate magnetic anomaly to the sphere (red line and yellow line in Figure 2.41) at the same depth, and the magnetic anomaly of 2D polygonal body almost is the same to the magnetic anomalies of 2D triangular body 1 and 2. In specific condition, the impact of 2D triangular body on the width of magnetic anomaly can be negligible as the bottom thickness of 2D triangular body decreases. Comparing sphere or 2D polygonal body to prism 6, their magnetic anomalies (red line and yellow line as shown in Figure 2.41) are still broader than the prism 6 (blue line), whether the magnetic source is 3 dimensional (sphere) or 2 dimensional (2D polygonal body), that means the magnetic anomaly for deeper body is still broader than that of shallow body as the same to the statements in above, this deserves to be further studied.

Table 2.5: Parameters of prism 6, sphere and 2D polygonal body

<table>
<tr><th>Models
parameters</th><th>Prism 6</th><th>Sphere</th><th>2D polygonal body, 2D triangular body 1 and 2</th></tr>
<tr><td>Strike length (m)</td><td>500m</td><td rowspan="2">Radius: 150m</td><td rowspan="5">Their geometries are shown in Figure 2.40.
Their center coordinates are approximate to (0,0,-600m)</td></tr>
<tr><td>Dip extent (m)</td><td>500m</td></tr>
<tr><td>Thickness (m)</td><td>100m</td><td rowspan="3">Center location
(x,y,z)
(0,0,-600m)</td></tr>
<tr><td>Top location (m)</td><td>-200m</td></tr>
<tr><td>Center depth (m)</td><td>-450m</td></tr>
<tr><td>Susceptibility (κ)</td><td>1 SI</td><td>1.4 SI</td><td>1.5 SI, 0.75 SI and 1.85 SI</td></tr>
<tr><td>Magnetization (M)</td><td colspan="3">52500nT</td></tr>
<tr><td>Inclination (I)</td><td colspan="3">75°</td></tr>
<tr><td>Declination east of north</td><td colspan="3">20°</td></tr>
<tr><td>Altitude of survey line</td><td colspan="3">0 (Earth’s surface)</td></tr>
</table>

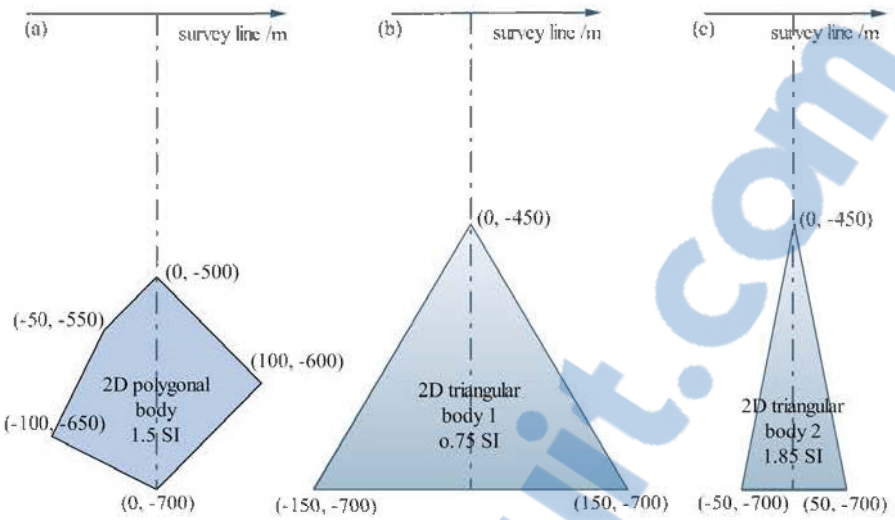

Figure 2.40: 2 dimensional (2D) polygonal body

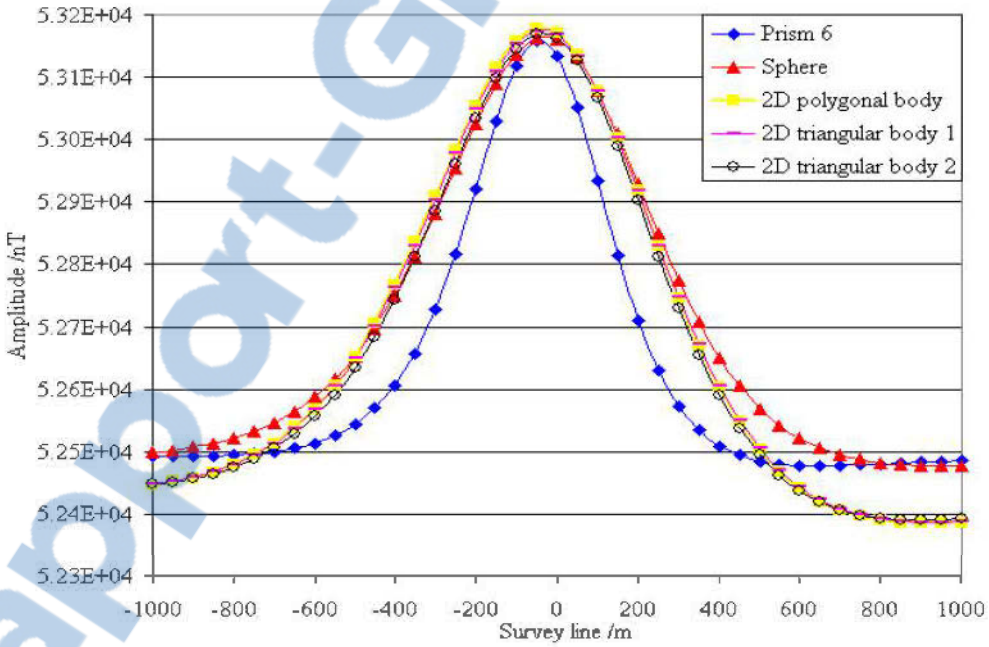

Figure 2.41: Responses of prism, sphere and 2D polygonal body

CHAPTER 3 CASE STUDY

We applied the depth imaging method to interpret the magnetic data over the Gallen mine in the Abitibi greenstone belt (within Québec province) of Canada.

3.1 Geology of the Gallen Volcanogenic Massive Sulfide Deposit

The Gallen deposit is located in the Dufresnoy Township, on the east shore of Lake Dufault, approximately 8 km northeast of Rouyn-Noranda. It was prospected in the late 1920s and early 1930s. MacDonald Mines produced 125t of Cu, 287000t of Zn, 52.7kg of Au, and 1550kg of Ag before 1959. Noranda Mines acquired a 51% interest in the property in 1961 and developed an open pit mine in 1981 (about 10m deep). Mining was suspended after only one year, with a total production of 156000t of ore grading 4.38% in Zn, 33.1g/t of silver, and 1.1g/t of gold (Trudeau, 1984). From July 1997 to July 2000, 2.4Mt of ore were extracted from the open pit, the bottom depth is approximately 88m with an average grade of 4.8% in Zn. In total, 4.1Mt of ore were extracted from the Gallen Mine by underground and open pit mining (Guimont and Riopel, 1998; Riopel, 2001). Since the cessation of the last period of exploitation in 2000, the open pit has been filled with acidic water (pH=2.35) to depths of 15 to 88m.

Figure 3.1 is the regional geology map of Gallen area. The red square indicates our study area, and its local geology is shown in Figure 3.2. The mineralization of Gallen is mainly composed of pyrite and sphalerite, type of the volcanogenic massive sulfide. It situates in a felsic volcanic terrain composed of rhyolites whose composition varies from dacite to andesite. Two types of intrusions disturbed the rhyolite formation. They are the granodiorite of Lac Dufault (Figure 3.1) and porphyritic felsic intrusion directly around the Gallen deposit (Figure 3.2). The north contact between the Lac Dufault granodirite and the rhyolite is dipping to the south (cross section A-B). According to simplified geological cross-section (Figure 3.2), the main lens of the deposit overlies the rhyolite formation.

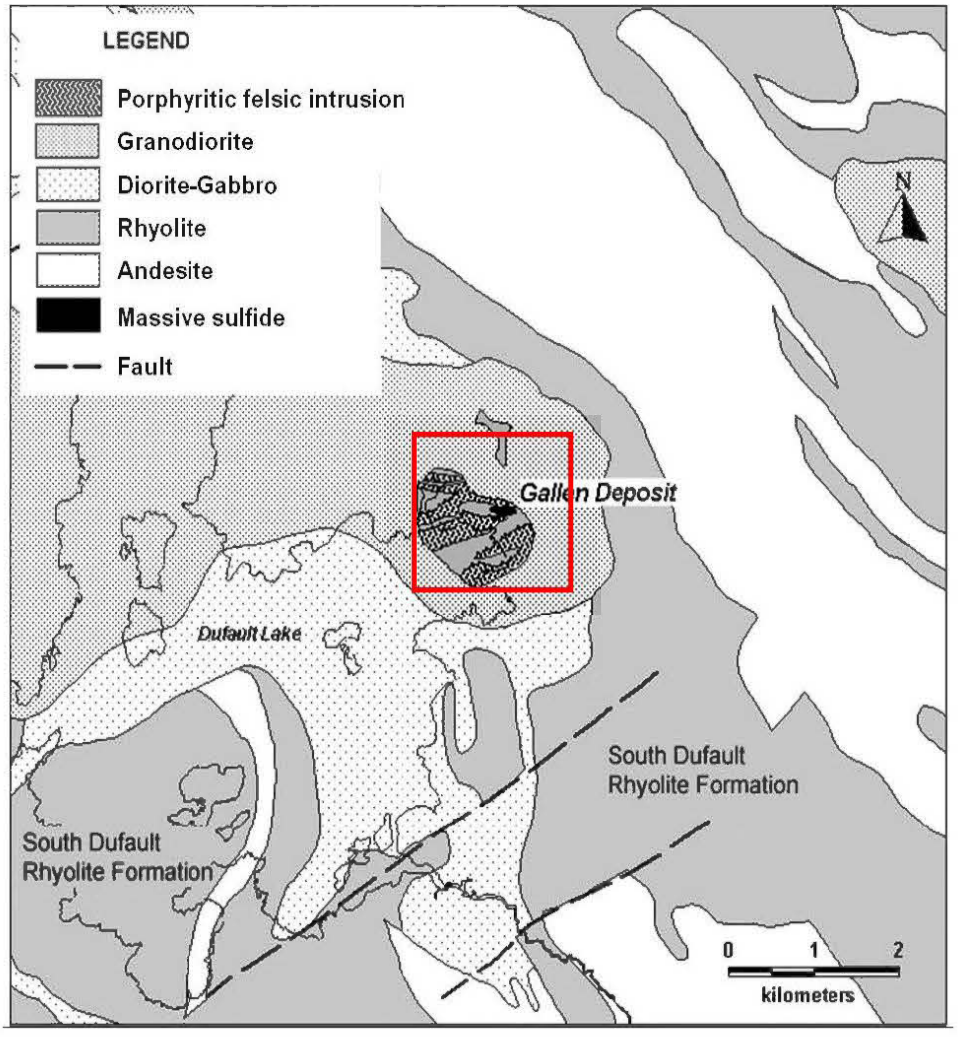

Figure 3.1: Regional geology map of the Gallen area (Cheng et al., 2007).

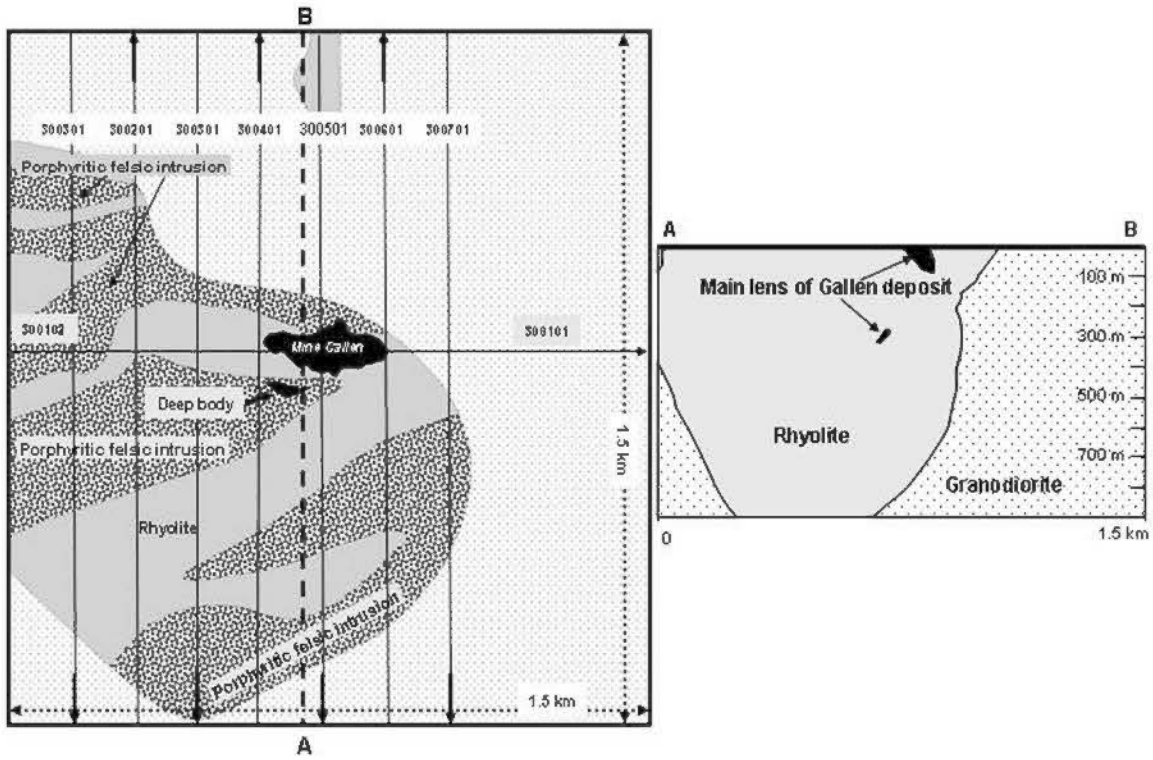

Figure 3.2: Detail geological map around the Gallen deposit, overlapped by magnetic survey lines with flight direction over the Gallen deposit (left). The geological cross-section along line A-B (right, Cheng et al., 2007)

3.2 Magnetic data description

The magnetic data used in this study mainly come from the MEGATEMII survey (Fugro airborne surveys), collected in 2003 using a Scintrex CS-2 single cell cesium vapour, mounted on a Dash-7 aircraft, measuring the total intensity of the earth's magnetic field in units of 0.01 nT at intervals of 0.5 sec. Figure 3.3 shows the measurement system's configuration.

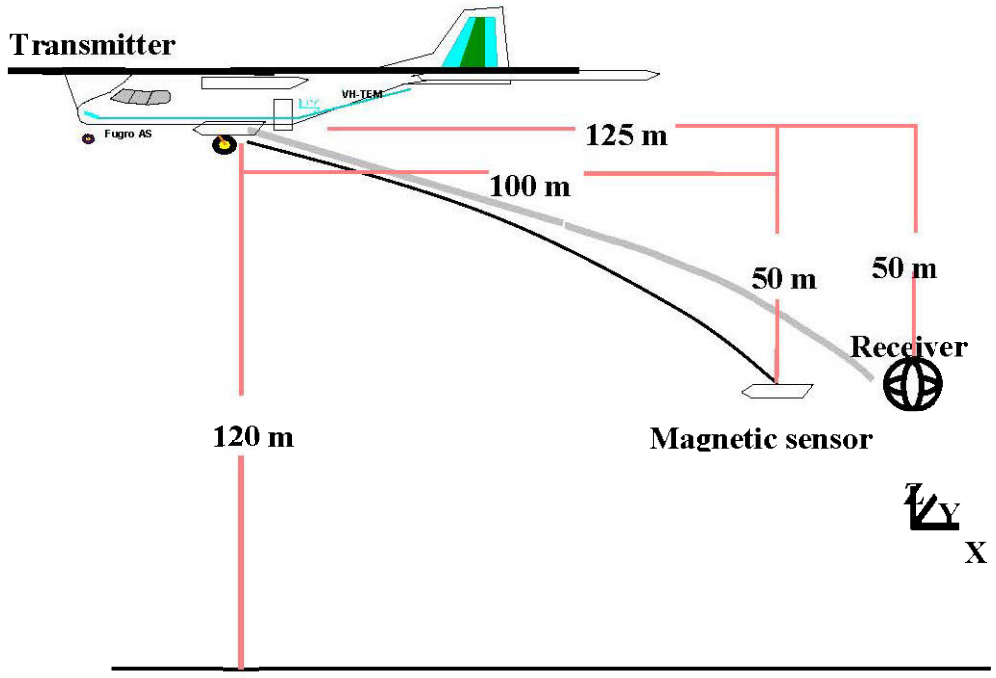

Figure 3.3: Survey system and its configuration (Cheng et al., 2007)

The survey was flown at a mean terrain clearance of 120m. Altitude was not to exceed 140m from nominal over a distance greater than 20km. The noise envelope on the magnetic data did not exceed ± 0.25 nT in the whole survey. Magnetic diurnal deviations were not to exceed 10nT as measured from a chord of 30 seconds duration. The magnetic sensor is located in a bird approximately 100m behind the aircraft at a height of 70m; an electromagnetic signal receiver is located in a second bird towed 130m behind the aircraft at a height of 70m above ground.

The magnetic data are processed by Geosoft and removed out a linear regional trend, and also reduced to the pole. According to the residual magnetic anomalies (Figure 3.4, covered the same area as Figure 3.2), magnetic response over the Gallen deposit is relatively small (300 nT to 700 nT). But in the southwest of the area the maximum magnetic response reaches 2800 nT. We cut 10 W-E oriented profiles (W-E lines 1 to 10 from south to north), and 9 S-N oriented profiles (S-N lines 1 to 9 from west to east) from the magnetic residual anomalies map (Figure 3.4), in order to apply the depth imaging method for recovering a distribution of magnetic sources.

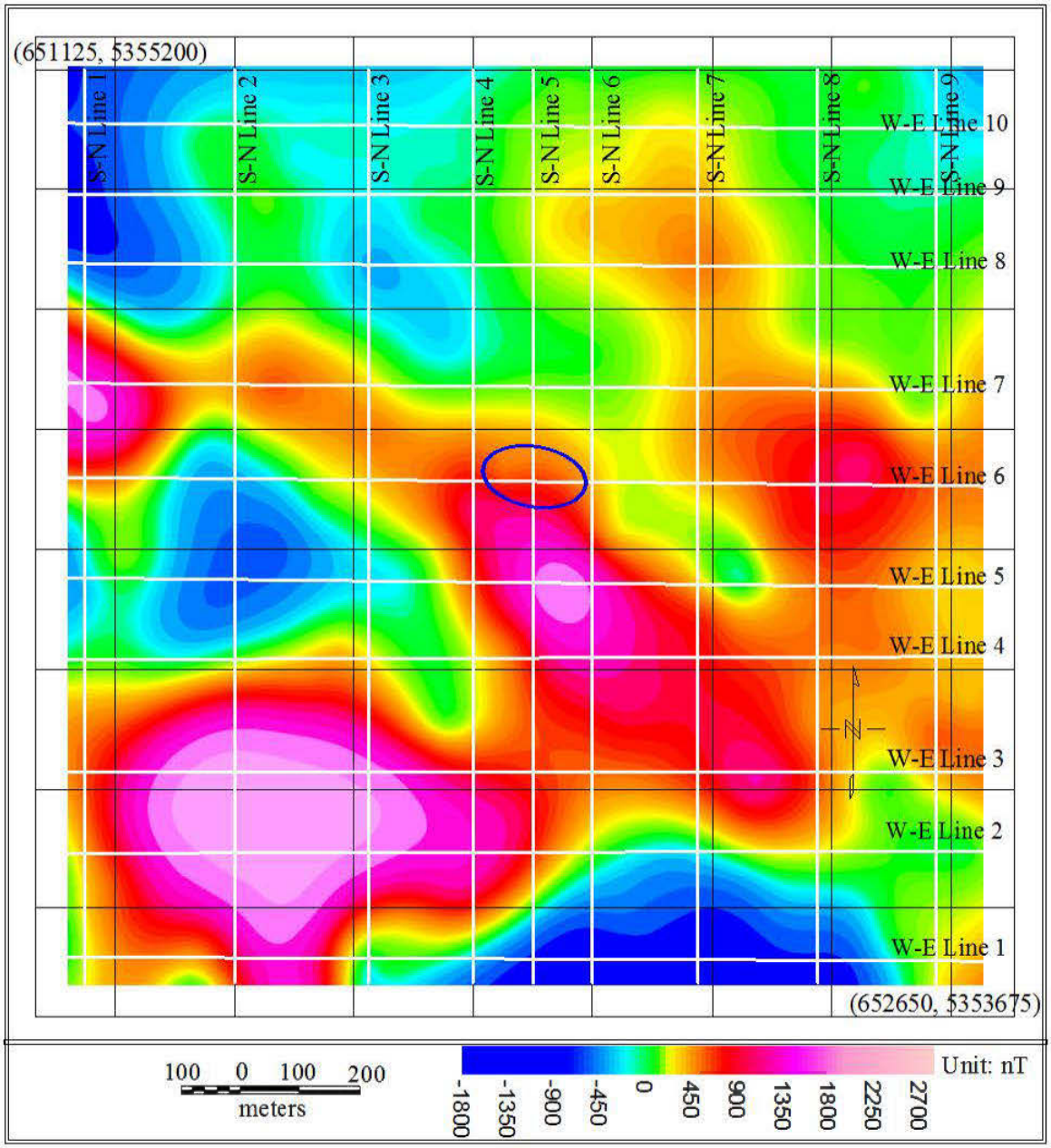

Figure 3.4: Residual magnetic anomalies over the Gallen deposit, the blue cycle indicates main Gallen ore body location, and white lines represent magnetic data interpretation profiles

3.3 Data processing results and interpretation

A 3D geological model was built up from the drillhole data for this area (Figure 3.5). On the left side, it is a top view of this 3D geological model which is simplified compared with Figure 3.2. A 3D view is on the right side of Figure 3.5.

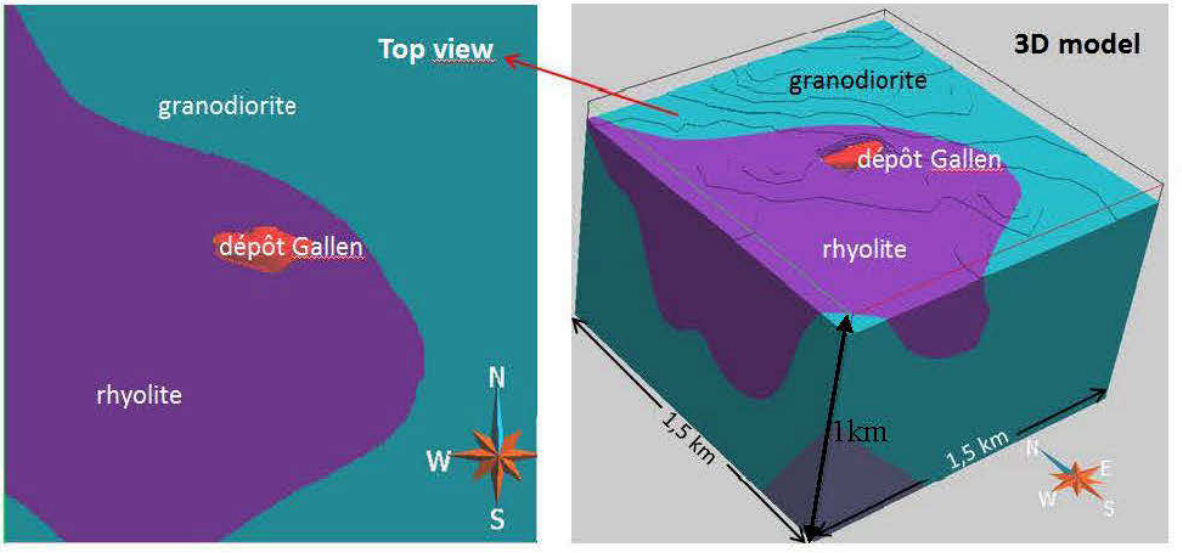

Figure 3.5: Top view of 3D model (left), the 3D geological model (right)

Using the depth imaging method, we processed the survey data along 19 profiles. In the processing, the width of window function is 256 sampling points and the type of window function is rectangular. We interpolate depth imaging results of 19 profiles and build up a power spectrum distribution in three dimensions (Figures 3.6 to 3.8). First, we looked at near surface geological features by comparing the depth imaging result and the detail geological map (Figure 3.6).

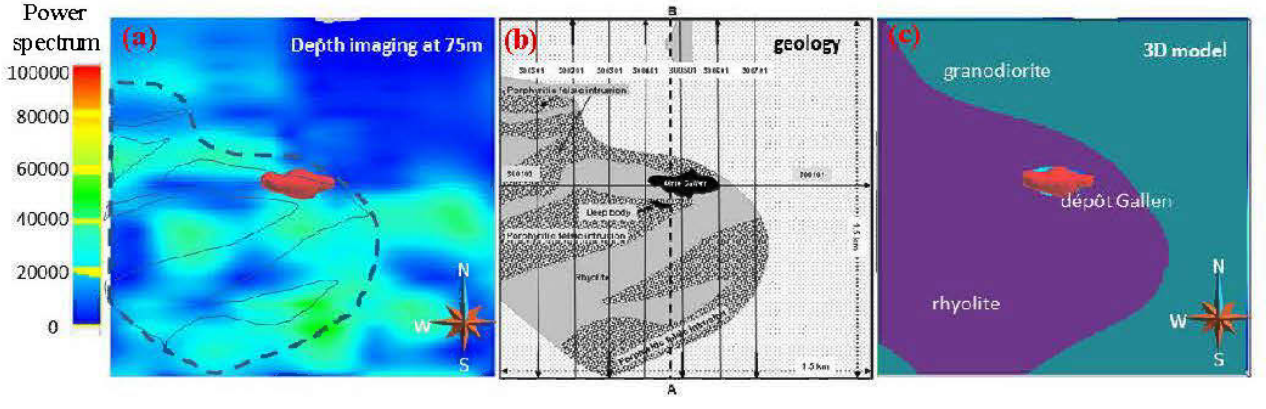

Figure 3.6: Comparisons between the depth imaging at the depth of 75m (left), detail geological map (middle) and 3D geological model (right)

Table 3 and Table 4 show magnetic susceptibilities and Koenigsberger ratios (Q) for some rocks and minerals respectively. The rhyolite has lower susceptibility compared with the porphyry and the granodiorite. It seems that the low Power spectrum zone corresponds to low

susceptibility lithology as rhyolite (compare the depth imaging result (left) with the detail geology (middle) on Figure 3.6).

Table 3.1: Magnetic susceptibilities of rocks and minerals (Christopher, et al. 1995)

Rock /Material	**Volume Susceptibility (SI)**
Granite	(0-50) x 10^{-3}
Gabbro	(1-90) x 10^{-3}
Diorite	(0.63-130) x 10^{-3}
Pyrite (FeS2)	(0.05-5) x 10^{-3}
Quartz	(-13-17) x 10^{-6}
Quartzite	4.4 x 10^{-3} (maximum)
Granodiorite	0.062 (maximum)
Andesite	170x 10^{-3} (maximum)
Dacite	0.05 (maximum)
Granite	(0-50) x 10^{-3}
Gabbro	(1-90) x 10^{-3}
Diorite	(0.63-130) x 10^{-3}

Table 3.2: Koenigsberger ratios (Q) for some rocks (Christopher, et al. 1995)

Rocks	**Koenigsberger ratio, Q_n**
Granite	0.1-28
Granodiorite	0.1-0.2
Gabbro	1-9.5
Intrusions	0.1-20
Volcanics	30-50
Magnetite ore	1-90

Note: Koenigsberger ratio (Q ratio) is defined as the ratio in a rock of remanent magnetization to the induced magnetization in the Earth's field.

We compared the 3D models from Depth Imaging to known geological 3D model (Figures 3.7 to 3.9). Both 3D models have size of 1.5 km square on the surface and down to 1 km of the

depth. The locations of five cross-sections cut from both 3D models are shown on the left of Figure 3.7 (top view). Since two 3D models are overlapped each other, we made the Depth Imaging to be demi-transparent, and use a white dash line to indicate the geological contact between the rhyolite and the granodiorite. The cross-sections EW-1 and EW-2 show a similar structure feature between both two 3D models (right on Figure 3.7).

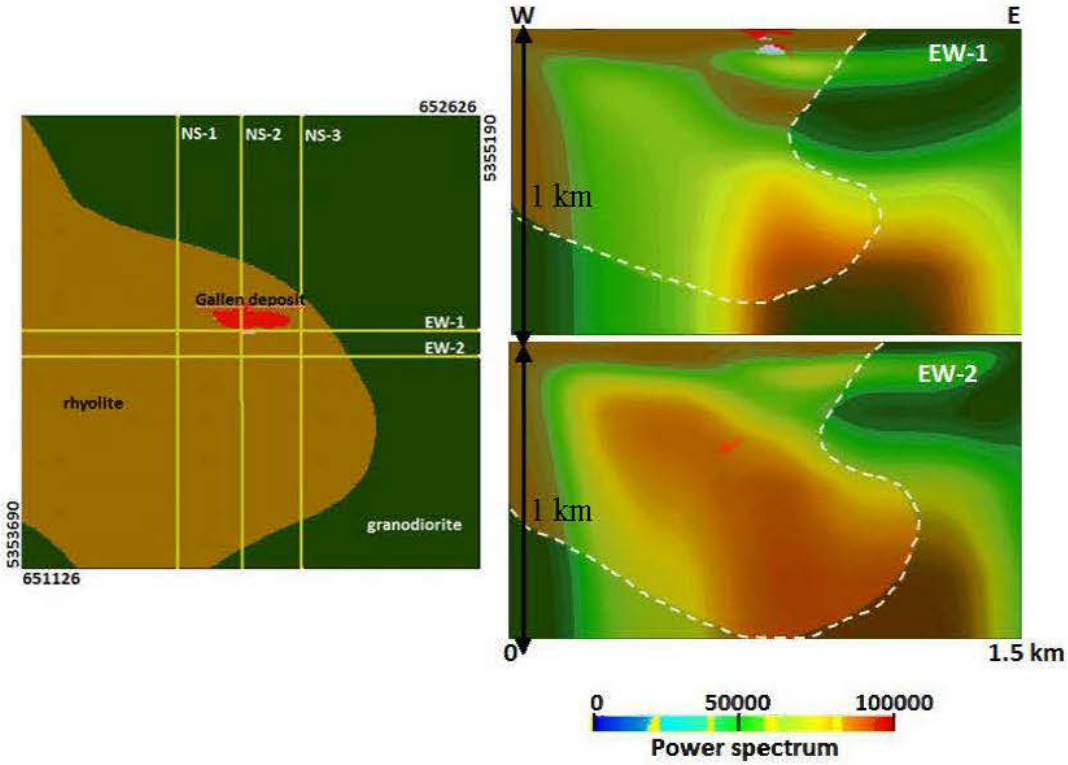

Figure 3.7: Two cross-sections from the Depth imaging 3D model (right) and their location over the 3D geological model (left)

The north contact between the rhyolite and the granodiorite is clearly shown by the discontinuity of Power spectrum from depth imaging (Figures 3.8 and 3.9). It is possible that the north contact is dipping to the south at the shallow level, but the existence of a deep source could be possible (Figure 3.8). This deep source has higher amplitude of Power spectrum (80000 to 100000), which might be the source of porphyry felsic intrusions.

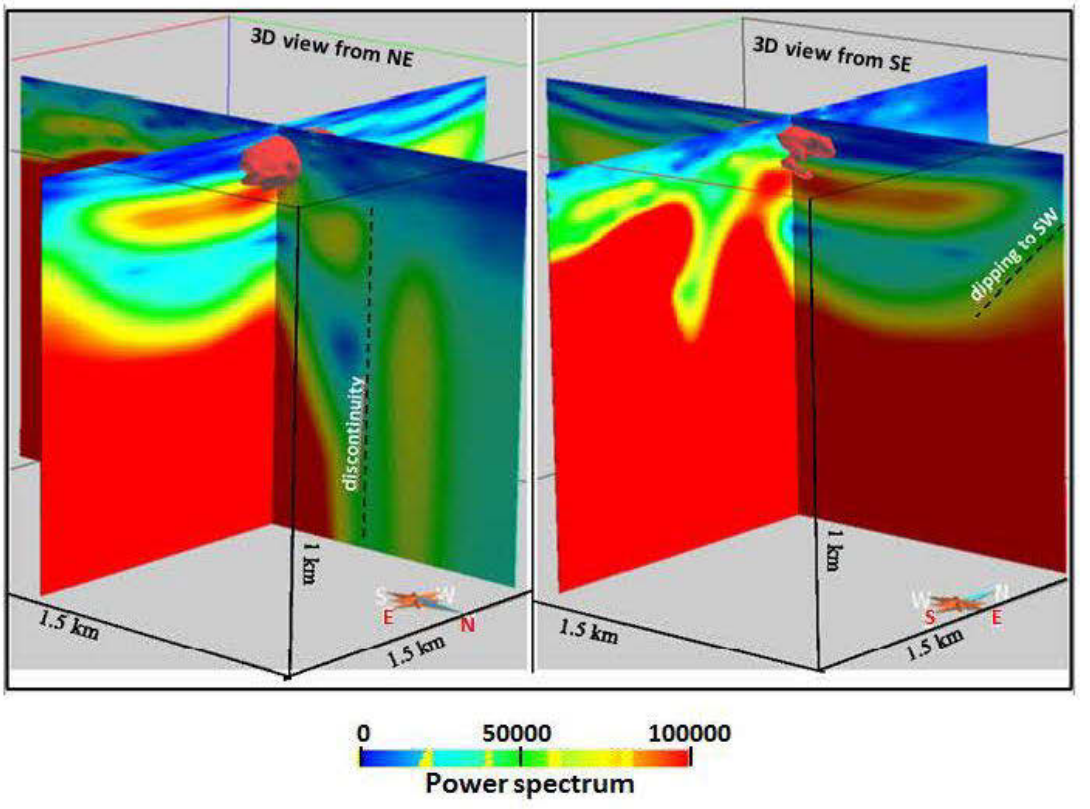

Figure 3.8: 3D view of the Depth imaging results from two cross-sections

The discontinuity of Power spectrum from the Depth Imaging, indicating the geological contact between the rhyolite and the granodiorite, is very clearly shown once again by three cross-sections on Figure 3.9 (red arrow). The locations of those three cross-sections are indicated on the right side of Figure 3.9 (top view). From those cross-sections we see that there are some zoning where the rhyolite is thicker. The white dash line indicates the geological contact between the rhyolite and the granodiorite from 3D geological model.

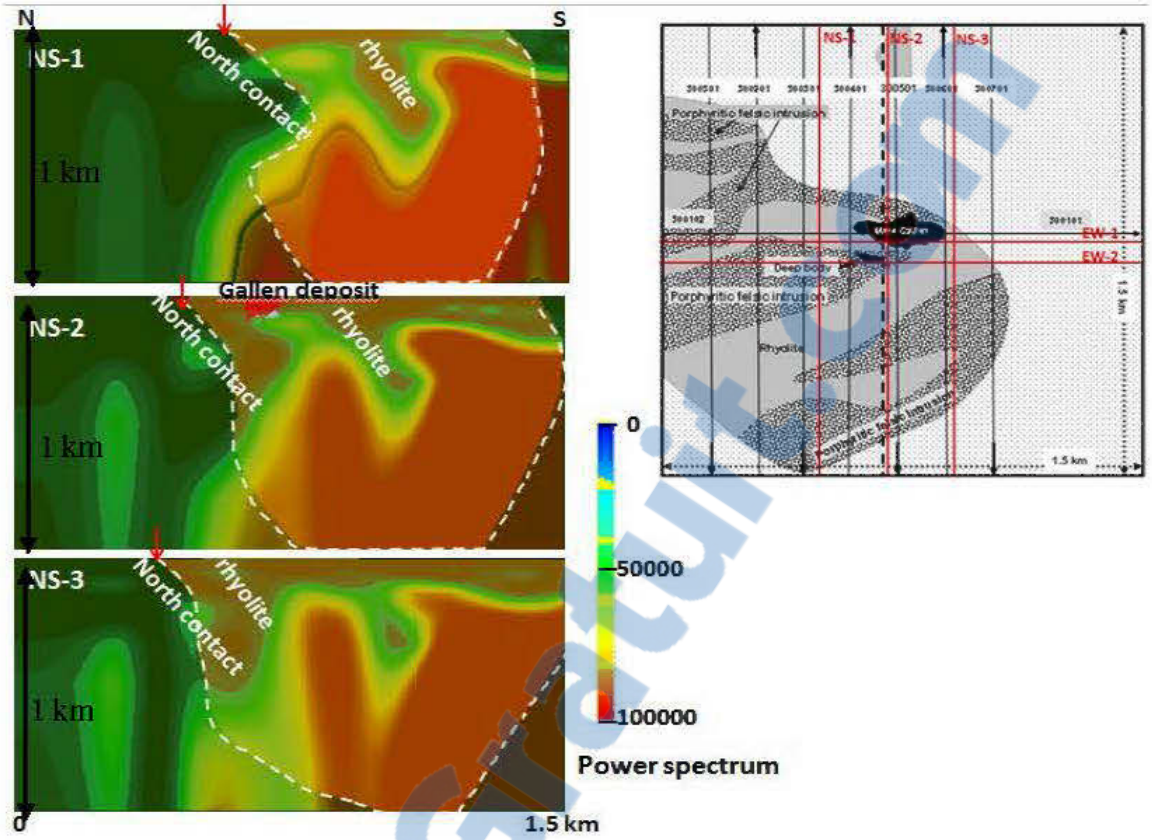

Figure 3.9: Three cross-sections from the Depth imaging 3D model (left) and their location on the detail geological map (right)

CONCLUSION

We studied the characteristics of the Power spectrum of magnetic field anomalies in the frequency domain and found that the spectrum of the anomaly is correlated with the depth of the source of the anomaly. We deduced a mathematical formula to express the relation between the depth and the wave number for a simple magnetic body. We extended this formula to a general situation and got a depth imaging method to interpret magnetic data in term of distribution of sources.

Using synthetic models, we tested this new method. For horizontal sources which are separated away in horizontal direction, we can estimate the depth of a body with a high spatial resolution. As the depth increases, higher accuracy is obtained regarding the depth estimation from the Power spectrum. For vertical superposed bodies, we can image the depth at the top of the deeper body. If a small body overlays a larger body, they can easily be separated by the discontinuity of their spectrum in the depth; however, when the bigger body overlays a small one, the top depth of the deepest body can be clearly determined only if they are separated by a certain distance.

For magnetic anomaly, the noise may cause a gross distortion to the result of Fourier transform as the *NSR* (the noise-signal ratio) increases, also the DC components become more significant. The impact of noise on the component with small wavenumber is smaller than that with bigger wavenumber for the peer noise-signal ratio.

For the problem of equivalent source, according to our studies it is possible that several magnetic bodies at the same depth can produce same magnetic anomalies. However, it only affects the form of the causative body without affecting the precise positioning of the source which is the most important factor in mineral exploration. For a vertical stack of several magnetic bodies, the depth impact on the shape of the magnetic anomaly cannot be compensated by the variation of reasonable susceptibility values. In addition, when the depth of abnormal body changes, the shape of magnetic anomaly also changes accordingly; therefore it is possible to distinguish the body to different depths by our new method.

The effect of the edge in the Fourier transform (the Gibbs phenomenon) was considered in our calculation. By using windows to smooth the signal, the results of Fourier transform are

much better than that of original signal. The principle to choose the window is that enough number of sampling points and adjusting the parameters of window function make the original signal smoother to zeros. Also the sampling points of window function do not be countless so that it affects the computing speed.

Through the case study of Gallen, we showed also that the depth imaging method can produce a complex model without any constraint of discretization of the model. We will continue to work in the future towards more complex geological situations by adding known information to improve spatial resolution. We also continue to find out the intrinsic link between the Power spectrum and physical properties such as the magnetic susceptibility.

REFERENCES

ALLDREDGE LR. (1981). Rectangular harmonic analysis applied to the geomagnetic field. *JGR*, 86, 3021-3026.

AMALENDU Roy. 1962. Ambiguity in geophysical interpretation. *Geophysics*, XXXVII (1), 90-99.

BACKUS G., GILBERT F. (1970). Uniqueness in the inversion of inaccurate gross earth data. Phil. Trans. R. *Soc.*, A266 (1173), 123-192.

BARNETT, C. T. (1976). Theoretical modeling of the magnetic and gravitational fields of an arbitrarily shaped three-dimensional body. *Geophysics*, 41, 1353-1364.

BARTON, D. C.. (1929). Calculations in the interpretation of observations with the Eotvos torsion balance. *AIME*, 481-486.

BERG E. (1990). Simple convergent genetic algorithm for inversion of multi parameter data. *60th SEG Annual Meeting*. 948-945.

BHATTACHARYYA B.K., CHAN K.C. (1977). Computation of gravity and magnetic anomalies due to inhomogeneous distribution of magnetization and density in a localized region. *Geophysics*, 42, 602-609.

BHATTACHARYYA, B. K. (1964). Magnetic anomalies due to prism-shaped bodies with arbitrary polarization. *Geophysics*, 29, 517-531.

BLUM, P. (1997). Physical properties handbook: a guide to the shipboard measurement of physical properties of deep-sea cores. *ODP Tech. Note, 26.*

BOSCH M., MEZA R., JIMENEZ R., HONING A. (2006). Joint gravity and magnetic inversion in 3D using Monte Carlo methods. *Geophysics*, 71(4), 153-156.

BOTT, M. H. P. (1959). The use of electronic digital computers for the evaluation of gravimetric terrain corrections. *Geophys. Prosp.*, 7, 45-54.

CHEN LONG-WEI, ZHANG HUI, AND ZHENG ZHI-QIANG. (2007). Technique of geomagnetic field continuation in underwater geomagnetic aided navigation. Journal of Chinese *Inertial Technology*, 15, 693-697.

CHEN J., KEMNA A., HUBBARD S.S. (2008). A comparison between Gauss-Newton and Markov-chain Monte Carlo-based methods for inverting spectral induced-polarization data for Cole-Cole parameters. *Geophysics*, 73(6), 247-259.

CHENG L. Z., RICHARD S., ALLARD M., CHOUTEAU M., KEATING P., LEMIEUX J., VALLÉE M.A., BOIS D., AND FOUNTAIN D., (2007). Geophysical case study of the Gallen deposit, Québec, Canada. *Exploration and Mining Geology*, 16, 67-81.

CHENG L. Z., RICHARD S., ALLARD M., KEATING P., CHOUTEAU M., LEMIEUX J., VALLÉE M.A., BOIS D., AND FOUNTAIN D., (2006a). Geophysical case study of the Iso and New Insco deposits, Québec, Canada: Part I, Data comparison and analysis. *Exploration and Mining Geology*, 15(1-2), 53-63.

CHENG L. Z., RICHARD S., ALLARD M., KEATING P., CHOUTEAU M., LEMIEUX J., VALLÉE M.A., BOIS D., AND FOUNTAIN D., (2005b). Geophysical case study of the Iso and New Insco deposits, Québec, Canada: Part II, Modeling and interpretation. *Exploration and Mining Geology*, 15(1-2), 65-74.

CHRISTOPHER P. HUNT, BRUCE M. MOSKOWITZ, SUBIR K. BANERJEE. (1995). Magnetic properties of rocks and minerals. *The American Geophysical Union*, 3, 189-204.

CHUI, CHARLES K. (1992). An Introduction to Wavelets. San Diego: Academic Press.

COOPER G. (2004). The stable downward continuation of potential field data. *Exploration Geophysics*, 35, 260-265.

CORDELL, L.E., GRAUCH, V., (1985). Mapping basement magnetization zones from aeromagnetic data in the San Juan Basin, New Mexico, in Hinze, W.J., The unility of regional gravity and magnetic anomaly maps. *Soc. Expl. Geophys.*, 181-197.

CURTIS A., SNIEDER R. (1997). Reconditioning inverse problems using the genetic algorithm and revised parameterization. *Geophysics*, 62(4), 1524-1532.

DAMPNEY, C. N. G., (1969). The equivalent source technique. *Geophysics*, 34, 39–53.

DAVE R.SCHMITZ. (1983). Geomagnetic spherical harmonic analysis 1. Techniques. Journal of geophysical research, 88, 1222-1228.

EMILIA, D. A., (1973). Equivalent sources used as an analytic base for processing total magnetic field data to a horizontal plane by means of finite harmonic series. *Geophysics*, 36, 856-866.

GIBBS J.W. (1899). Letter to the editor. *Nature*, 59,606.

GRANT F.S. (1973). The magnetic susceptibility mapping method for interpreting aeromagnetic surveys. *43rd Annual International Meeting*, SEG.

GUAN, ZHINING. (2005). Geomagnetic field and magnetic exploration. Book, *Geological Publishing House, Beijing.*

GUIMONT, B., RIOPEL, J. (1998). Undermine Gallen concession minings 345, 359, 398, canton of Dufresnoy: Report on work of diamond drilling carried out in Autumn 1998: *Mines et Exploration, Noranda Inc., internal report*, p.7.

HANSEN R.O., SIMMONDS M. (1993). Multiple-source Werner decomvolution. *Geophysics*, 58, 1792-1800.

HARTMAN R.R., TESKEY D.J., AND FRIEDBERG J.L. (1971). A system for rapid digital aeromagnetic interpretation. *Geophysics*, 36, 891-918.

HERNAN UGALDEL, WILLIAM A. (2010). Cluster analysis of Euler deconvolution solutions: New filtering techniques and geologic strike determination. *Geophysics*, 75(3), 61-70.

HJELT, S. E. (1972). Magnetostatic anomalies of a dipping prism. *Geoexplor*, 10, 239-254.

HUANG J., SIDERIS M.G., VANICEK P., et al.. A comparison of downward continuation techniques of terrestrial gravity anomalies. http://gge.unb.ca/Personnel/Vanicek/ Downward ContinuationTech.pdf.

JACOBSEN B.H. (1987). A case for upward continuation as a standard separation filter for potential-field maps. *Geophysics*, 52, 1138-1148.

JONT B. ALLEN. (1977). Short Time Spectral Analysis, Synthesis, and Modification by Discrete Fourier Transform. *IEEE Transactions on Acoustics, Speech, and Signal Processing*. ASSP-25 (3): 235–238.

KARA, İ., Bal, O. T., Tur, H., & Ates, A. (2014). A new efficient method for topographic distortion correction, analytical continuation, vertical derivatives and using equivalent source technique: Application to field data. *Journal of Applied Geophysics*, 106, 67-76.

KELBERT A., EGBERT G.D., SCHULTZ A. (2008). Non-linear conjugate gradient inversion for global EM induction: resolution studies. *Geophysical Journal international*, 73(2), 365-381.

KEVIN MCCLANING, TOM VITO, (2000). Radio receiver design. Noble Pub. Corp.

LI, Y., OLDENBURG D. W., (2010). Rapid construction of equivalent sources using wavelets. *Geophysics*, 75(3), L51-L59.

MARQUARDT D.W. (1963). An algorithm for least-squares estimation of nonlinear parameters. *Journal of Society for Industrial and Applied Mathematics*, 11(2), 431-441.

MICHELSON A.A. (1898). Letter to the editor. *Nature,* 58, 44-45.

MIOARA MANDEA, MONIKA KORTE. (2011). Geomagnetic observations and models. *Springer Dordrecht Herdelberg*, London New York.

MISENER D.J., GRANT F.S., WALKER P. (1984). Variable depth, space-domain magnetic susceptibility mapping. *SEG Expanded Abstracts*, 3,237.

OKABE. M. (1979). Analytical expressions for gravity anomalies due to homogeneous polyhedral bodies and translations into magnetic anomalies. *Geophysics*, 44(4), 730-741.

MOON W.M., USHAH A. (1988). Application of 2-D Hilbert transform in geophysical imaging with potential field data. *IEEE Transactions on Geosciences and Remote Sensing*, 26(5).

MUSHAYANDEBVU M.F., REID A.B. AND FAIRHEAD J.D. (2000). Grid Euler deconvolution with constraints for 2-D structures. *SEG expanded Abstracts*, 19, 398-401.

MUSHAYANDEBVU M.F., VAN DRIEL P., REID A.B., AND FAIRHEAD J.D. (2001). Magnetic source parameters of two-dimensional structures using extended Euler deconvolution. *Geophysics*, 66, 814-823.

MUSHAYANDEBVU M.F., LESUR V., REID A.B. AND FAIRHEAD J.D. (2004). Grid Euler deconvolution with constraints for 2D structures. *Geophysics*, 69, 489-496.

MYOUNG AN, JAMES W. COOLEY, AND RICHARD TOLIMIERI. (1990). Factorization method for crystallographic Fourier transforms. *Advances in Applied Mathematics*, 11, 358-371.

NABIGHIAN M.N. (1984). Toward a three-dimensional automatic interpretation of potential field data via generalized Hilbert transforms-Fundamental relations. Geophysics, 49, 780-786.

NAGY, D. (1966). *The gravitational attraction of a right rectangular prism. Geophysics*, 31, 362-371.

NEEDHAM, P. E. (1970). The formation and evaluation of detailed geopotential models based on point masses (No. DGS-149). *OHIO STATE UNIV COLUMBUS DEPT OF GEODETIC SCIENCE.*

NORDEN E. HUANG, ZHAOHUA WU. (2008). A review on Hilbert-Huang transform: method and its applications to geophysical studies. Reviews of Geophysics, 46(2).

O'BRIEN D.P. (1972). Compudepth, a new method for depth-to-basement compution: Symposium. *42nd Annual International Meeting of the SEG.*

PARKER, R. L. (1973). The rapid calculation of potential anomalies. *Geophys.* J. Roy. Astr. Soc., 31, 447-455.

PAUL, M. K. (1974). The gravity effect of a homogeneous polyhedron for three-dimensional interpretation. Pure and Appl. *Geophys.*, 112, 553-561.

PETER G. LELIÈVRE, DOUGLAS W. OLDENBURG. (2006). Magnetic forward modelling and inversion for high susceptibility. *Geophysics*, 166, 76-90.

PETER G. LELIÈVRE, DOUGLAS W. OLDENBURG. (2006). 3D magnetic inversion for total magnetization in areas with complicated remanence. *SEG Expanded Abstracts* (University of British Columbia-Geophysical Inversion Facility), 25.

PEDERSEN L.B. (1991). Relations between potential fields and some equivalent sources. *Geophysics*, 56, 961-971.

PLOUFF, D. (1976). Gravity and magnetic fields of polygonal prisms and application to magnetic terrain corrections. *Geophysics*, 41, 727-741.

REID A.B., ALLSOP J.M., GRANSER H., et al. (1990). Magnetic interpretation in three dimensions using Euler deconvolution. *Geophysics*, 55, 80-91.

RICHARD J.BLAKELY. (1995). Potential theory in gravity and magnetic applications. *Cambridge University Press.*

RIOPEL, J. (2001). Surveys during 2000, Gallen property, Dufresony Township, Nornanda Mining camp (in French): *Noranda Inc. Exploration*, p.12.

ROTHMAN D.H. (1986). Automatic estimation of large residual statics correction. *Geophysics*, 51, 332-346.

SHAMSIPOUR P., MARCOTTE D., CHOUTEAU M. (2012). 3D stochastic joint inversion of gravity and magnetic data. J. *Applied Geophysics*, 79, 27-37.

SHAMSIPOUR P., MARCOTTE D., CHOUTEAU M., et al. (2011). Stochastic inversion of a gravity field on multiple scale parameters using surface and borehole data. *Geophysical prospecting*, 59(6), 998-1012.

SHAMSIPOUR P., CHOUTEAU M., MARCOTTE D. (2011). *3D stochastic inversion of magnetic data. J. of Applied Geophysics*, 73(4), 336-347.

SHIZHE XU, YUNJU LOU. (1986). A method of calculating magnetic anomaly of an arbitrary body. *Computing Techniques for Geophysical and Geochemical Exploration*, 8(4), 260-275.

SIGH B. (2001). New method for fast computation of gravity and magnetic anomalies from arbitrary polyhedra. *Geophysics*, 66(2), 521-526.

SILVA J.B.C., HOHMANN G.W. (1984). Airborne magnetic susceptibility mapping. *Exploration Geophysics*, 15, 1-13.

SMITH M.L., SCALES J.A., FISCHER TL. (1992). Global search and genetic algorithm. *The Leading Edge of Exploration*, 11(1), 22-23.

STOCKWELL, RG. (1999). S-transform analysis of gravity wave activity from a small scale network of airglow imagers. *PhD thesis*, University of Western Ontario, London, Ontario, Canada.

STOCKWELL, R. G., MANSINHA, L., & LOWE, R. P. (1996). Localization of the complex spectrum: the S transform. *Signal Processing, IEEE Transactions* on, 44(4), 998-1001.

TALWANI, M. (1965). Computation with the help of a digital computer of magnetic anomalies caused by bodies of arbitrary shape. *Geophysics*, 30, 797-819.

TARANTOLA A. (1987). Inverse problem theory, methods of data fitting and mode parameter estimation. *Elsevier Publishing Co.*

THOMPSON D.T. (1982). EULDPH- a new technique for making computer-assisted depth estimates from magnetic data. *Geophysics*, 47, 31-37.

THURSTON J.B., SMITH R.S. (1997). Automatic conversion of magnetic data to depth dip, and susceptibility contrast using the SPITM method. *Geophysics*, 62, 807-813.

THURSTON J.B., SMITH R.S., GUILLON J.C. (2002). A multimodel method for depth estimation from magnetic data. *Geophysics*, 67, 555-561.

TROMPAT H., BOSCHETTI F., AND HORNBY P. (2003). Improved downward continuation of potential field data. *Exploration Geophysics*, 34, 249-256.

TRUDEAU, Y. (1984). Les Mines Gallen Massive sulfide deposit: *Noranda Exploration Co. Ltd., Additional Guide*, p.63.

UQAT, Noranda Exploration Inc., Fugro Airborne Surveys. (2004). Logistics and processing report: *Airborne magnetic and MEGATEM text over the Iso-New, Gallen and Aldermac deposit.*

WANG X., HANSEN R.O. (1990). Inversion for magnetic anomalies of arbitrary three-dimensional bodies. *Geophysics*, 55, 1321-1326.

WENXIAO ZHU, WANSHENG TU, TIAN YOU LIU. (1989). *Gravity and magnetic processing and interpretation in programming.* China University of Geosciences Press.

YAO, CHANGLI. (2009). *Applied geophysics* (magnetic exploration). Book, China University of Geosciences, Beijing.

YU-SHEN H., CHEINWAY HWANG. (2010). Topography-Assisted downward continuation of airborne gravity: an application for geoid determination in Taiwan. *Terr. Atmos. Ocean. Sci.*, 21, 629-637.

ZENG HUA LIN, (1985). Gravity and magnetic data processing program analysis. *Geological Publishing House.*

ZHALKOVESKY YE.A. (2008). Chart-making of the Earth's main magnetic field. *Russian Journal of Earth Sciences*, 10, ES4003, doi: 10.2205/2007ES000258.

ZHINING GUAN, JUNSHENG HOU, LINPING HUANG et al. (1998). Inversion of gravity and magnetic anomalies using pseudo-BP neural network method and its application. *Geophysics*, 41(2), 245-251.

ZIQIANG ZHU, GUOXIANG HUANG, (1994). Gravity and magnetic inversion by using artificial neural networks and its application in southern HuNan. *Journal of Central South University*, 25(3), 289-293.